THE ELECTRIC CONDUCTIVITY OF HOT PION MATTER

A Thesis

by

JOSEPH I. ATCHISON

Submitted to the Graduate and Professional School of Texas
A&M University
in partial fulfillment of the requirements for the degree of

PH. D. IN PHYSICS

Chair of Committee,	Ralf Rapp
Committee Members,	Rainer Fries
	Saskia Mioduszewski
	Sherry Yennello
Head of Department,	Grigory Rogachev

December 2021

Major Subject: Physics and Astronomy

ABSTRACT

The determination of transport coefficients plays a central role in characterizing hot and dense nuclear matter. Currently, there are significant discrepancies between various calculations of the electric conductivity of hot hadronic matter. It has been shown that dilepton emission spectra can be described by calculating the electromagnetic correlator within the vector dominance model (VDM). Transport coefficients probe the low-energy limit of the medium, thus the interactions of the low mass pion are expected to play an important role in determining the conductivity of hot hadronic matter. In the present work we calculate the electric conductivity of hot pion matter by extracting it from the electromagnetic spectral function, as its zero energy limit at vanishing 3-momentum. Within the VDM the photon couples primarily to the rho meson. Therefore, we use hadronic many-body theory to calculate the rho meson's self-energy in hot pion matter. This requires the dressing of the pion propagators within the rho self-energy with thermal π-ρ and π-σ loops, and the inclusion of vertex corrections to maintain gauge invariance. Furthermore, in order to obtain a finite conductivity, all intermediate particles must be dressed with self-energies. In particular, we analyze the transport peak of the spectral function and extract its behavior with temperature. Finally, we compare our results to previous calculations, including various calculations of the electric conductivity of hot pion matter, to a proposed quantum lower bound, and a proposed sum rule for the EM-spectral function.

ACKNOWLEDGMENTS

I would like to thank all of the faculty and staff and Texas A&M and at the Cyclotron Institute. With a special thanks to the computer support groups, who were of great assistance in maintaining the computing clusters.

I would also like to thank all of the members of the Ralf Rapp research group who provided advice and support including: Paul Hohler, Nathan Holt, Shuai Liu, Xiaojian Du, Isaac Sarver, Thomas Onyango, Biaogang Wu, and Zhanduo Tang.

CONTRIBUTORS AND FUNDING SOURCES

Contributors

This work was supported by a thesis committee consisting of Professors Ralf Rapp [advisor], Rainer Fries, and Saskia Mioduszewski, of the Department of Physics and Astronomy and Professor Sherry Yennello of the Department of Chemistry.

Funding Sources

This work is supported by the US-NSF under grants no.: PHY-1306359, PHY-1614484, and PHY-1913286.

TABLE OF CONTENTS

Page

1. INTRODUCTION AND LITERATURE REVIEW

In this section we provide an introduction to hot and dense nuclear matter, and the intriguing physical phenomena that arise under these conditions. To begin, in section 1.1, we discuss the theoretical motivation to study hot and dense nuclear matter and address how it can be produced and studied in heavy ion collisions (HICs). In section 1.2, we discuss how transport coefficients can be used to analyze HICs and nuclear matter, with particular focus on the electric conductivity. Finally, in section 1.3 we introduce the vector dominance model (VDM), emphasizing its successful description of dilepton emission spectra, and how the electric conductivity is related to the rho meson's spectral function in this framework.

1.1 Hot and dense nuclear matter

Hot and dense nuclear matter is a promising area of study, to shed light on fundamental phenomena such as: confinement, mass generation, and the nature of strongly coupled systems. The physics of nuclear matter is governed by the strong interaction, which is described by Quantum Chromodynamics (QCD) with the Lagrangian density [1, 2, 3]:

$$\mathcal{L}_{\text{QCD}} = \bar{q}(i\gamma^\mu D_\mu - \mathcal{M}_q)q - \frac{1}{4}G^a_{\mu\nu}G^{\mu\nu}_a, \tag{1.1}$$

$$D_\mu = \partial_\mu + ig_s\frac{\lambda_a}{2}A^a_\mu, \tag{1.2}$$

with quark and gluon fields q and A^a_μ, respectively, and Dirac, Gell-Mann and current-quark mass matrices γ^μ, λ^a and M_q, respectively. QCD has been quantitatively confirmed in high-energy scattering experiments, where the coupling is small and perturbation theory is reliable [4]. However, it is not obvious how QCD gives rise to many-body nuclear physics. Many phenomena are yet to be fully understood, such as quark confinement, mass generation, and the structure of the QCD phase diagram [58].

At small distances, the potential energy between two static quarks can be described with a Coulomb like potential, however, for large distances, the potential grows linearly with distance. The strong force is transmitted by gluons, which in the long distance limit can be visualized as a "string" connecting the quarks. In nature we do not observe isolated quarks, because as one separates two quarks it eventually becomes more energetically favorable for the "string" to "break", and form additional quarks. These additional quarks will couple to the original two quarks, producing separated hadrons, rather than two isolated quarks [7]. However, it is possible for quarks and gluons to become the relevant degrees of freedom in a system, because at high temperatures (T) and baryon chemical potentials (μ_B) the quark wave functions inside of hadrons begin to overlap. This overlap eventually allows quarks and gluons to move freely throughout the system [7]. This state is known as Quark-Gluon Plasma (QGP), and its study is a central objective of heavy-ion collision experiments at the Relativistic Heavy-Ion Collider (RHIC) and the Large Hadron Collider (LHC) [8, 9, 10, 11, 12].

The masses of quarks and other elementary particles are generated by a condensate of Higgs bosons, which breaks electroweak symmetry [13]. However, the resulting mass of the light up and down quarks is only about 3-5 MeV, while the mass of a nucleon is approximately 938 MeV. Thus, the masses of the up and down quarks only account for about 2% of the nucleon mass. The remaining mass is generated dynamically by the strong force [6]. The strong interaction also generates an quark anti-quark condensate that breaks the approximate chiral symmetry (conservation of left and right handedness) of QCD. This spontaneous symmetry breaking results in a mass splitting between chiral partners such as the ρ meson and the a_1 of about 500 MeV [6]. Furthermore, spontaneous symmetry breaking implies the generation of a "massless" Goldstone boson, in this case, the almost massless pion. The pion is in fact not massless, because chiral symmetry is also explicitly broken by the light quark mass [6]. The relation between the broken symmetries and the pion's mass can be expressed through the Gell-Mann-Oaks-Renner relation [14]:

$$m_\pi^2 f_\pi^2 = -2m_q\langle\bar{q}q\rangle. \tag{1.3}$$

From this relation, we see that $m_\pi^2 \propto m_q$, which demonstrates that should m_q be driven to zero the pion would become massless. Furthermore, since the pion mass is proportional to the root of the quark mass and not the quark mass, the pion mass is significantly heavier (140 MeV) than the light quark mass [14]. At high temperature and chemical potential, such as those obtained in HICs, it is believed the quark anti-quark condensate will evaporate, resulting in the restoration of chiral symmetry and a "melting" of hadronic masses [6].

Another goal of HICs is to probe the QCD phase structure. We have already mentioned that at high temperature and density one expects the formation of a QGP. At lower temperature and chemical potential matter will hadronize, forming hot hadronic matter. This state is also of interest as chiral restoration commences in this phase, furthermore hot hadronic matter may represent a strongly coupled system where particle widths become of the same order as their energy [6]. Finally, at high density and low temperature it is believed that quark Cooper pairs will condense, resulting in a Color Super Conductor (CSC) [15]. Mapping out the QCD phase diagram will require an understanding of the nature of the various QCD phase transitions, their locations, and the search for possible critical points in the chiral phase transition.

1.2 Transport coefficients

One achievement of the field has been the description of HICs with relativistic hydrodynamics [16]. Hydrodynamic models utilize transport coefficients such as viscosity as inputs, which helps characterize the medium. Transport coefficients probe the long wavelength limit of the medium, and describe how conserved quantities propagate through the medium. For instance, viscosity describes the flow of 4-momentum, the heavy-quark transport coefficient describes the diffusion of heavy quarks, and electric conductivity describes the transport of charge. The viscosity over entropy density has been extracted from measurements of the elliptic flow in off-central collisions

[16]. Heavy-quark transport coefficients have also been inferred, from measurements of elliptic flow and transverse momentum spectra of heavy-flavor particles [17, 18]. One believes that these quantities should be closely related, as they all quantify transport through the same medium.

This work will focus on the calculation of the electric conductivity, closely related to soft dilepton emission [19]. One can investigate the medium produced in HICs by studying charge correlations, which quantify how pairs of conserved charge, created during the collision, propagate through the medium [20]. The electric conductivity is related to charge diffusion, and should impact the evolution of charge correlations in HICs. Recent calculations of the electric conductivity in hot hadronic matter have been performed, however, their results have varied considerably [21, 22, 23, 24, 25, 26, 27, 28, 29, 30, 31]. These calculations utilized various formalisms including: kinetic theory, chiral perturbation theory, K-matrix, hadronic many-body theory, perturbative approaches to the QGP, approximate solutions to the relativistic transport equation, lattice QCD, and conformal field theory. A quantum lower bound was also proposed in [22].

Here, we seek to perform a hadronic quantum many-body calculation, which approximately maintains gauge invariance. Our calculation is rooted in dilepton emission calculations reviewed in references [6, 32], which describe observed dilepton spectra in HICs. The dilepton emission rate is proportional to the electromagnetic spectral function ($\mathrm{Im}\Pi^{\mathrm{EM}}_{\mu\nu}$) [33, 34],

$$\frac{dR_{l+l-}}{d^4q} = \frac{-\alpha^2_{\mathrm{EM}}}{3\pi^3 M^2} f_B(q_0, T) g_{\mu\nu} \mathrm{Im}[\Pi^{\mu\nu}_{\mathrm{EM}}(M, q, T, \mu_B)], \tag{1.4}$$

where f_B denotes the Bose distribution, $M^2 = q_0^2 - \vec{q}^{\,2}$ is the dilepton's invariant mass and α_{EM} the fine-structure constant, $\alpha_{\mathrm{EM}} = \frac{e^2}{4\pi}$. In particular the electric conductivity can be obtained from $\Pi^{\mathrm{EM}}_{\mu\nu}$ in the zero-momentum, low-energy limit [35]:

$$\sigma_{el}(T) = \frac{-e^2}{3} \lim_{q_0 \to 0} \frac{\mathrm{Im}[\Pi^{ii}_{\mathrm{EM}}(q_0, \vec{q} = 0, T)]}{q_0}, \tag{1.5}$$

demonstrating the connection to dilepton emission calculations.

Reference [35] evaluated transport coefficients in weakly-coupled high-temperature gauge the-

ories and found that, at zero momentum, the electromagnetic spectral function displays a Lorentzian-like transport peak centered at zero energy. For vanishing coupling the transport peak becomes a Dirac δ-function, resulting in an infinite conductivity. As the coupling is increased the peak broadens, implying a finite conductivity. In figure 1.1 we demonstrate how a medium particle can interact with a photon through an intermediate pion. The bubble on the pion represents the pion's interaction with the medium. These interactions generate a finite width for the resonant particle. As previously stated, if this width is ignored an infinite conductivity results, as is expected from a non-interacting gas. Furthermore, because the conductivity is extracted from the low energy limit, one requires an interaction that is not subject to a low energy threshold, such as vacuum decays. Therefore, at least two thermal particles are necessary to obtain a finite conductivity, one incoming particle to create a resonance and a second to generate the resonance's low energy width.

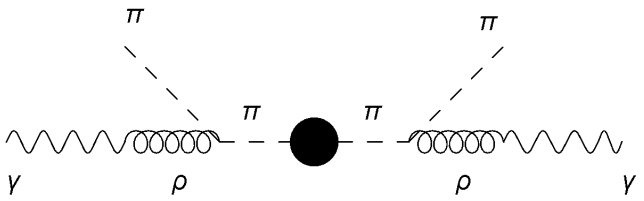

Figure 1.1: Photon coupling with the medium through a rho meson. The rho meson interacts with the medium through an intermediate pion. The bubble represents the width the pion obtains due to interaction with the medium.

1.3 Vector dominance model

The electromagnetic correlation function is defined through [36]:

$$\Pi^{\mu\nu}_{\rm EM}(q_0,\vec{q}) = -i\int d^4x e^{iq\cdot x}\Theta(x_0)\langle\langle[j^\mu_{\rm em}(x), j^\nu_{\rm em}(0)]\rangle\rangle, \tag{1.6}$$

where $j^\mu_{\rm em}$ is the hadronic EM current. For invariant mass below approximately 1 GeV, the EM spectral function is well described within the vector dominance model (VDM) [36]. In the VDM it is assumed that electromagnetic interactions in hadronic matter are mediated by the neutral vector

mesons (ρ, ω, and ϕ), the EM current is then given by the field current identity [36]:

$$j^{\mu}_{\text{em}}(M \leq 1\,\text{GeV}) = \frac{m_{\rho}^2}{g_{\rho}}\rho^{\mu} + \frac{m_{\omega}^2}{g_{\omega}}\omega^{\mu} + \frac{m_{\phi}^2}{g_{\phi}}\phi^{\mu}, \tag{1.7}$$

and the EM correlation function by:

$$\Pi^{\mu\nu}_{\text{EM}} \approx \frac{(m_{\rho}^0)^4}{g_{\rho}^2}D^{\mu\nu}_{\rho} + \frac{(m_{\omega}^0)^4}{g_{\omega}^2}D^{\mu\nu}_{\omega} + \frac{(m_{\phi}^0)^4}{g_{\phi}^2}D^{\mu\nu}_{\phi}. \tag{1.8}$$

The dominant contribution to $\Pi^{\text{EM}}_{\mu\nu}$ comes from the rho meson. This can be seen by writing j^{μ}_{em} in the quark basis [6]:

$$j^{\mu}_{\text{em}} = \frac{1}{\sqrt{2}}\bar{\psi}\gamma^{\mu}\psi\left[\frac{\bar{u}u - \bar{d}d}{\sqrt{2}} + \frac{1}{3}\frac{\bar{u}u + \bar{d}d}{\sqrt{2}} - \frac{\sqrt{2}}{3}\bar{s}s\right]. \tag{1.9}$$

After inserting j^{μ}_{em} into eq. 1.6 ones sees that the ω meson is suppressed by a factor of $\frac{1}{9}$, and the ϕ meson by a factor of $\frac{2}{9}$. Additionally, the ϕ meson has a mass approximately 300 MeV higher than the ρ and ω mesons, and contains strange quarks. Thus, the electromagnetic spectral function can be approximated in terms of only the ρ meson. The electric conductivity is then given by:

$$\sigma_{\text{el}}(T) = \frac{-e^2(m_{\rho}^0)^4}{3g_{\rho}^2}\lim_{q_0 \to 0}\frac{\text{Im}[D^{ii}_{\rho}(q_0, \vec{q} = 0, T)]}{q_0}. \tag{1.10}$$

The rho propagator can be expressed in terms of the transverse and longitudinal projection operators $P_T^{\mu\nu}$ and $P_L^{\mu\nu}$ [37]:

$$D^{\mu\nu}_{\rho}(q,T) = \frac{P_T^{\mu\nu}}{M^2 - (m_{\rho}^0)^2 - \Sigma_{\rho}^T(q,T)} + \frac{P_L^{\mu\nu}}{M^2 - (m_{\rho}^0)^2 - \Sigma_{\rho}^L(q,T)} + \frac{q^{\mu}q^{\nu}}{(m_{\rho}^0)^2 M^2}, \tag{1.11}$$

where m_ρ^0 is the bare rho mass and $M^2 = q_0^2 - \vec{q}^{\,2}$ is the rho meson's invariant mass. The projection operators are defined by:

$$P_T^{\mu\nu} = \begin{cases} 0 & \mu = 0 \ \text{ or } \ \nu = 0 \\ \delta^{\mu\nu} - \frac{q^\mu q^\nu}{\vec{q}^2} & \mu, \nu \in \{1,2,3\} \end{cases}, \qquad P_L^{\mu\nu} = \frac{q^\mu q^\nu}{M^2} - g^{\mu\nu} - P_T^{\mu\nu}. \tag{1.12}$$

The rho self-energy, $\Sigma_\rho^{\mu\nu}$, characterizes the rho's interactions in the vacuum and with the medium. The transverse and longitudinal components of the rho self-energy, Σ_ρ^T and Σ_ρ^L, are defined through:

$$\Sigma_\rho^{\mu\nu}(q,T) = P_T^{\mu\nu}\Sigma_\rho^T(q,T) + P_L^{\mu\nu}\Sigma_\rho^L(q,T). \tag{1.13}$$

One can use eq. 1.12 and eq. 1.13 to show:

$$\Sigma_\rho^T(q,T) = \frac{1}{2}P_T^{\mu\nu}\Sigma_{\rho\,\mu\nu}(q,T), \qquad \Sigma_\rho^L(q,T) = P_L^{\mu\nu}\Sigma_{\rho\,\mu\nu}(q,T). \tag{1.14}$$

In order to calculate the conductivity, one requires D_ρ^{ii}. One can write D_ρ^{ii} in terms of Σ_ρ^T and Σ_ρ^L using eq. 1.11:

$$\begin{aligned} \text{Im}[D_\rho^{ii}(q,T)] &= \text{Im}\big[\frac{P_T^{ii}}{M^2 - (m_\rho^0)^2 - \Sigma_\rho^T(q,T)} + \frac{P_L^{ii}}{M^2 - (m_\rho^0)^2 - \Sigma_\rho^L(q,T)}\big] \\ &= \text{Im}\big[\frac{2}{M^2 - (m_\rho^0)^2 - \Sigma_\rho^T(q,T)} + \frac{q_0^2}{M^2}\frac{1}{M^2 - (m_\rho^0)^2 - \Sigma_\rho^L(q,T)}\big]. \end{aligned} \tag{1.15}$$

For $\vec{q} = 0$, $\Sigma_T(q,T) = \Sigma_L(q,T)$, therefore one can write:

$$\text{Im}[D_\rho^{ii}(\{q_0, \vec{q} = 0\}, T)] = \text{Im}\big[\frac{3}{M^2 - (m_\rho^0)^2 - \Sigma_T(\{q_0, \vec{q} = 0\}, T)}\big]. \tag{1.16}$$

The conductivity is then given by:

$$\sigma_{\text{el}}(T) = \frac{-e^2(m_\rho^0)^4}{g_\rho^2} \lim_{q_0 \to 0} \text{Im}\big[\frac{1}{q_0^2 - (m_\rho^0)^2 - \Sigma_\rho^T(\{q_0, \vec{q} = 0\}, T)}\big]. \tag{1.17}$$

In ref. [38] it was found that there are two rho self-energy diagrams required to maintain gauge invariance in vacuum, see fig. 1.2. The first is the $\pi\pi$-loop, which gives rise to the vacuum $\rho \to \pi\pi$ decay. The second is the tad pole loop, which involves a vacuum four-point interaction, and produces a constant shift in the rho mass.

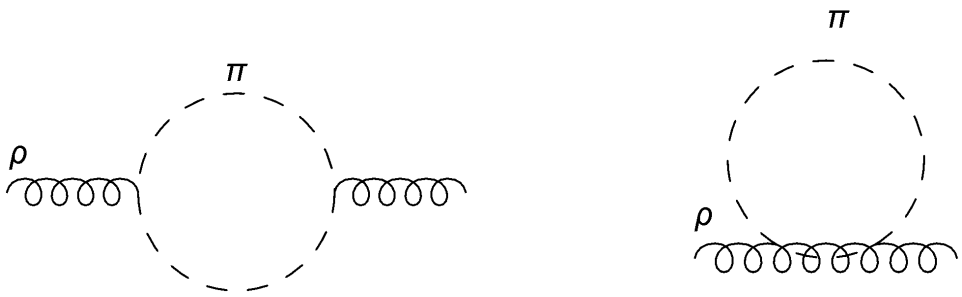

Figure 1.2: Left: The $\pi\pi$-loop of the rho self-energy. Right: The rho self-energy tadpole loop. These diagrams are the minimum diagrams necessary to maintain gauge invariance in vacuum.

If one extends the $\pi\pi$-loop to finite temperature, it encompasses $\rho\pi$-scattering into an intermediate pion state. As fig 1.1 suggests, such scatterings are crucial when calculating the conductivity. The pion's width is included by dressing the pion propagators in figure 1.2 with a pion self-energy (Σ_π):

$$D_\pi(k) = \frac{1}{k^2 - m_\pi^2 - \Sigma_\pi(k)}. \tag{1.18}$$

Similarly to $\Sigma_\rho^{\mu\nu}$, the pion self-energy characterizes the pion's medium interactions. These interactions provide the second thermal particle necessary to obtain a finite conductivity. One can then calculate $\Pi_{\rm EM}^{\mu\nu}$ within a fully quantum formalism, by integrating over the off-shell effects of the dressed propagators within the self-energies.

The contributions of thermal baryons to $\Sigma_\rho^{\mu\nu}$ were calculated in refs. [19, 37, 39, 40, 41, 42, 43]. Reference [40] considered $\gamma\pi$ scattering, however the pion's width was generated through interactions with nucleons. The effects of $\pi\pi$-scattering were not included. At small temperatures

and low baryon chemical potential baryon-antibaryon excitations are suppressed and the effects of the lighter pions dominate. Thus, we seek to add $\pi\pi$-scattering to the baryonic effects calculated in [40]. It was found in references [38, 43] that adding in-medium pion self-energies violates gauge invariance. In order to maintain gauge invariance, vertex corrections were constructed and calculated in references [38, 40, 41, 43, 44]. In this work, the electromagnetic spectral function and the electric conductivity will be calculated in hot pion matter both with and without vertex corrections.

This thesis is organized as follows: in chapter 2 we discuss the basic expressions for the rho meson self-energy in vacuum and at finite temperature, and discuss simplifying scenarios for the conductivity including sharp (on-shell) pions and constant pion widths. We calculate the pion self-energy in chapter 3, focusing on S- and P-wave scattering through sigma and rho resonances, respectively. The vertex corrections required to maintain gauge invariance are calculated in chapter 4. In chapter 5 we discuss the EM spectral function and the conductivity of hot pion matter with and without vertex corrections. Applications of the EM spectral function are discussed in chapter 6, specifically the calculation of the charge susceptibility and comparison to a sum rule from ref. [45]. Finally, we summarize and discuss future work in chapter 7.

2. RHO MESON SELF-ENERGY

In this chapter we discuss the rho meson's self-energy, and demonstrate how it can be used to calculate the electric conductivity. The vacuum self-energy is calculated in section 2.1. In section 2.2, we introduce the Ward-Takahashi identities and show that gauge invariance is satisfied in vacuum. The rho self-energy is extended to finite temperature in section 2.3, by introducing thermal $\rho\pi$-scattering and Bose enhancement of the vacuum $\rho \to \pi\pi$ decay. In section 2.4 we take the transverse projection of the rho self-enery. Next, we address the need to introduce a finite pion width into the rho self-energy. In section 2.5, the conductivity is approximated for a small constant pion width. Finally, in section 2.6 we calculate the conductivity for a constant width, without use of the small width approximation.

2.1 Vacuum self-energy

In ref. [38] it was found that there are two rho self-energy diagrams required to maintain gauge invariance in vacuum, see Fig. 1.2. The self-energies were derived from the Lagrangians:

$$\mathcal{L}_\pi + \mathcal{L}_\rho = \frac{1}{2}\partial_\mu\vec{\phi}\cdot\partial^\mu\vec{\phi} - \frac{1}{2}m_\pi^2\vec{\phi}\cdot\vec{\phi} - \frac{1}{4}\rho_{\mu\nu}\rho^{\mu\nu} + \frac{1}{2}(m_\rho^{(0)})^2\rho_\mu\rho^\mu \tag{2.1}$$

$$\mathcal{L}_{\pi\rho} = \frac{1}{2}ig_\rho\rho_\mu(T_3\vec{\phi}\cdot\partial^\mu\vec{\phi} + \partial^\mu\vec{\phi}\cdot T_3\vec{\phi}) - \frac{1}{2}g_\rho^2\rho_\mu\rho^\mu T_3\vec{\phi}\cdot T_3\vec{\phi}. \tag{2.2}$$

Here, $\rho_{\mu\nu} = \partial_\mu\rho_\nu - \partial_\nu\rho_\mu, T_3 = -i\epsilon_{3ab}$, and $m_\pi = 140\,\text{MeV}$ is the pion mass. One can derive the vacuum rho propagator (D_ρ), pion propagator (D_π), $\rho\pi\pi$ vertex $(\Gamma^{(3)}_{\mu(ab)})$ and $\rho\rho\pi\pi$ vertex $(\Gamma^{(4)}_{\mu\nu(ab)})$ from eqs. 2.1 and 2.2, given by:

$$D_\pi(k) = \frac{1}{k^2 - m_\pi^2 + i\epsilon} \tag{2.3}$$

$$D_\rho^{\mu\nu}(k) = \frac{-g^{\mu\nu} + \frac{k^\mu k^\nu}{k^2}}{k^2 - (m_\rho^0)^2 + i\epsilon} + \frac{k^\mu k^\nu}{(m_\rho^{(0)})^2 k^2} \tag{2.4}$$

$$\Gamma^{(3)}_{\mu\,abc} = g_\rho\epsilon_{cab}(2k+q)_\mu \tag{2.5}$$

$$\Gamma^{(4)}_{\mu\nu\,abcd} = ig_\rho^2(2\delta_{ab}\delta_{cd} - \delta_{ac}\delta_{bd} - \delta_{ad}\delta_{bc})g_{\mu\nu}, \tag{2.6}$$

where g_ρ is the $\rho\pi\pi$ coupling, Greek indices are used to denote Lorentz space, and Roman are used to denote isospin. The expression for the pion propagator in eq. 2.3 differs from that given in eq. 1.18, in that eq. 2.3 does not include the pion self-energy. Equation 2.3 defines the sharp pion propagator, which assumes pions to be noninteracting. In chapter 3 we will derive the pion self-energy and demonstrate how the sharp propagator can be dressed to obtain eq. 1.18. Figure 2.1 expresses the propagators and vertices diagramatically.

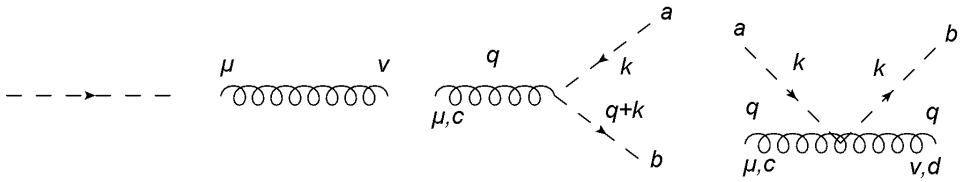

Figure 2.1: From left to right: π-propagator, ρ-propagator, $\pi\pi\rho$ vertex, and $\pi\pi\rho\rho$ vertex.

The rho self-energy is then given by:

$$\begin{aligned}\Sigma_\rho^{\mu\nu}(q) &= \frac{-i}{2}\int\frac{d^4k}{(2\pi)^4}D_\pi(k)D_\pi(q+k)\Gamma^{(3)}_{\mu\,3ab}(k,q)\Gamma^{(3)}_{\mu\,3ba}(q+k,-q)\\ &\quad -\frac{1}{2}\int\frac{d^4k}{(2\pi)^4}D_\pi(k)\Gamma^{(4)}_{\mu\nu\,aa33}(k,q),\end{aligned}\tag{2.7}$$

where repeated isospin indices are summed over. The first integral corresponds to the $\pi\pi$-loop in fig. 1.2, and the second integral to the tad pole loop. A symmetry factor of $\frac{1}{2}$ has been added to both terms to remove double counting of pion states. This is because the pion is distinguishable in particle space, but not in isospin space. In eq. 2.7 we have written $\Sigma_\rho^{\mu\nu}$ in terms of a general pion propagator and general $\rho\pi\pi$ and $\rho\rho\pi\pi$ vertices. If one inserts the vacuum propagator and vertices into eq. 2.7 one obtains:

$$\begin{aligned}\Sigma_\rho^{\mu\nu}(q) &= ig_\rho^2\int\frac{d^4k}{(2\pi)^4}\frac{(2k+q)^\mu(2k+q)^\nu}{(k^2-m_\pi^2+i\epsilon)((q+k)^2-m_\pi^2+i\epsilon)}\\ &\quad -2ig_\rho^2\int\frac{d^4k}{(2\pi)^4}\frac{g^{\mu\nu}}{k^2-m_\pi^2+i\epsilon}.\end{aligned}\tag{2.8}$$

One must take care to not violate gauge invariance when regularizing $\Sigma_\rho^{\mu\nu}$. In references [46, 38] the Pauli-Villars regularization scheme was used. In this scheme, rho self-energies are calculated using heavy pion propagators, that is one replaces m_π with a higher mass, but keeps the quantum numbers of the pion. The heavy pion terms are then subtracted from the vacuum rho self-energy. The regularized self-energy is given by:

$$\Sigma_\rho'^{\mu\nu}(q) = \Sigma_\rho^{\mu\nu}(q, m_\pi) - 2\Sigma_\rho^{\mu\nu}(q, \sqrt{m_\pi^2 + \Lambda_0^2}) + \Sigma_\rho^{\mu\nu}(q, \sqrt{m_\pi^2 + 2\Lambda_0^2}). \tag{2.9}$$

We adopt the values $g_\rho = 5.9$, $m_\rho^{(0)} = 853\,\mathrm{MeV}$, and $\Lambda_0 = 1\,\mathrm{GeV}$, which were obtained by fitting the P-wave $\pi\pi$-scattering phase shift and the pion electromagnetic form factor in ref. [46]. It was demonstrated in ref. [38], that the vacuum rho self-energy can be resummed into the rho propagator:

$$\begin{aligned} D_\rho^{\mu\nu}(k) &= D_\rho(k)(-g^{\mu\nu} + \frac{k^\mu k^\nu}{k^2}) + \frac{k^\mu k^\nu}{(m_\rho^{(0)})^2 k^2}, & (2.10)\\ D_\rho(k) &= \frac{1}{k^2 - (m_\rho^0)^2 - \Sigma_\rho(k)}, & (2.11)\\ \Sigma_\rho^{\mu\nu}(k) &= (-g^{\mu\nu} + \frac{k^\mu k^\nu}{k^2})\Sigma_\rho(k). & (2.12) \end{aligned}$$

2.2 Gauge invariance in vacuum

In the VDM the rho couples to a conserved current, and thus must be four-dimensionally transverse ($q^\mu \Sigma_{\rho\,\mu\nu} = 0$) [40]. Transversality is ensured if the $\rho\pi\pi$ and $\rho\rho\pi\pi$ vertices satisfy the Ward-Takahashi identities:

$$\begin{aligned} q^\mu \Gamma^{(3)}_{\mu\,ab3} &= g_\rho \epsilon_{3ab}(D_\pi^{-1}(k+q) - D_\pi^{-1}(k)) & (2.13)\\ q^\mu \Gamma^{(4)}_{\mu\nu\,ab33} &= i g_\rho(\epsilon_{3ca}\Gamma^{(3)}_{\nu\,bc3}(k, -q) - \epsilon_{3bc}\Gamma^{(3)}_{\nu\,ca3}(k+q, -q)). & (2.14) \end{aligned}$$

It is straight forward to demonstrate that $\Sigma^{\mu\nu}_{\rho}$ will be four-dimensionally transverse if the Ward-Takahashi identities are satisfied:

$$\begin{aligned}
q^{\mu}\Sigma_{\rho\,\mu\nu}(q,T) =& \frac{-i}{2}\int\frac{d^4k}{(2\pi)^4}q_{\mu}\Gamma^{(3)}_{\mu\,ab3}(k,q)\Gamma^{(3)}_{\nu\,ba3}(q+k,-q)D_{\pi}(k)D_{\pi}(q+k)\\
&-\frac{1}{2}q_{\mu}\int\frac{d^4k}{(2\pi)^4}\Gamma^{(4)}_{\mu\nu\,aa33}(k,q)D_{\pi}(k)\\
=&\frac{-i}{2}\int\frac{d^4k}{(2\pi)^4}g_{\rho}\epsilon_{3ab}(D_{\pi}^{-1}(k+q)-D_{\pi}^{-1}(k))\Gamma^{(3)}_{\nu\,ba3}(q+k,-q)D_{\pi}(k)D_{\pi}(q+k)\\
&-\frac{1}{2}\int\frac{d^4k}{(2\pi)^4}ig_{\rho}(\epsilon_{3ba}\Gamma^{(3)}_{\nu\,ab3}(k,-q)-\epsilon_{3ab}\Gamma^{(3)}_{\nu\,ba3}(k+q,-q))D_{\pi}(k)\\
=&\frac{-i}{2}g_{\rho}\int\frac{d^4k}{(2\pi)^4}\epsilon_{3ab}\Gamma^{(3)}_{\nu\,ba3}(q+k,-q)D_{\pi}(k)\\
&-\frac{-i}{2}g_{\rho}\int\frac{d^4k}{(2\pi)^4}\epsilon_{3ab}\Gamma^{(3)}_{\nu\,ba3}(q+k,-q)D_{\pi}(q+k)\\
&-\frac{i}{2}g_{\rho}\int\frac{d^4k}{(2\pi)^4}(\epsilon_{3ba}\Gamma^{(3)}_{\nu\,ab3}(k,-q)-\epsilon_{3ab}\Gamma^{(3)}_{\nu\,ba3}(k+q,-q))D_{\pi}(k).
\end{aligned}\tag{2.15}$$

One can now make the change of variable $k\to k-q$ in the second integral to obtain:

$$\begin{aligned}
q^{\mu}\Sigma_{\rho\,\mu\nu}(q,T) =& \frac{-i}{2}g_{\rho}\int\frac{d^4k}{(2\pi)^4}\epsilon_{3ab}\Gamma^{(3)}_{\nu\,ba3}(q+k,-q)D_{\pi}(k)\\
&-\frac{-i}{2}g_{\rho}\int\frac{d^4k}{(2\pi)^4}\epsilon_{3ab}\Gamma^{(3)}_{\nu\,ba3}(k,-q)D_{\pi}(k)\\
&-\frac{i}{2}g_{\rho}\int\frac{d^4k}{(2\pi)^4}(\epsilon_{3ba}\Gamma^{(3)}_{\nu\,ab3}(k,-q)-\epsilon_{3ab}\Gamma^{(3)}_{\nu\,ba3}(k+q,-q))D_{\pi}(k)\\
&=0.
\end{aligned}\tag{2.16}$$

The shift in k does not violate gauge invairance, because $\Sigma^{\mu\nu}_{\rho}$ is regularized with the Pauli-Villars schema [46].

One can easily show that the Ward identities are satisfied in vacuum. For the $\rho\pi\pi$ vertex one finds:

$$\begin{aligned}
q^{\mu}\Gamma^{(3)}_{\mu\,ab3} &= g_{\rho}\epsilon_{3ab}(2k\cdot q+q^2)=g_{\rho}\epsilon_{3ab}((k+q)^2-m_{\pi}^2-k^2+m_{\pi}^2)\\
&= g_{\rho}\epsilon_{3ab}(D_{\pi}^{-1}(q+k)-D_{\pi}^{-1}(k)),
\end{aligned}\tag{2.17}$$

and for the $\rho\rho\pi\pi$ vertex we start with the right hand side of eq. 2.14 to show:

$$\begin{aligned}
&ig_\rho(\epsilon_{3ca}\Gamma^{(3)}_{\nu\,bc3}(k,-q) - \epsilon_{3bc}\Gamma^{(3)}_{\nu\,ca3}(k+q,-q)) \\
&= ig_\rho(\epsilon_{3ca}\epsilon_{3bc}g_\rho(2k-q)_\nu - \epsilon_{3bc}\epsilon_{3ca}g_\rho(2k+q)_\nu) \\
&= ig_\rho^2\epsilon_{3ca}\epsilon_{3bc}(-2q)_\nu \\
&= ig_\rho^2(\delta_{3a}\delta_{3b} - \delta_{ab})(-2q)_\nu \\
&= i2g_\rho^2(\delta_{ab} - \delta_{3a}\delta_{3b})q^\mu g_{\mu\nu} \\
&= q^\mu\Gamma^{(4)}_{\mu\nu\,ab33}.
\end{aligned} \tag{2.18}$$

Although the Ward identities are satisfied in vacuum, the addition of medium effects within D_π violates the Ward identities and will be addressed in chapter 4.

2.3 In medium rho-self-energy

At finite temperature, the self-energy experiences Bose enhancement. In the imaginary-time formalism, this can be implemented by replacing the energy integration with an infinite summation over discrete Matsubara frequencies (ω_n) [47]:

$$\int \frac{dk_0}{(2\pi)} \to iT\sum_n, \qquad k_0 \to i\omega_n, \qquad \omega_n = \pi nT, \tag{2.19}$$

where n is summed over even integers for bosons and odd integers for fermions. In order to perform the summation, we rewrite propagators using the spectral representation:

$$F(k_0) = \frac{-1}{\pi}\int_{-\infty}^{\infty} dv \frac{\mathrm{Im}[F(v)]}{k_0 - v + i\epsilon}, \tag{2.20}$$

where ϵ is infinitesimally small. Equation 2.20 holds for any analytic function, F, if the real part of F is calculated from the principal value of the integral. At finite temperature $\Sigma_\rho^{\mu\nu}$ is given by:

$$\begin{aligned}\Sigma_\rho^{\mu\nu}(q) =& -g_\rho^2 T \sum_{n(even)} \int \frac{d^3k}{(2\pi)^3} \int_{-\infty}^{\infty} \frac{dvdv'}{\pi^2} \frac{(2k+q)^\mu (2k+q)^\nu \text{Im}[D_\pi(v,\vec{k})]\text{Im}[D_\pi(v',\vec{k}+\vec{q})]}{(i\omega_n - v + i\epsilon)(q_0 + i\omega_n - v' + i\epsilon)} \\ &+ 2g_\rho^2 g^{\mu\nu} T \sum_{n(even)} \int \frac{d^3k}{(2\pi)^3} \int_{-\infty}^{\infty} \frac{dv}{-\pi} \frac{\text{Im}[D_\pi(v,\vec{k})]}{i\omega_n - v + i\epsilon}.\end{aligned} \tag{2.21}$$

One can rewrite the first term using partial fractions such that:

$$\begin{aligned}&\frac{1}{(i\omega_n - v + i\epsilon)(q_0 + i\omega_n - v' + i\epsilon)} \\ &= \frac{1}{q_0 + v - v' + i\epsilon}\Big(\frac{1}{i\omega_n - v + i\epsilon} - \frac{1}{q_0 + i\omega_n - v' + i\epsilon}\Big).\end{aligned} \tag{2.22}$$

The summations can be performed using the identity [51]:

$$T\sum_n \frac{1}{i\omega_n - v + i\epsilon} = -f(v), \tag{2.23}$$

were $f(v)$ is the Bose distribution function for even n, and the Fermi distribution function for odd n. The in medium rho self-energy is then given by:

$$\begin{aligned}\Sigma_\rho^{\mu\nu}(q) =& g_\rho^2 \int \frac{d^3k}{(2\pi)^3} \int_{-\infty}^{\infty} \frac{dvdv'}{\pi^2} \frac{(2k+q)^\mu (2k+q)^\nu}{q_0 + v - v' + i\epsilon} \\ &\text{Im}[D_\pi(v,\vec{k})]\text{Im}[D_\pi(v',\vec{k}+\vec{q})](f(v) - f(v')) \\ &- 2g_\rho^2 g^{\mu\nu} \int \frac{d^3k}{(2\pi)^3} \int_{-\infty}^{\infty} \frac{dv}{-\pi} \text{Im}[D_\pi(v,\vec{k})] f(v).\end{aligned} \tag{2.24}$$

The first term is complex, while the second is purely real. The imaginary part of Σ_ρ can be obtained using the identity:

$$\mathrm{Im}\Big[\frac{1}{\omega - v + i\epsilon}\Big] = (-\pi)\delta(\omega - v), \tag{2.25}$$

resulting in:

$$\begin{aligned}
\mathrm{Im}\Sigma^{\mu\nu}_{\rho}(q) =& g^2_{\rho}\int \frac{d^3k}{(2\pi)^3}\int_{-\infty}^{\infty}\frac{dv}{-\pi}\mathrm{Im}[D_{\pi}(v,\vec{k})]\mathrm{Im}[D_{\pi}(q_0+v,\vec{q}+\vec{k})] \\
& (2k+q)^{\mu}(2k+q)^{\nu}(f(v)-f(q_0+v)) \\
=& g^2_{\rho}\int \frac{d^3k}{(2\pi)^3}\int_{0}^{q_0}\frac{dv}{-\pi}\mathrm{Im}[D_{\pi}(v,\vec{k})]\mathrm{Im}[D_{\pi}(q_0-v,\vec{q}+\vec{k})] \\
& (2k+q)^{\mu}(2k+q)^{\nu}(1+f(v)+f(q_0-v)) \\
& + 2g^2_{\rho}\int \frac{d^3k}{(2\pi)^3}\int_{0}^{\infty}\frac{dv}{-\pi}\mathrm{Im}[D_{\pi}(v,\vec{k})]\mathrm{Im}[D_{\pi}(q_0+v,\vec{q}+\vec{k})] \\
& (2k+q)^{\mu}(2k+q)^{\nu}(f(v)-f(q_0+v)),
\end{aligned} \tag{2.26}$$

where we have made use of the identity,

$$f(-v) = -1 - f(v), \tag{2.27}$$

for the Bose distribution function.

In the second equality we have separated the self-energy into two "cuts". These "cuts" correspond to the imaginary part of the self-energy, and represent different physical processes. The first term is the unitarity cut, which represents the vacuum $\rho \to \pi\pi$ decay and its Bose enhancement. The second term is the Landau cut, which gives the contribution from $\rho\pi$-scattering through an intermediate pion state. The energy dependent portion of the real part of $\Sigma^{\mu\nu}_{\rho}$ can be calculated from a dispersion relation, while a constant shift from the tadpole diagram can be calculated directly, giving:

$$\begin{aligned}\mathrm{Re}\Sigma_\rho^{\mu\nu}(q_0,\vec{q}) =& \frac{-1}{\pi}\mathrm{p.v.}\int_0^\infty dv^2 \frac{1}{q_0^2-v^2}\mathrm{Im}\Sigma_\rho^{\mu\nu}(v,\vec{q}) \\ &- 2g_\rho^2 g^{\mu\nu}\int\frac{d^3k}{(2\pi)^3}\int_{-\infty}^{\infty}\frac{dv}{-\pi}\mathrm{Im}[D_\pi(v,\vec{k})]f(v),\end{aligned} \tag{2.28}$$

where p.v. indicates that one should take the principal value of the integral.

2.4 Transverse projection

In order to calculate the conductivity, we require the transverse projection of $\Sigma_\rho^{\mu\nu}$. We now calculate the transverse projection of $\Sigma_\rho^{\mu\nu}$. The Lorentz structure of $\Sigma_\rho^{\mu\nu}$ is given by the $\rho\pi\pi$ and $\rho\rho\pi\pi$ vertices. For the $\pi\pi$-loop to calculate the transverse projection one must evaluate:

$$\begin{aligned}&\frac{1}{2}P_T^{\mu\nu}(2k+q)^\mu(2k+q)^\nu = \\ &\frac{1}{2}(4\vec{k}^2+4\vec{k}\cdot\vec{q}+\vec{q}^2-4\frac{(\vec{k}\cdot\vec{q})^2}{\vec{q}^2}-4\vec{k}\cdot\vec{q}-\vec{q}^2) = \\ &\frac{1}{2}(4\vec{k}^2-4\frac{(\vec{k}\cdot\vec{q})^2}{\vec{q}^2}) = \\ &2\vec{k}^2(1-\cos(\theta)),\end{aligned} \tag{2.29}$$

where θ is the angle between $\vec{q}$ and $\vec{k}$. It is convenient to align the z-axis with $\vec{q}$, so that θ also corresponds to the angle between k and the z-axis. To calculate the transverse projection of the tadpole loop one must evaluate:

$$\begin{aligned}&\frac{1}{2}P_T^{\mu\nu}g^{\mu\nu} = \\ &\frac{1}{2}(-3+\frac{\vec{q}^2}{\vec{q}^2}) = \\ &-1.\end{aligned} \tag{2.30}$$

The transverse projection of the in medium rho self-energy is then given by:

$$\begin{aligned}\Sigma_\rho^T(q) =& g_\rho^2 \int \frac{d^3k}{(2\pi)^3} \int_{-\infty}^{\infty} \frac{dvdv'}{\pi^2} \frac{2\vec{k}^2(1-\cos(\theta))}{q_0+v-v'+i\epsilon} \\ & \mathrm{Im}[D_\pi(v,\vec{k})]\mathrm{Im}[D_\pi(v',\vec{k}+\vec{q})](f(v)-f(v')) \\ & + 2g_\rho^2 \int \frac{d^3k}{(2\pi)^3} \int_{-\infty}^{\infty} \frac{dv}{-\pi} \mathrm{Im}[D_\pi(v,\vec{k})] f(v).\end{aligned} \tag{2.31}$$

Finally, for $\vec{q}=0$, the explicit θ dependence can be integrated out analytically:

$$\begin{aligned}\Sigma_\rho^T(q_0,\vec{q}) &= g_\rho^2 \frac{8\pi}{3} \int \frac{d|\vec{k}|\vec{k}^2}{(2\pi)^3} \int_{-\infty}^{\infty} \frac{dvdv'}{\pi^2} \frac{2\vec{k}^2}{q_0+v-v'+i\epsilon} \\ & \quad \mathrm{Im}[D_\pi(v,\vec{k})]\mathrm{Im}[D_\pi(v',\vec{k})](f(v)-f(v')) \\ & \quad +2g_\rho^2 \int \frac{d^3k}{(2\pi)^3} \int_{-\infty}^{\infty} \frac{dv}{-\pi} \mathrm{Im}[D_\pi(v,\vec{k})] f(v) \\ &= \frac{g_\rho^2}{3} \int \frac{d^3k}{(2\pi)^3} \int_{-\infty}^{\infty} \frac{dvdv'}{\pi^2} \frac{4\vec{k}^2}{q_0+v-v'+i\epsilon} \\ & \quad \mathrm{Im}[D_\pi(v,\vec{k})]\mathrm{Im}[D_\pi(v',\vec{k})](f(v)-f(v')) \\ & \quad +2g_\rho^2 \int \frac{d^3k}{(2\pi)^3} \int_{-\infty}^{\infty} \frac{dv}{-\pi} \mathrm{Im}[D_\pi(v,\vec{k})] f(v).\end{aligned} \tag{2.32}$$

2.5 On-shell approximation

Now that the transverse projection of the rho self-energy has been established, we will investigate how it generates the transport peak in Π^{EM}. Within the VDM, the conductivity is given by:

$$\sigma_{el} = \frac{-e^2(m_\rho^0)^4}{3g_\rho^2} \lim_{q_0\to 0} \frac{\mathrm{Im}D_\rho^{ii}(q_0,0)}{q_0} = \frac{-e^2(m_\rho^0)^4}{g_\rho^2} \lim_{q_0\to 0} \frac{\mathrm{Im}D_\rho^T(q_0,0)}{q_0}, \tag{2.33}$$

with:

$$\begin{aligned}\mathrm{Im}D_\rho^T(q_0,0) &= \mathrm{Im}[\frac{1}{q_0^2-(m_\rho^0)^2-\Sigma_\rho^T(q_0,0)}] \\ &= \frac{\mathrm{Im}\Sigma_\rho^T(q_0,0)}{(q_0^2-(m_\rho^0)^2-\mathrm{Re}\Sigma_\rho^T(q_0,0))^2+\mathrm{Im}\Sigma_\rho^T(q_0,0)^2}.\end{aligned} \tag{2.34}$$

At zero-energy, $\mathrm{Im}\Sigma_\rho$ must go to zero, due to the retarded nature of the propagator. Furthermore, we will see in chapter 6 that a sum rule requires $\mathrm{Re}\Sigma_\rho$ to return to it's vacuum value at $q_0 = \vec{q} = 0$ [45]. Reference [46] found that the rho self-energy must vanish for $q^2 = 0$ thus the conductivity can be expressed as:

$$\sigma_{el} = \frac{-e^2}{g_\rho^2} \lim_{q_0 \to 0} \frac{\mathrm{Im}\Sigma_\rho^T(q_0, 0)}{q_0}. \tag{2.35}$$

From eq. 2.35 one sees that σ_{el} is proportional to $\mathrm{Im}\Sigma_\rho$, which is in turn generated by two physical processes: $\rho \to \pi\pi$ decay and $\rho\pi$-scattering. For sharp pion propagators, $\rho \to \pi\pi$ decays cannot occur unless the rho's invariant mass is greater than two times the pion mass, due to conservation of energy. For finite pion widths, the rho's unitarity cut gains strength below the 2-pion threshold, because the pions do not need to be on-shell. However, the conductivity is calculated in the zero energy limit, and the typical pion width ($\approx 25\,\mathrm{MeV}$ at $T = 150\,\mathrm{MeV}$) [48] is significantly smaller than the pion mass (140 MeV). Thus, even when a pion width is included, the unitarity cut's contribution to the conductivity is expected to be small. The Landau cut corresponds to $\rho\pi$ scattering through an intermediate pion, $\rho\pi \to \pi$. However, at finite energy and zero momentum this interaction is once again forbidden for sharp pions, because, for $\vec{q} = 0$, the pions in the final and initial states have the same 4-momentum. Thus, any additional energy added to the initial state by the photon will violate conservation of 4-momentum. This interaction is allowed for $q_0 = 0$, however the self-energy is infinite at this point. This is precisely what was found in ref. [35], where the spectral function developed a delta function at $q_0 = 0$ for zero coupling. The solution is to include the pion's interactions with the medium, smearing out the delta function, thus generating a finite conductivity.

The Landau cut provides the dominant contribution to the conductivity. If one inserts the

transverse projection of the Landau cut into eq. 2.35 one finds:

$$\sigma_{el} = \lim_{q_0\to 0}\Big[\frac{-2e^2}{3q_0}\int\frac{d^3k}{(2\pi)^3}\int_0^\infty\frac{dv}{-\pi}\mathrm{Im}[D_\pi(v,\vec{k})]\mathrm{Im}[D_\pi(q_0+v,\vec{k})] \\ 4|\vec{k}|^2(f(v)-f(q_0+v))\Big]. \tag{2.36}$$

The limit can be performed analytically using L'Hospital's rule:

$$\lim_{q_0\to 0}\frac{1}{q_0}(f(v)-f(q_0+v)) = \frac{e^{\frac{v}{T}}}{T(-1+e^{\frac{v}{T}})^2}. \tag{2.37}$$

The conductivity is then given by:

$$\sigma_{el} = \frac{-2e^2}{3q_0}\int\frac{d^3k}{(2\pi)^3}\int_0^\infty\frac{dv}{-\pi}\mathrm{Im}[D_\pi(v,\vec{k})]^2\frac{4|\vec{k}|^2e^{\frac{v}{T}}}{T(-1+e^{\frac{v}{T}})^2}. \tag{2.38}$$

As a first approximation, we calculate the conductivity using a small, but finite, pion width Γ_π. The pion propagator is then given by:

$$D_\pi(k) = \frac{1}{2\omega_k}\Big(\frac{1}{k_0-\omega_k+i\frac{\Gamma_\pi}{2}}-\frac{1}{k_0+\omega_k+i\frac{\Gamma_\pi}{2}}\Big), \tag{2.39}$$

with $\omega_k = \sqrt{k^2+m_\pi^2}$. For small widths and positive k_0 $\mathrm{Im}[D_\pi]$ is dominated by the first term in eq. 2.40, because the second term does not contain a pole. Therefore, one can express the imaginary part of the pion propagator as:

$$\mathrm{Im}D_\pi(k) \approx \frac{1}{2\omega_k}\mathrm{Im}\Big[\frac{1}{k_0-\omega_k+i\frac{\Gamma_\pi}{2}}\Big] = \frac{-\Gamma_\pi}{4\omega_k}\frac{1}{(k_0-\omega_k)^2+\frac{\Gamma_\pi^2}{4}}. \tag{2.40}$$

For sharp pions, the propagator can be expressed in terms of a Dirac δ-function:

$$\mathrm{Im}[D(k)] = \frac{-\pi}{2\omega_k}\delta(k_0-\omega_k). \tag{2.41}$$

It is straight forward to derive equation 2.41. First, we note that as Γ_π approaches zero, $\mathrm{Im}[D(k)]$

goes to zero for all k_0 except $k_0 = \omega_k$, where it is infinite. Next, we integrate $\mathrm{Im}[D(k)]$ over all k_0:

$$\begin{aligned}
&\int_{-\infty}^{\infty} dk_0 \frac{-\Gamma_\pi}{4\omega_k} \frac{1}{(k_0-\omega_k)^2 + \frac{\Gamma_\pi^2}{4}} \\
&= \lim_{k_0\to\infty} \frac{1}{2\omega_k}\Big[\mathrm{ArcTan}\big(\frac{2(\omega_k - k_0)}{\Gamma_\pi}\big) - \mathrm{ArcTan}\big(\frac{2(\omega_k + k_0)}{\Gamma_\pi}\big)\Big] \\
&= \frac{-\pi}{2\omega_k}.
\end{aligned} \tag{2.42}$$

From eq. 2.42 one sees that the sharp pion propagator satisfies the definition of a delta function times $\frac{-\pi}{2\omega_k}$.

To obtain a finite conductivity we must derive an expression similar to eq. 2.41 for $\mathrm{Im}[D(k)]^2$, in the small width limit. To begin, we write the imaginary part of the propagator squared, while dropping the terms in D_π that do not contain a pole:

$$\mathrm{Im}[D(k)]^2 \;\approx\; \Big(\frac{-\Gamma_\pi}{4\omega_k}\frac{1}{(k_0-\omega_k)^2 + \frac{\Gamma_\pi^2}{4}}\Big)^2. \tag{2.43}$$

It is easy to see that for small widths $\mathrm{Im}[D(k)]^2$ approaches zero away from the pole. To relate $\mathrm{Im}[D(k)]^2$ to a delta function we must determine how $\mathrm{Im}[D(k)]^2$ behaves when integrated over k_0. If one integrates $\mathrm{Im}[D(k)]^2$ over all k_0 one finds:

$$\begin{aligned}
&\int_{-\infty}^{\infty} dk_0 \Big(\frac{-\Gamma_\pi}{4\omega_k}\frac{1}{(k_0-\omega_k)^2 + \frac{\Gamma_\pi^2}{4}}\Big)^2 \\
&= \lim_{k_0\to\infty} \frac{1}{4\omega_k^2}\Big[\frac{1}{2}\frac{(-\omega_k + k_0)}{(\frac{\Gamma_\pi}{2})^2 + (\omega_k - k_0)^2} - \frac{1}{\Gamma_\pi}\mathrm{ArcTan}\big(\frac{2(\omega_k - k_0)}{\Gamma_\pi}\big) \\
&\quad -\frac{1}{2}\frac{(-\omega_k - k_0)}{(\frac{\Gamma_\pi}{2})^2 + (\omega_k + k_0)^2} + \frac{1}{\Gamma_\pi}\mathrm{ArcTan}\big(\frac{2(\omega_k + k_0)}{\Gamma_\pi}\big)\Big] \\
&= \frac{\pi}{4\omega_k^2}\frac{1}{\Gamma_\pi}.
\end{aligned} \tag{2.44}$$

The definition of the Dirac delta function and eq. 2.44 imply that for small Γ_π:

$$\mathrm{Im}[D(k)]^2 \approx \frac{\pi}{4\omega_k^2}\frac{1}{\Gamma_\pi}\delta(k_0 - \omega_k). \tag{2.45}$$

Equation 2.45 allows one to approximate one propagator with a delta function, without dropping the second propagator's width. Therefore, it can be used in eq. 2.38 without producing and infinite conductivity. One can now use eqs. 2.45 and 2.38 to show:

$$\sigma_{el} = \frac{2e^2}{3T}\int \frac{d^3\vec{k}}{(2\pi)^3}\frac{v_k^2}{\Gamma_\pi} f(\omega_k)(1+f(\omega_k)), \tag{2.46}$$

where $v_k = \frac{\vec{k}}{\omega_k}$ is the pion's velocity.

Reference [49] calculated the conductivity by solving the Boltzmann equation in the relaxation time approximation:

$$\sigma_{el} = \frac{1}{3T}\sum_i e_i^2 n_i \tau, \tag{2.47}$$

where i is summed over all particle species in the medium, e_i and n_i are the charge and density for a given species, respectively, and τ is the mean time between collisions. For a pion gas equation 2.47 is summed over the three iospin states of the pion. Only two of the isospin states are charged, so after the summation eq. 2.47 will increase by a factor of two rather than three. This result is similar to what we find in 2.46, if one replaces the collision time with $\frac{v_k^2}{\Gamma_\pi}$. We note that we pick up the factor of v_k^2 due to relativistic effects. Furthermore, our approximate conductivity agrees with similar calculations in references [23, 30], which express the conductivity in terms of the pion width.

2.6 Constant pion width

The approximate conductivity in section 2.5 requires the pion's width to be small. As the width increases the approximation breaks down. In fact, eq. 2.46 approaches zero for large Γ_π, and thus would violate any potential quantum lower-bound, in the strong-coupling limit. To obtain a non-zero conductivity in the strong-coupling limit one must dress both pion propagators with a constant

width. For an arbitrary width the pion propagator is given by:

$$D_\pi(k) = \frac{1}{k_0^2 - \vec{k}^2 - m_\pi^2 + ik_0\Gamma_\pi}. \tag{2.48}$$

We use eqs. 2.36 and 2.48 to calculate the conductivity with two dressed pion propagators, integrating over off-shell effects. Figure 2.2 displays how the conductivity varies with width for a constant temperature of T=150 MeV. While the sharp pion approximation works well for widths below approximately $100\,\text{MeV}$, the results diverge as the width increases. This discrepancy indicates that one must perform the full quantum calculation to study the strong-coupling limit of the medium.

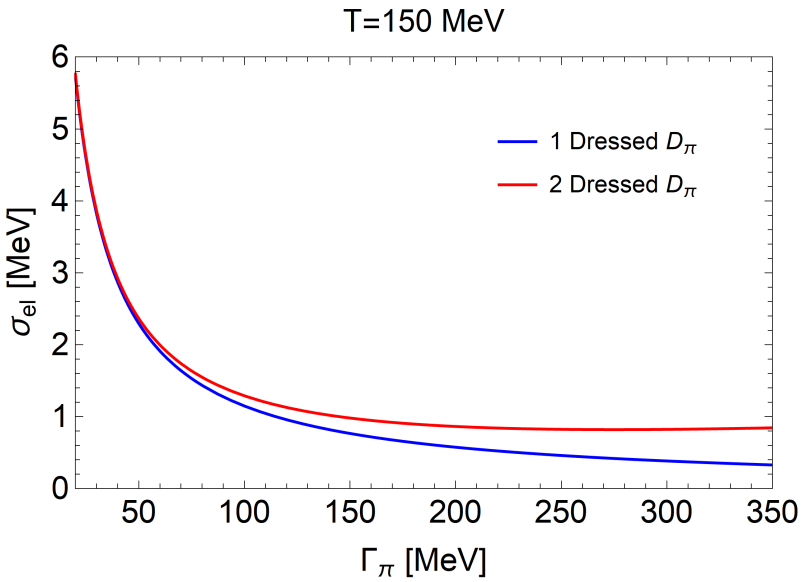

Figure 2.2: Electric conductivity for a fixed temperature of 150 MeV, plotted as a function of the pion width, Γ_π. The blue line shows the result when the imaginary part of one pion propagator is approximated with a delta function, and the second propagator is dressed with a constant width. The red line shows the result when both propagators are dressed with constant widths.

3. PION SELF-ENERGY

As emphasized in section 2.5, the pion's medium interactions are essential to extract a finite conductivity. Therefore thermal $\pi\pi$-scattering plays a decisive role in calculating the conductivity at low temperature and chemical potential. In this chapter, we calculate the pion self-energy due to thermal S- and P-wave $\pi\pi$-scattering. The resonant scattering model is able to describe S- and P-wave $\pi\pi$ interactions up to about 1 GeV [50]. Such scatterings occur predominantly through sigma and rho resonances, respectively. These resonant scattering as shown diagrammatically in fig. 3.1.

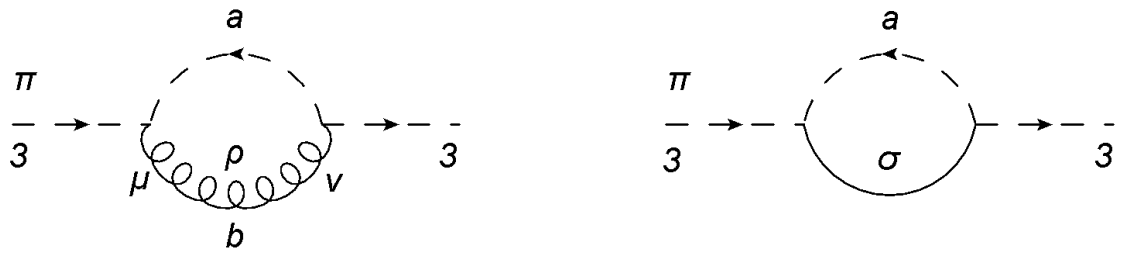

Figure 3.1: The pion self-energy resulting from resonant scattering of a pion with a thermal pion through an intermediate ρ (left) or σ (right) meson.

In section 3.1 we show how one can resum self-energy loops into the pion propagator. In section 3.2 we calculate the pion self-energy due to the rho resonance, using the previously established Lagrangian from eq. 2.2. In Section 3.3 we calculate the pion self-energy due to the sigma resonance, following the approach used in refs. [50, 51]. In section 3.4 we fit our parameters to the measured S- and P- wave phase shifts, and compare our $\pi\pi$-cross section to the experimentally measured cross section. Finally, in sections 3.5 we calculate the pion self-energy at finite temperature.

3.1 Dressed pion propagator

In chapter 1 the resummed pion propagator (eq. 1.18) was introduced without justification. Equation 1.18 can be derived from an infinite summation of interaction loops, as illustrated in figure 3.2.

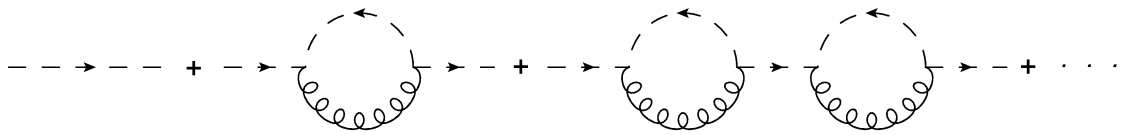

Figure 3.2: Above: Pion propagator dressed with the self-energy from $\pi\pi$ resonant scattering through a rho resonance. The propagator is resummed to infinite order in the interaction loop.

Figure 3.2 can be written as [51]:

$$D_\pi(k) = D^0_\pi(k) + D^0_\pi \Sigma_\pi(k) D_\pi(k), \tag{3.1}$$

where $D^0_\pi(k)$ is the vacuum pion propagator. Equation 3.1 can then be rewritten in a closed form expression:

$$\begin{aligned} D_\pi(k) &= D^0_\pi(k) \sum_{n=0}^{\infty} (\Sigma(k) D^0_\pi(k))^n \\ &= D^0_\pi(k) \frac{1}{1 - \Sigma_\pi(k) D^0_\pi(k)} \\ &= \frac{1}{k_0^2 - \vec{k}^2 - m_\pi^2 - \Sigma_\pi(k)}. \end{aligned} \tag{3.2}$$

Thus, one can see that eq. 1.18 dresses the pion propagator with interaction loops to infinite order.

3.2 Rho resonance

In this section we calculate the pion self-energy due to the rho resonance. The $\rho\pi\pi$ vertex was established in chapter 2 along with the rho and pion propagators. One can use the vertex and

propagators, along with standard Feynman rules, to construct the pion self-energy for $\pi\pi$-scattering through a rho resonance. With this approach one obtains:

$$\begin{aligned}\Sigma_{\pi(\rho)}(k,T) &= -\frac{g_\rho^2\epsilon_{3ab}\epsilon_{3ab}}{2}T\sum_{n(even)}\int\frac{d^3p}{(2\pi)^3}\Big[(k-p)_\mu(k-p)_\nu D_\rho^{\mu\nu}(p+k) \\ &\quad D_\pi(p)\tilde{\mathrm{FF}}_\rho[q_{\mathrm{CM}}]^2\Big]_{p_0=i\omega_n}, \end{aligned} \tag{3.3}$$

where we have added a symmetry factor of $\frac{1}{2}$, as was also the case for the rho self-energy. We also add a form factor $\tilde{\mathrm{FF}}_\rho[q_{\mathrm{CM}}]$ at each vertex, because regularizing the pion self-energy using the Pauli-Villars scheme presents significant numerical difficulty. Thus we opt for a simpler form factor defined as:

$$\tilde{\mathrm{FF}}_\rho[q_{\mathrm{CM}}] = \frac{\Lambda_\rho^2+m_\rho^2}{\Lambda_\rho^2+4(m_\pi^2+q_{\mathrm{CM}}[p,k]^2)}, \tag{3.4}$$

$$q_{\mathrm{CM}}[p,k]^2 = \frac{1}{(p+k)^2}\big(\frac{1}{4}((p+k)^2-k^2-p^2)^2-k^2p^2\big), \tag{3.5}$$

where q_{CM} is the center of mass momentum and Λ_ρ is the form factor cutoff, which will be fit to scattering data in section 3.4. It is convenient to redefine our cutoff parameters, so that the form factor is more similar to that used in ref. [46]. Thus we define:

$$\mathrm{FF}_\rho[p,k] = \tilde{\mathrm{FF}}_\rho[q_{\mathrm{CM}}] = \frac{\Lambda_{1\rho}^2}{\Lambda_{2\rho}^2+q_{\mathrm{CM}}[p,k]^2}, \tag{3.6}$$

$$\Lambda_{1\rho} = \sqrt{\frac{\Lambda_\rho^2+m_\rho^2}{4}}, \tag{3.7}$$

$$\Lambda_{2\rho} = \sqrt{\frac{\Lambda_\rho^2}{4}+m_\pi^2}. \tag{3.8}$$

However, we stress that the two form factors $\tilde{\mathrm{FF}}_\rho[q_{\mathrm{CM}}]$ and $\mathrm{FF}_\rho[p,k]$ are equivalent. Finally, we note that for $D_\rho^{\mu\nu}$ we use the vacuum rho propagator established in eq. 2.10.

3.3 Sigma resonance

We have not established a $\sigma\pi\pi$ vertex, so in order to calculate the pion self-energy due to scattering through a sigma resonance, we follow the approach outlined in references [50, 51]. We begin with the interaction Lagrangian for the linear sigma model [32, 51, 52, 53]:

$$\mathcal{L}^{int}_{\pi\pi\sigma} = -\frac{g_\sigma^2}{2} f_\pi \vec{\pi}^2 \sigma - \frac{g_\sigma^2}{8}(\vec{\pi}^2)^2. \tag{3.9}$$

The I=0 Born amplitude is given by [52]:

$$M^{I=0}_{B,\pi\pi\sigma}(s,t,u) = g_\sigma^2\Big(3\frac{s-m_\pi^2}{s-m_\sigma^2} + \frac{t-m_\pi^2}{t-m_\sigma^2} + \frac{u-m_\pi^2}{u-m_\sigma^2}\Big), \tag{3.10}$$

where m_σ is the bare sigma mass and s, t, and u are the Mandelstam variables. Reference [50] created a separable potential using an off-shell continuation of the Mandelstam variables in which the pion energies in t and u where placed on their mass shell, while s was kept as an external variable in the scattering equation. In this continuation the Mandelstam variables become:

$$\begin{aligned} s &= E^2, \\ t &= 2m_\pi^2 - 2\omega_q\omega_{q'} + \vec{q}\cdot\vec{q}', \\ u &= 2m_\pi^2 - 2\omega_q\omega_{q'} - \vec{q}\cdot\vec{q}', \end{aligned} \tag{3.11}$$

where E is the invariant mass of the sigma meson, and q and q' are the center-of-mass momenta of the incoming and outgoing pions. Here, we deviate from references [50, 51] by only considering the first term in eq. 3.10. We make this approximation because t and u channels yield non-resonant terms ($t, u << m_\sigma^2$) in eq. 3.10, which are suppressed by $\frac{1}{m_\sigma^2}$. Therefore, we use the interaction kernel:

$$V^{00}_{\pi\pi\sigma}(E,q,q') = 3g_\sigma^2 \frac{E^2-m_\pi^2}{E^2-m_\sigma^2} \tilde{\text{F}}\text{F}_\sigma[q]\tilde{\text{F}}\text{F}_\sigma[q'], \tag{3.12}$$

where $\tilde{\text{FF}}_\sigma[q]$ is the $\sigma\pi\pi$ form factor given by:

$$\tilde{\text{FF}}_\sigma[q_{\text{CM}}] = \frac{\Lambda_\sigma^2}{\Lambda_\sigma^2 + 4(m_\pi^2 + q_{\text{CM}}[p,k]^2)}, \tag{3.13}$$

$$\text{FF}_\sigma[p,k] = \frac{\Lambda_{1\sigma}^2}{\Lambda_{2\sigma}^2 + q_{\text{CM}}[p,k]^2}, \tag{3.14}$$

$$\Lambda_{1\sigma} = \frac{\Lambda_\sigma}{2}, \tag{3.15}$$

$$\Lambda_{2\sigma} = \sqrt{\frac{\Lambda_\sigma^2}{4} + m_\pi^2}, \tag{3.16}$$

where we again provide two equivalent parameterizations for the form factor, to make latter comparisons to ref. [46] more convenient. One can obtain the partial wave scattering amplitude for a given spin-isospin channel using the Lippmann Schwinger equation:

$$\begin{aligned} M_{\pi\pi}^{\text{JI}}(E,q,q') &= V_{\pi\pi}^{\text{JI}}(E,q,q') \\ &\quad + \int_0^\infty \frac{dkk^2}{(2\pi)^2} V_{\pi\pi}^{\text{JI}}(E,q,k) G_{\pi\pi}(E,k) M_{\pi\pi}^{\text{JI}}(E,k,q'). \end{aligned} \tag{3.17}$$

Here J and I denote the spin and isospin of the $\pi\pi$-scattering channel, respectively, and $G_{\pi\pi}(E,k)$ is the 2-pion propagator:

$$G_{\pi\pi}(E,k) = \frac{1}{\omega_k} \frac{1}{E^2 - 4\omega_k^2 + i\epsilon}. \tag{3.18}$$

For a separable potential, $V(q,q') = v(q)v(q')$, one can resum equation 3.17 to obtain:

$$M_{\pi\pi}^{\text{JI}}(E,q,q') = \frac{3g_\sigma^2(E^2 - m_\pi^2)}{E^2 - m_\sigma^2 - \Sigma_\sigma(E)} \tilde{\text{FF}}_\sigma[q] \tilde{\text{FF}}_\sigma[q'], \tag{3.19}$$

where $\Sigma_\sigma(E)$ is the sigma self-energy, given by:

$$\Sigma_\sigma(E) = 3g_\sigma^2 \int \frac{d|\vec{k}|\vec{k}^2}{(2\pi)^2} \frac{(E^2 - m_\pi^2)\tilde{\text{FF}}_\sigma[k]^2}{\omega_k(E^2 - 4\omega_k^2 + i\epsilon)}. \tag{3.20}$$

Figure 3.3 displays the Feynman diagram corresponding to $\Sigma_\sigma(E)$.

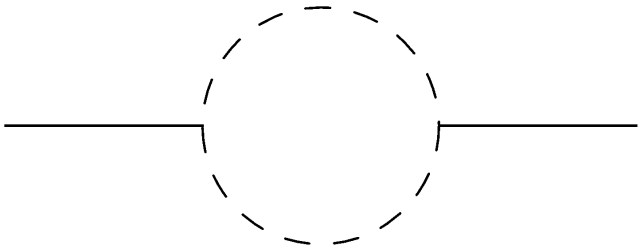

Figure 3.3: Vacuum sigma self-energy from a $\pi\pi$-loop.

The forward scattering amplitude can now be used to calculate the pion self-energy [48]:

$$\Sigma_\pi(k) = -T \sum_{n(even)} \int \frac{d^3p}{(2\pi)^3} \Big[M_{\pi\pi}(p+k, q_{\text{CM}}, q_{\text{CM}}) D_\pi(p) \Big]_{p_0 = i\omega_n}, \tag{3.21}$$

where the forward scattering amplitude ($M_{\pi\pi}$) is calculated by summing $M^{IJ}_{\pi\pi}$ over all relevant spin-isospin channels using [51]:

$$M_{\pi\pi}(E, q, q') = \frac{1}{6} \sum_J \sum_I (2J+1)(2I+1) M^{JI}_{\pi\pi}(E, q, q'). \tag{3.22}$$

In this section we only calculate the pion self-energy due to the sigma resonance ($\Sigma_{\pi(\sigma)}$), thus we only include the $J = 0$, $I = 0$ channel and obtain:

$$\begin{aligned} \Sigma_{\pi(\sigma)}(k, T) &= -\frac{1}{6} T \sum_{n(even)} \int \frac{d^3p}{(2\pi)^3} \Big[M^{00}_{\pi\pi}(p+k, q_{\text{CM}}, q_{\text{CM}}) D_\pi(p) \Big]_{p_0 = i\omega_n} \\ &= -g_\sigma^2 T \sum_{n(even)} \int \frac{d^3p}{(2\pi)^3} \Big[\frac{((p+k)^2 - m_\pi^2)}{2} D_\sigma(p+k) \\ &\quad D_\pi(p) \text{FF}_\sigma[p, k]^2 \Big]_{p_0 = i\omega_n}, \end{aligned} \tag{3.23}$$

where D_σ is the vacuum sigma propagator:

$$D_\sigma(E) = \frac{1}{E^2 - m_\sigma^2 - \Sigma_\sigma(E)}. \tag{3.24}$$

Finally, we note that in ref. [51] the off-shell continuation of the Mandelstam variables was also used to calculate P-wave scattering through the rho resonance. We do not use this off-shell continuation when calculating $\Sigma_{\pi(\rho)}$, in order to maintain consistency with the $\rho\pi\pi$ vertex from ref. [46], however for on-shell pions our self-energy is identical to the result from ref. [51]

3.4 Vacuum fits

Next, we compare our scattering amplitudes to experimental measurements. The forward scattering amplitude for a given spin-isospin channel is related to the propagator for a given resonance through:

$$M^{00}_{\pi\pi}(E, q_{\text{CM}}, q_{\text{CM}}) = \frac{g_\sigma^2}{2}(E^2 - m_\pi^2)D_\sigma(E)\tilde{\text{FF}}_\sigma[q'_{\text{CM}}]^2 \tag{3.25}$$

$$M^{11}_{\pi\pi}(E, q_{\text{CM}}, q_{\text{CM}}) = g_\rho^2(E^2 - 4m_\pi^2)D_\rho(E)\tilde{\text{FF}}_\rho[q'_{\text{CM}}]^2. \tag{3.26}$$

For comparisons to vacuum data we take the pion energies k_0 and p_0 to be on-shell, but keep the resonant particle's energy, E, as an external variable. The center of mass momentum is then given by:

$$q'_{\text{CM}}[\sqrt{s}] = \frac{1}{s}\big(\frac{1}{4}(s - 2m_\pi^2)^2 - m_\pi^4\big). \tag{3.27}$$

The parameters: g_σ, m_σ, and $\Lambda_{(\rho/\sigma)}$ can be fit to S- and P-wave $\pi\pi$-scattering phase shifts [54]. The $\pi\pi$-scattering phase shifts are related to the sigma and rho propagators by [55]:

$$\tan\delta_0^0(E) = \frac{\text{Im}[D_\rho(E)]}{\text{Re}[D_\rho(E)]}, \tag{3.28}$$

$$\tan\delta_1^1(E) = \frac{\text{Im}[D_\sigma(E)]}{\text{Re}[D_\sigma(E)]}. \tag{3.29}$$

In order to fit Λ_ρ we cannot use the previously established $\Sigma_\rho^{\mu\nu}$ in eq. 3.28. This is because $\Sigma_\rho^{\mu\nu}$ was regularized with Pauli-Villars regularization, thus it is independent of Λ_ρ. Instead, we define a

new rho self-energy regularized with FF_ρ for use in 3.28:

$$\Sigma_\rho'^{\mu\nu}(q) = ig_\rho^2 \int \frac{d^4k}{(2\pi)^4} \frac{(2k+q)^\mu (2k+q)^\nu}{(k^2 - m_\pi^2 + i\epsilon)((k+q)^2 - m_\pi^2 + i\epsilon)} \tilde{\text{FF}}_\rho[k]^2. \tag{3.30}$$

We must also refit $m_\rho^{(0)}$ within D_ρ, since we neglect the tadpole diagram in $\Sigma_\rho'^{\mu\nu}$. $\Sigma_\rho'^{\mu\nu}$ is only used to fit Λ_ρ, while $\Sigma_\rho^{\mu\nu}$ is used for the rest of this work, in order to maintain consistency with [40, 46]. The resulting fits are given in figure 3.4.

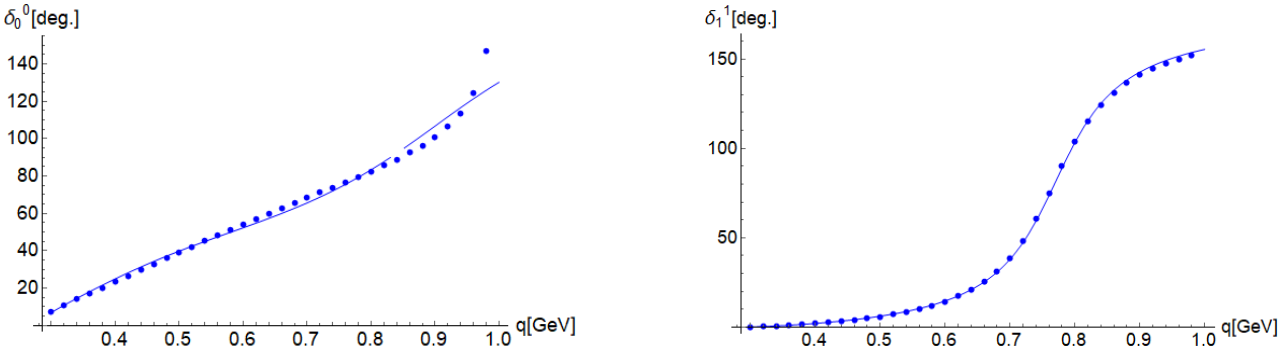

Figure 3.4: Left: Fit for $\Sigma_{\pi(\sigma)}$ to the S-wave phase shift. Right: Fit for $\Sigma_{\pi(\rho)}$ to the P-wave phase shift. Data are taken from ref. [54].

The fits provide the values: $g_\sigma = 8.86$, $m_\sigma = 934$ MeV, $\Lambda_\rho = 1.85$ GeV, and $\Lambda_\sigma = .745$ GeV. Finally, we compare our cross-section with the experimentally measured $\pi\pi$-scattering cross-section. The imaginary part of the forward scattering amplitude is related to the cross-section by:

$$\sigma_{\pi\pi}(s) = \frac{1}{\sqrt{s(s-4m_\pi^2)}} \text{Im}[M_{\pi\pi}(\sqrt{s})], \tag{3.31}$$

or in terms of the ρ and σ propagators:

$$\begin{aligned}\sigma_{\pi\pi}(s) &= \frac{1}{\sqrt{s(s-4m_\pi^2)}}\Big(- g_\rho^2 \mathrm{Im}[D_\rho(\sqrt{s})](s-4m_\pi^2)\mathrm{FF}_\rho[q'_{\mathrm{CM}}]^2 \\ &\quad + \frac{-g_\sigma^2}{2}\mathrm{Im}[D_\sigma(\sqrt{s})](s-m_\pi^2)\mathrm{FF}_\sigma[q'_{\mathrm{CM}}]^2\Big). \end{aligned} \tag{3.32}$$

Figure 3.5 compares our cross-section to experimental measurements taken from ref. [56], and to the cross sections used by ref. [29] for their K-matrix formulation, as well as the cross-sections used in refs. [23, 21].

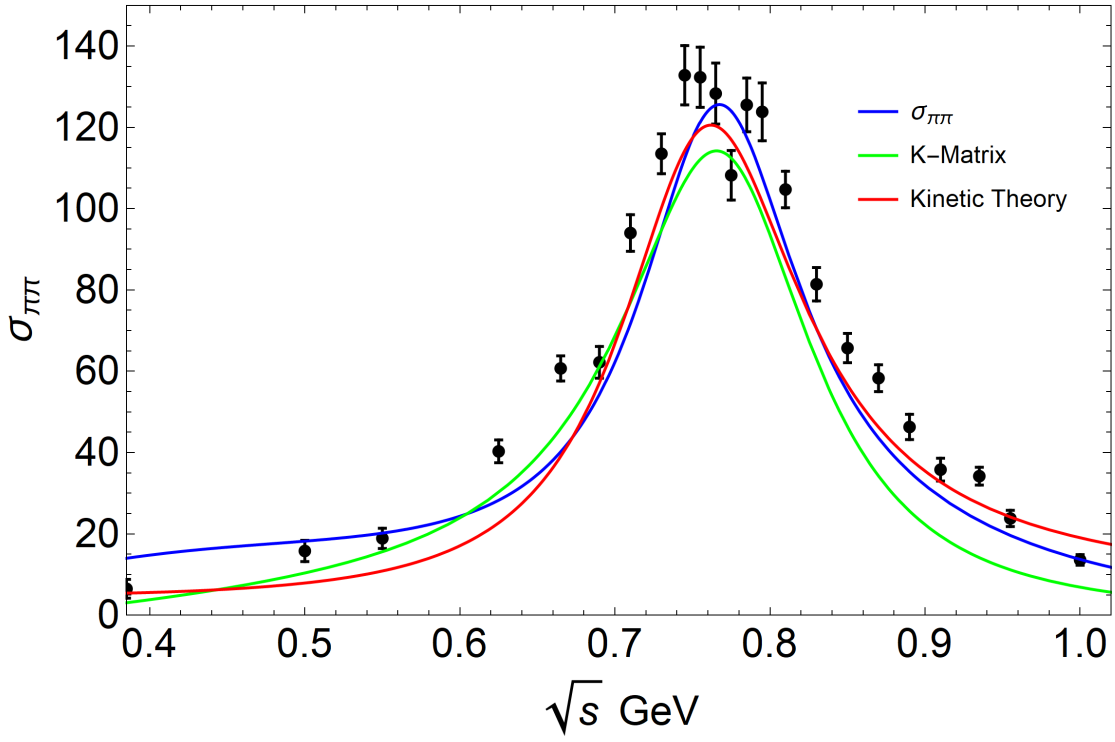

Figure 3.5: Comparison of our $\pi\pi$ cross-section (blue) to experimental data (black dots) from ref. [56] and cross sections used in previous calculations: kinetic theory (red) [21], K-matrix (green) [29]. For the K-matrix we plot only ref. [29]'s lowest lying resonance, the rho meson.

Our cross section is closest to the cross section used in the kinetic theory calculation, however our cross section is larger for $\sqrt{s} \lesssim 600$ MeV, and has a narrower rho peak. For $\sqrt{s} \lesssim 600$ MeV

our cross sections is increased due to the sigma resonance. Our cross section is narrower than experimental data, because in eq. 3.32 we use the vacuum rho propagator from ref. [46]. Reference [46] fit D_ρ to the pion electromagnetic form factor as well as the P-wave phase shift. As a result, D_ρ produces a narrower cross section, but the fit to the pion electromagnetic form factor is improved.

3.5 Pion self-energy at finite temperature

In this section, we calculate the pion self-energy at finite temperature. As was the case for the rho self-energy, the Matsubara sums in eqs. 3.3 and 3.23 can be performed using eq. 2.23, if one rewrites the propagators using a spectral representation. After performing the Lorentz contractions and the summations, we obtain:

$$\begin{aligned}
\Sigma_{\pi(\rho)}(k,T) &= g_\rho^2 \int \frac{d^3p}{(2\pi)^3} \int_{-\infty}^{\infty} \frac{dw}{-\pi} \int_{-\infty}^{\infty} \frac{dw'}{-\pi} \Big[\mathrm{Im}[D_\pi(w,\vec{p})] \mathrm{Im}[D_\rho(w',\vec{k}+\vec{p})] \\
&\quad \frac{N_{\pi(\rho)}[p,k,w']}{k_0+w-w'+i\epsilon} (f(w)-f(w')) \mathrm{FF}_\rho[p,k]^2 \Big]_{p_0=w}, \qquad (3.33) \\
\Sigma_{\pi(\sigma)}(k,T) &= g_\sigma^2 \int \frac{d^3p}{(2\pi)^3} \int_{-\infty}^{\infty} \frac{dw}{-\pi} \int_{-\infty}^{\infty} \frac{dw'}{-\pi} \Big[\mathrm{Im}[D_\pi(w,\vec{p})] \mathrm{Im}[D_\sigma(w',\vec{k}+\vec{p})] \\
&\quad \frac{N_{\pi(\sigma)}[p,k,w']}{k_0+w-w'+i\epsilon} (f(w)-f(w')) \mathrm{FF}_\sigma[p,k]^2 \Big]_{p_0=w}, \qquad (3.34)
\end{aligned}$$

where,

$$\begin{aligned}
N_{\pi(\rho)}[p,k,w'] &= -(k-p)^2 + \frac{(k^2-p^2)^2}{w'^2-(\vec{p}+\vec{k})^2}, \qquad (3.35) \\
N_{\pi(\sigma)}[p,k,w'] &= \frac{w'^2-(\vec{k}+\vec{p})^2-m_\pi^2}{2}. \qquad (3.36)
\end{aligned}$$

The imaginary part of the self-energy can be calculated using eq. 2.25. As was done for $\Sigma_\rho^{\mu\nu}$, we can split the imaginary part of the pion self-energy into various cuts. For the rho resonance we

define:

$$\begin{aligned}\mathrm{Im}\Sigma^{\mathrm{U1}}_{\pi\rho}(k,T) &= g_\rho^2 \int \frac{d^3p}{(2\pi)^3}\int_0^\infty \frac{dw}{-\pi}\Big[-\Theta(k_0-w)\mathrm{Im}[D_\pi(p)]\mathrm{Im}[D_\rho(k+p)] \\ &\quad N_{\pi(\rho)}[p,k,p_0+k_0]\mathrm{FF}_\rho[p,k]^2(1+f(w)+f(k_0-w))\Big]_{p_0=-w}, \qquad (3.37)\end{aligned}$$

$$\mathrm{Im}\Sigma^{\mathrm{U2}}_{\pi\rho}(k,T) = -\mathrm{Im}\Sigma^{\mathrm{U1}}_{\pi\rho}(k,T)\big|_{k_0\to -k_0}, \qquad (3.38)$$

$$\begin{aligned}\mathrm{Im}\Sigma^{\mathrm{L1}}_{\pi\rho}(k,T) &= g_\rho^2 \int \frac{d^3p}{(2\pi)^3}\int_0^\infty \frac{dw}{-\pi}\Big[\Theta(k_0+w)\mathrm{Im}[D_\pi(p)]\mathrm{Im}[D_\rho(k+p)] \\ &\quad N_{\pi(\rho)}[p,k,p_0+k_0]\mathrm{FF}_\rho[p,k]^2(f(w)-f(k_0+w))\Big]_{p_0=w}, \qquad (3.39)\end{aligned}$$

$$\mathrm{Im}\Sigma^{\mathrm{L2}}_{\pi\rho}(k,T) = -\mathrm{Im}\Sigma^{\mathrm{L1}}_{\pi\rho}(k,T)\big|_{k_0\to -k_0}. \qquad (3.40)$$

and for the σ-resonance:

$$\begin{aligned}\mathrm{Im}\Sigma^{\mathrm{U1}}_{\pi\sigma}(k,T) &= \frac{g_\sigma^2}{2} \int \frac{d^3p}{(2\pi)^3}\int_0^\infty \frac{dw}{-\pi}\Big[-\Theta(k_0-w)\mathrm{Im}[D_\pi(p)]\mathrm{Im}[D_\sigma(k+p)] \\ &\quad N_{\pi(\sigma)}[p,k,p_0+k_0]\mathrm{FF}_\sigma[p,k]^2(1+f(w)+f(k_0-w))\Big]_{p_0=-w}, \qquad (3.41)\end{aligned}$$

$$\mathrm{Im}\Sigma^{\mathrm{U2}}_{\pi\sigma}(k,T) = -\mathrm{Im}\Sigma^{\mathrm{U1}}_{\pi\sigma}(k,T)\big|_{k_0\to -k_0}, \qquad (3.42)$$

$$\begin{aligned}\mathrm{Im}\Sigma^{\mathrm{L1}}_{\pi\sigma}(k,T) &= \frac{g_\sigma^2}{2} \int \frac{d^3p}{(2\pi)^3}\int_0^\infty \frac{dw}{-\pi}\Big[\Theta(k_0+w)\mathrm{Im}[D_\pi(p)]\mathrm{Im}[D_\sigma(k+p)] \\ &\quad N_{\pi(\sigma)}[p,k,p_0+k_0]\mathrm{FF}_\sigma[p,k]^2(f(w)-f(k_0+w))\Big]_{p_0=w}, \qquad (3.43)\end{aligned}$$

$$\mathrm{Im}\Sigma^{\mathrm{L2}}_{\pi\sigma}(k,T) = -\mathrm{Im}\Sigma^{\mathrm{L1}}_{\pi\sigma}(k,T)\big|_{k_0\to -k_0}. \qquad (3.44)$$

Equations 3.37, 3.38, 3.41 and 3.42 correspond to the pion unitarity cut (a pion decaying into

another pion and a rho or sigma meson), while equations 3.39, 3.40, 3.43 and 3.44 correspond to the Landau cut. The unitarity cuts are heavily suppressed, because the rho and sigma meson masses are significantly larger than the pion mass. Furthermore, our goal is to dress the pion propagator with thermal interactions, however the unitarity cut corresponds to corrections to the vacuum pion propagator. Therefore, we drop all pion self-energy terms corresponding to the unitarity cut.

For positive energy, $\mathrm{Im}\Sigma^{\mathrm{L1}}_{\pi(\rho/\sigma)}$ provides resonant scattering with a thermal pion through a (ρ/σ) meson, while $\mathrm{Im}\Sigma^{\mathrm{L2}}_{\pi(\rho/\sigma)}$ provides scattering with a thermal (ρ/σ) meson. However, for negative energy $\mathrm{Im}\Sigma^{\mathrm{L2}}_{\pi(\rho/\sigma)}$ corresponds to $\pi\pi$-scattering, while $\mathrm{Im}\Sigma^{\mathrm{L2}}_{\pi(\rho/\sigma)}$ provides scattering with a thermal (ρ/σ) meson. In this work, we perform calculates in hadronic matter at temperatures between 100 and 180 MeV. Thermal rho and sigma excitations are heavily suppressed in this temperature range, due to their large masses relative to the temperature. Therefore, we drop terms corresponding to scattering with thermal rho or sigma mesons, and only calculate $\mathrm{Im}\Sigma^{\mathrm{L1}}_{\pi(\rho/\sigma)}$ for positive energy. In order to calculate the pion self-energy, for negative energy we note that the pion propagator is retarded, implying that:

$$\Sigma_\pi(-k_0,\vec{k}) = \Sigma^*_\pi(k_0,\vec{k}). \tag{3.45}$$

Therefore, one can infer the negative energy behavior from eq. 3.45.

The real part of Σ_π is calculated through the subtracted dispersion relation:

$$\mathrm{Re}\Sigma_\pi(k) = \frac{-1}{\pi}\int_{-\infty}^{\infty} dw \Big(\frac{\mathrm{Im}\Sigma_\pi(k_0,\vec{k})}{k_0 - w} - \frac{\mathrm{Im}\Sigma_\pi(0,\vec{k})}{-w}\Big). \tag{3.46}$$

The subtraction ensures that $\mathrm{Re}\Sigma_\pi$ is zero for zero energy. This is physically justified because the pion is a Goldstone boson, thus its self-energy is expected to be small for zero energy. Furthermore, if $\mathrm{Re}\Sigma_\pi$ is large at small energy (as is the case at high temperature and in the strong coupling limit) the pion propagator can develop a pole at zero energy. This behavior is expected for strong coupling, and corresponds to the development of a pion condensate. Although in principal the condensate can be removed by including repulsive $\pi\pi$-interactions, in this work any potential con-

densate is avoided due to the zero energy subtraction.

We graph the real and imaginary parts of the optical potential in figures 3.6 and 3.7. The optical potential is defined by:

$$U_\pi(\vec{k}) = \frac{\Sigma_\pi(\omega_k, \vec{k})}{2\,\omega_k}. \tag{3.47}$$

Although we dress the rho and sigma propagators in Σ_π with the vacuum rho and sigma self-energies, the pion propagator within Σ_π is not dressed. This propagator will not induce an infinite conductivity, because it corresponds to a thermal pion, while only intermediate particle states transmit charge through the medium.

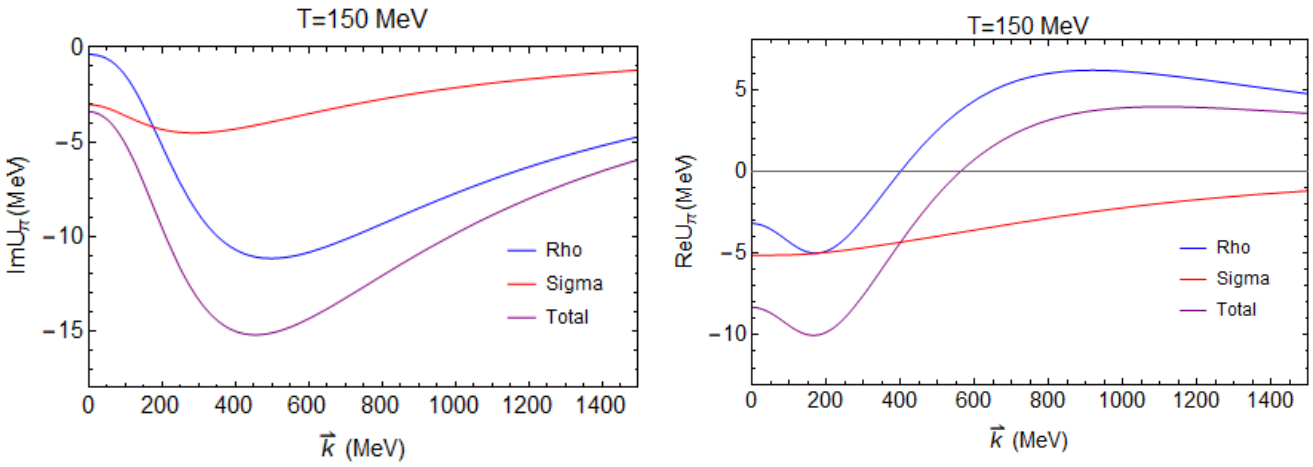

Figure 3.6: Left: Imaginary part of the optical potential, plotted as a function of momentum for $T = 150\,\text{MeV}$. Contributions from the rho (blue) and sigma (red) resonances are shown in addition to the total (purple). Right: Real part of the optical potential, plotted as a function of momentum for $T = 150\,\text{MeV}$. Contributions from the rho (blue) and sigma (red) resonances are shown in addition to the total (purple).

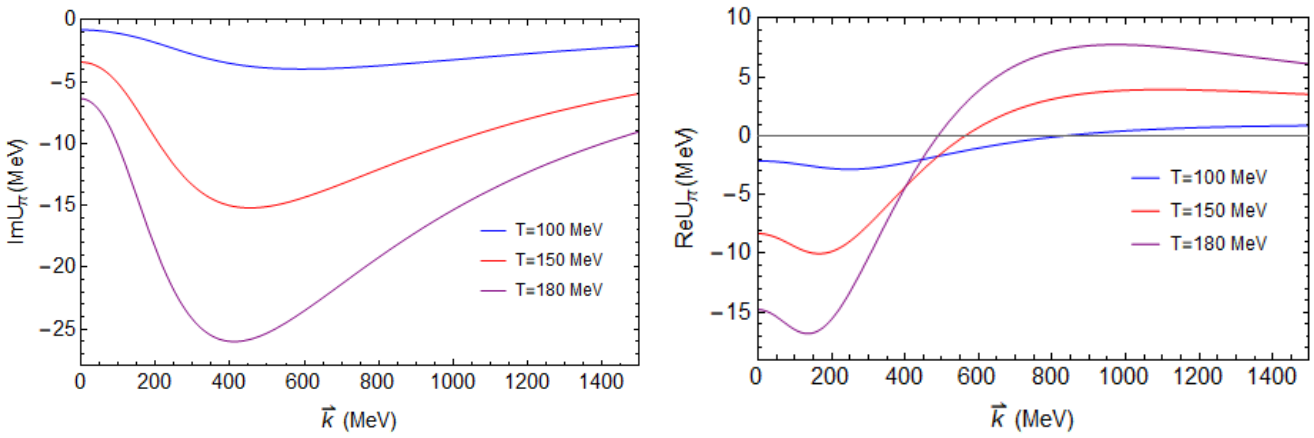

Figure 3.7: Left: Imaginary part of the optical potential, plotted as a function of momentum for $T = 100\,\text{MeV}$ (blue), $T = 150\,\text{MeV}$ (red), and $T = 180\,\text{MeV}$ (purple). Right: Real part of the optical potential, plotted as a function of momentum for $T = 100\,\text{MeV}$ (blue), $T = 150\,\text{MeV}$ (red), and $T = 180\,\text{MeV}$ (purple).

Our results for the optical potential agree well with those in refs. [50, 51]. However, the imaginary part of our total pion self-energy is a few MeV smaller than that obtained in ref. [51], because more resonances where considered in ref. [51]. We do not consider additional resonances here, because the rho and sigma provide the dominant contribution for low momentum, and the inclusion of further resonances would require the calculation of additional vertex corrections. Our pion self-energy is similar in form to those used in ref. [23] and [30]. However, ref. [23] calculates the self-energy in terms of the $\pi\pi$ cross section, making use of the cross section shown in 3.5. Reference [30] also expresses the self-energy in terms of the rho and sigma propagators, however ref. [30] does not dress the rho or sigma propagators with widths. Furthermore, ref. [30]'s self-energy due to the sigma resonance uses a factor of m_σ^2 in the numerator rather than $s - m_\pi^2$.

4. GAUGE INVARIANCE IN MEDIUM

In this chapter, we address how the Ward-Takahashi identities are maintained in medium. To begin, we examine the violation of the Ward identities due to dressing D_π in section 4.1, and generate the subsequent vertex corrections in section 4.2. In section 4.3 we demonstrate analytically that the Ward identities are maintained when the vertex corrections are included. We discuss the addition of form factors to the vertex corrections in section 4.4, including their effects of the Ward identities. Next, in section 4.5, we discuss the need to dress the intermediate particles within the vertex corrections and Σ_π with widths, and its effect on the Ward identities. Sections 4.6 addresses double counting that is encountered, and demonstrates how it can be removed without violating gauge invariance. Finally, in section 4.7 we take the transverse projection of the rho self-energy for vertices dressed with vertex correction.

4.1 Ward-Takahashi identities in medium

The Ward-Takahashi identities are straightforwardly satisfied in vacuum, but are upset by the addition of a pion self-energy in D_π. If one considers the Ward-Takahashi identity from eq 2.13 at zero momentum one obtains:

$$q_0 \Gamma^{(3)}_{0\,ab3} \;=\; g_\rho \epsilon_{3ab}(2k_0 q_0 + q_0^2 - \Sigma_\pi(k+q) + \Sigma_\pi(k)). \tag{4.1}$$

In general, eq. 4.1 will not be satisfied by the vacuum $\rho\pi\pi$ vertex. In figures 4.1, 4.2, and 4.3 we plot the right hand side of eq. 4.1 at T=0 and at T=150 MeV (dropping the factors of ϵ_{3ab}). The difference in the two results provides a measure of the violation of the Ward identities induced by dressing the pion propagators, without modifying the $\rho\pi\pi$ vertex.

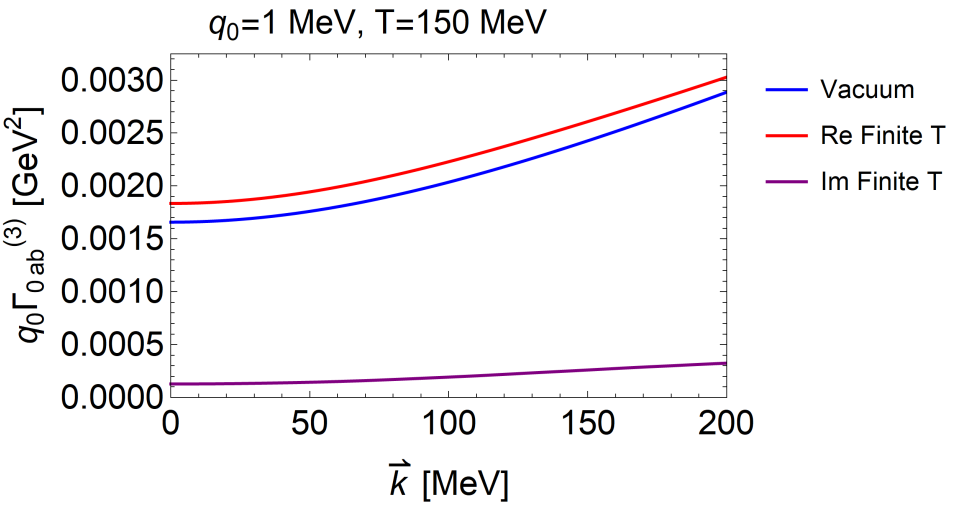

Figure 4.1: Comparison of q_0 times the temporal component of the vacuum $\rho\pi\pi$ vertex, to the result expected from the Ward-Takahashi identity, for $q_0 = 1\,\text{MeV}$ and $\vec{q} = 0$. Results are plotted for on-shell pion energy as a function of pion momentum. Although the vacuum vertex is purely real (blue line), the expected result from the Ward identity is complex. We plot the real part of the Ward result in red and the imaginary part in purple.

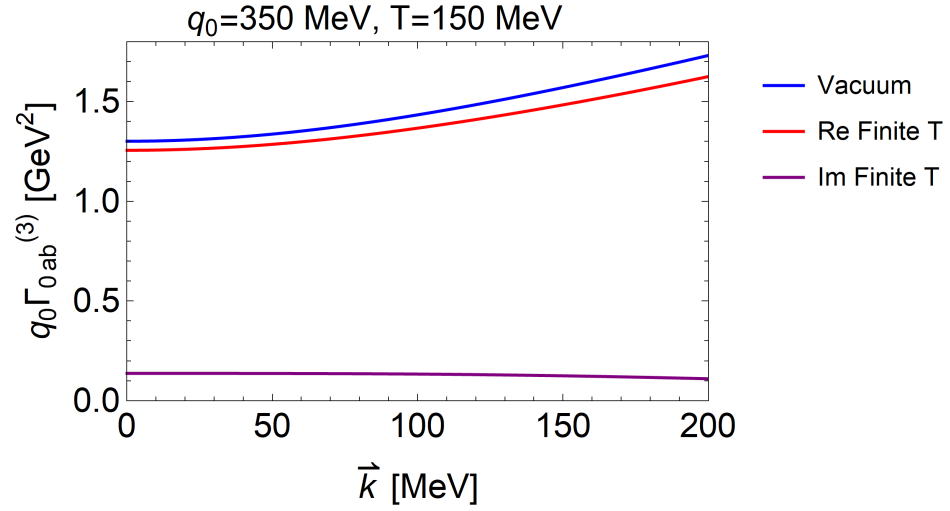

Figure 4.2: Comparison of q_0 times the temporal component of the vacuum $\rho\pi\pi$ vertex, to the result expected from the Ward-Takahashi identity, for $q_0 = 350\,\text{MeV}$ and $\vec{q} = 0$. Results are plotted for on-shell pion energy as a function of pion momentum. Although the vacuum vertex is purely real (blue line), the expected result from the Ward identity is complex. We plot the real part of the Ward result in red and the imaginary part in purple.

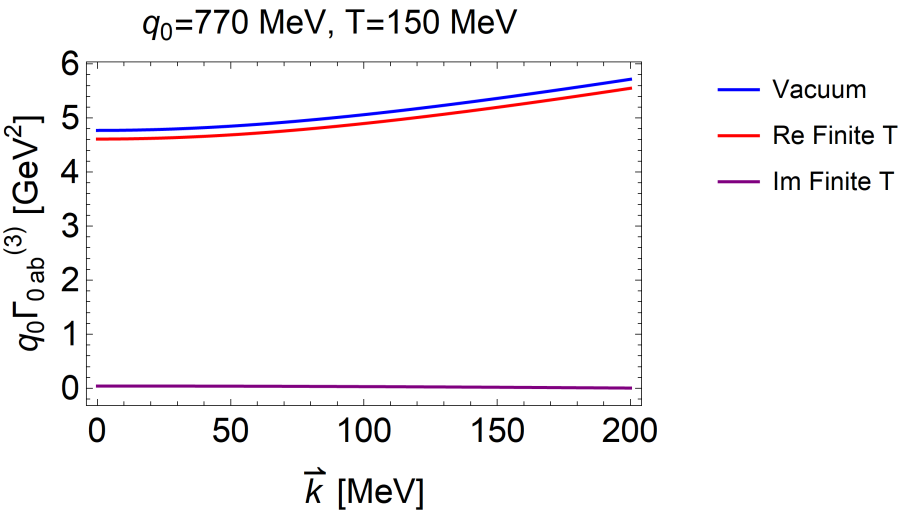

Figure 4.3: Comparison of q_0 times the tempral component of the vacuum $\rho\pi\pi$ vertex, to the result expected from the Ward-Takahashi identity, for $q_0 = 770\,\text{MeV}$ and $\vec{q} = 0$. Results are plotted for on-shell pion energy as a function of pion momentum. Although the vacuum vertex is purely real (blue line), the expected result from the Ward identity is complex. We plot the real part of the Ward result in red and the imaginary part in purple.

The percent difference between the vacuum vertex and the expected correction is largest for small energies, where it is $\approx 10\%$. As energy increases, the vacuum vertex increases quadratically, while the expected correction approaches zero, due to our pion self-energy approaching zero for large energy. Although the correction to the real part of the vertex appears small, the Ward identity implies that the corrected $\rho\pi\pi$ will be complex, while the vacuum vertex is purely real. This implies that the vertex corrections will create new cuts of the rho self-energy. Therefore, we set out to calculate the complex vertex corrections, necessary to maintain the Ward identities.

4.2 Vertex corrections

It is difficult to predict the effect of this violation of gauge invariance on the conductivity, because the Ward identities only directly restrict the temporal components of the vertices for $\vec{q} = 0$, while the conductivity is determined only by the spatial components of the rho self-energy. However, the violation can be remedied by considering thermal corrections to the $\rho\pi\pi$ and $\rho\rho\pi\pi$ vertices [44, 46]. The corrections to the $\rho\pi\pi$ vertex sufficient to maintain the Ward identities are

generated by coupling a rho meson to Σ_π in all possible configurations. Similarly, one can couple two rho mesons to Σ_π in all possible configurations to obtain corrections to the $\rho\rho\pi\pi$ vertex sufficient to maintain the Ward identities [46]. We then analytically determine which corrections are necessary to maintain the Ward identities when D_π is dressed with only the Landau cut of the pion self-energy. These vertex corrections completely fix both the temporal and spatial components of our vertices for all q, and assure that gauge invariance is not violated. Thus, the Ward identities will fix the spacial components of the vertex corrections, and provide a correction to the conductivity.

We follow the lead of references [40, 44] to calculate the required corrections. If one subtracts the vacuum vertex from both sides of equations 2.13 and 2.14 one obtains:

$$q^\mu \Gamma'^{(3)}_{\mu\, ab3} = g_\rho \epsilon_{3ab}(-\Sigma_\pi(k+q) + \Sigma_\pi(k)), \tag{4.2}$$

$$q^\mu \Gamma'^{(4)}_{\mu\nu\, ab33} = i g_\rho(\epsilon_{3ca}\Gamma'^{(3)}_{\nu\, bc3}(k,-q) - \epsilon_{3bc}\Gamma'^{(3)}_{\nu\, ca3}(k+q,-q)), \tag{4.3}$$

where $\Gamma'^{(3)}_{\mu\, ab3}$ and $\Gamma'^{(4)}_{\mu\nu\, ab3}$ are the vertex corrections to the $\rho\pi\pi$ and $\rho\rho\pi\pi$ vertices, respectively. The total vertices are then given by:

$$\Gamma^{(3)}_{\mu\, ab3} = g_\rho \epsilon_{3ab}(2k+q)_\mu + \Gamma'^{(3)}_{\mu\, ab3} \tag{4.4}$$

$$\Gamma^{(4)}_{\mu\nu\, ab33} = 2 i g_\rho^2(\delta_{ab} - \delta_{3a}\delta_{3b}) g_{\mu\nu} + \Gamma'^{(4)}_{\mu\nu\, ab33}. \tag{4.5}$$

The three-point vertex corrections to the $\rho\pi\pi$ vertex can be derived by coupling a single rho meson to the thermal Σ_π loop in all possible ways, while the four-point vertex corrections to the $\rho\rho\pi\pi$ vertex are derived by coupling two rho mesons to the thermal Σ_π loop. Figures 4.4, 4.5, and 4.6 show the vertex corrections resulting from dressing D_π with $\Sigma_{\pi\rho}$ and $\Sigma_{\pi\sigma}$.

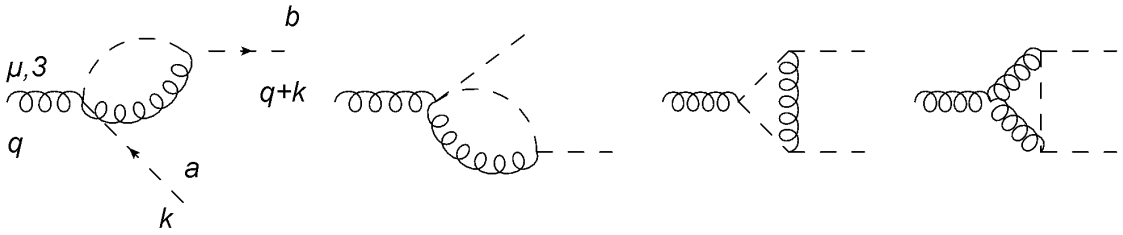

Figure 4.4: Corrections to the $\rho\pi\pi$ vertex due to $\Sigma_{\pi(\rho)}$.

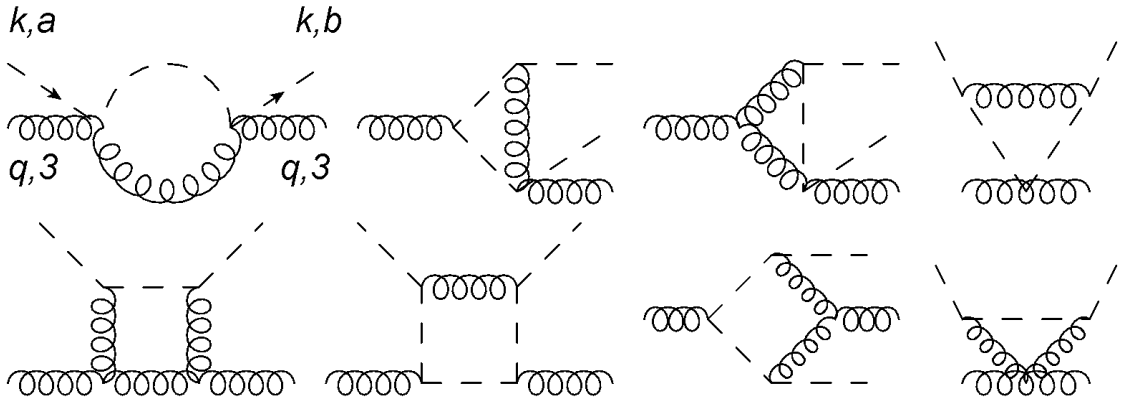

Figure 4.5: Corrections to the $\rho\rho\pi\pi$ vertex due to $\Sigma_{\pi(\rho)}$.

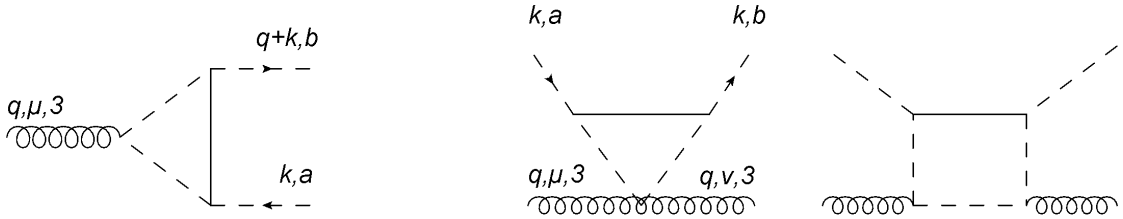

Figure 4.6: Left: Correction to the $\rho\pi\pi$ vertex due to $\Sigma_{\pi(\sigma)}$. Right: Corrections to the $\rho\rho\pi\pi$ vertex due to $\Sigma_{\pi(\sigma)}$.

We write the minimum diagrams necessary to maintain gauge invariance. Consequently, there are fewer corrections due to the sigma resonance, because the sigma meson is neutral and the $\sigma\pi\pi$

vertex is a Lorentz scalar.

Calculation of the vertex corrections requires the $\rho\rho\rho$, $\rho\rho\rho\rho$, and $\sigma\pi\pi$ vertices. We derive the $\rho\rho\rho$ and $\rho\rho\rho\rho$ vertices from the interaction Lagrangians:

$$\mathcal{L}_{\rho\rho\rho} = \frac{-1}{2} g_\rho \rho_{\mu\nu} \cdot (\rho_\mu \times \rho_\nu), \tag{4.6}$$

$$\mathcal{L}_{\rho\rho\rho\rho} = \frac{g_\rho^2}{4} (\rho_\mu \cdot \rho_\nu \cdot \rho_\lambda \rho_\gamma - \rho_\mu \cdot \rho_\lambda \cdot \rho_\nu \rho_\gamma). \tag{4.7}$$

The resulting vertices are given by:

$$\Gamma^{(3)}_{\mu\nu\lambda\, abc} = g_\rho \epsilon_{abc} ((p-q)_\nu g_{\lambda\mu} + (2q+p)_\lambda g_{\mu\nu} - (2p+q)_\mu g_{\nu\lambda}), \tag{4.8}$$

$$\begin{aligned} \Gamma^{(4)}_{\mu\nu\lambda\gamma\, abcd} = {} & i g_\rho^2 ((\delta_{ab}\delta_{cd} + \delta_{bc}\delta_{ad} - 2\delta_{ac}\delta_{bd}) g_{\mu\lambda} g_{\nu\gamma} \\ & + (\delta_{ab}\delta_{cd} + \delta_{bd}\delta_{ac} - 2\delta_{bc}\delta_{ad}) g_{\mu\gamma} g_{\nu\lambda} \\ & + (\delta_{ac}\delta_{bd} + \delta_{cb}\delta_{ad} - 2\delta_{cd}\delta_{ab}) g_{\mu\nu} g_{\gamma\lambda}). \end{aligned} \tag{4.9}$$

Figure 4.7 expresses these vertices diagrammatically.

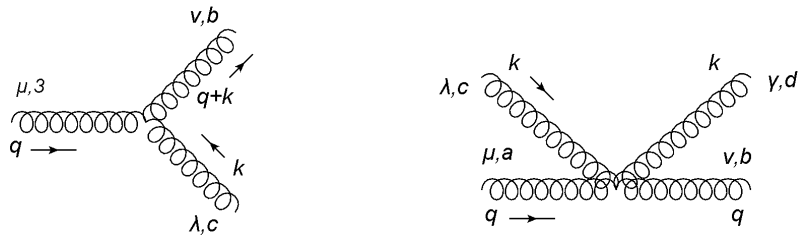

Figure 4.7: Left: diagrammatic representation of the $\rho\rho\rho$ vertex. Right: diagrammatic representation of the $\rho\rho\rho\rho$ vertex.

$\Sigma_{\pi(\sigma)}$ was calculated from the Born amplitude, so we have not established a $\sigma\pi\pi$ vertex. In

order to calculate the sigma vertex corrections we define the effective $\sigma\pi\pi$ vertex:

$$\Gamma^{(3)}_{\sigma\, ab} = i\delta_{ab} g_\sigma \sqrt{s - m_\pi^2}. \tag{4.10}$$

If one uses Feynman rules along with $\Gamma^{(3)}_{\sigma\, ab}$ to calculate Σ_σ and $\Sigma_{\pi(\sigma)}$ one obtains the same results as eqs. 3.20 and 3.23. $\Gamma^{(3)}_{\sigma\, ab}$ can then be used to calculate vertex corrections involving the $\sigma\pi\pi$ vertex, so that the Ward identities will be satisfied.

We are now in place to calculate the vertex corrections resulting from the inclusion of Σ_π. The corrections to the $\rho\pi\pi$ vertex due to the ρ resonance are given by:

$$\Gamma^{(3)A\rho}_{\mu\, ab3}(k,q) = \epsilon_{3ab}\frac{3g_\rho^3}{2}T\sum_{n(even)}\left[\int \frac{d^3p}{(2\pi)^3} D_\pi(p) D_\rho^{\nu\lambda}(k+p) g_{\mu\lambda}(k-p)_\nu\right]_{p_0=iw_n}, \tag{4.11}$$

$$\Gamma^{(3)B\rho}_{\mu\, ab3}(k,q) = \epsilon_{3ab}\frac{3g_\rho^3}{2}T\sum_{n(even)}\left[\int \frac{d^3p}{(2\pi)^3} D_\pi(p) D_\rho^{\nu\lambda}(q+k+p) g_{\mu\lambda}(q+k-p)_\nu\right]_{p_0=iw_n} \tag{4,12}$$

$$\begin{aligned}\Gamma^{(3)C\rho}_{\mu\, ab3}(k,q) = \epsilon_{3ab}\frac{g_\rho^3}{2}T\sum_{n(even)}\Bigg[\int \frac{d^3p}{(2\pi)^3} & D_\pi(p) D_\pi(q+p) D_\rho^{\nu\lambda}(q+k+p) \\ & (2p+q)_\mu(-p+k+q)_\lambda(k-p-q)_\nu\Bigg]_{p_0=iw_n},\end{aligned} \tag{4.13}$$

$$\begin{aligned}\Gamma^{(3)D\rho}_{\mu\, ab3}(k,q) = \epsilon_{3ab}\frac{g_\rho^3}{2}T\sum_{n(even)}\Bigg[\int \frac{d^3p}{(2\pi)^3} & D_\pi(p) D_\rho^{\beta\lambda}(k+p) D_\rho^{\nu\alpha}(q+k+p) \\ & (-p+k+q)_\alpha(k-p)_\beta((q-p-k)_\nu g_{\mu\lambda} - (2q+p+k)_\lambda g_{\mu\nu} \\ & +(2p+2k+q)_\mu g_{\nu\lambda})\Bigg]_{p_0=iw_n}.\end{aligned} \tag{4.14}$$

The vertex corrections induced by the σ resonance are given by:

$$\begin{aligned}\Gamma^{(3)C\sigma}_{\mu\, ab3}(k,q) = \epsilon_{3ab}\frac{g_\rho g_\sigma^2}{2}T\sum_{n(even)}\Bigg[\int \frac{d^3p}{(2\pi)^3} & D_\pi(p) D_\pi(q+p) D_\sigma(q+k+p) \\ & ((q+k+p)^2 - m_\pi^2)(2p+q)_\mu\Bigg]_{p_0=iw_n}.\end{aligned} \tag{4.15}$$

The corrections to the $\rho\rho\pi\pi$ vertex from ρ resonant scattering are give by:

$$\Gamma^{(4)A\rho}_{\mu\nu\,ab33}(k,q) = (-3\delta_{3a}\delta_{3b}+5\delta_{ab})\frac{ig_\rho^4}{2}T\sum_{n(even)}\Big[\int\frac{d^3p}{(2\pi)^3}D_\pi(p)D_{\rho\,\mu\nu}(q+k+p)\Big]_{p_0=iw_n} + (k\to -k), \tag{4.16}$$

$$\Gamma^{(4)B_1\rho}_{\mu\nu\,ab33}(k,q) = -2\delta_{ab}\frac{ig_\rho^4}{2}T\sum_{n(even)}\Big[\int\frac{d^3p}{(2\pi)^3}D_\pi(p)D_\pi(p+q)D_{\rho\,\nu\beta}(k+p) (2p+q)_\mu(p-k)^\beta\Big]_{p_0=iw_n} + (k\to -k), \tag{4.17}$$

$$\Gamma^{(4)B_2\rho}_{\mu\nu\,ab33}(k,q) = \Gamma^{(4)B_1\rho}_{\nu\mu ab}(k,q), \tag{4.18}$$

$$\Gamma^{(4)C_1\rho}_{\mu\nu\,ab33}(k,q) = -(\delta_{ab}-3\delta_{3a}\delta_{3b})\frac{ig_\rho^4}{2}T\sum_{n(even)}\Big[\int\frac{d^3p}{(2\pi)^3}D_\pi(p)D_\rho^{\lambda\beta}(k+p)D_\rho^{\gamma\alpha}(q+k+p) (p-k)_\beta g_{\alpha\nu}\big(-(2q+k+p)_\lambda g_{\mu\gamma}-(-q+p+k)_\gamma g_{\mu\lambda} +(q+2k+2p)_\mu g_{\gamma\lambda}\big)\Big]_{p_0=iw_n} + (k\to -k), \tag{4.19}$$

$$\Gamma^{(4)C_2\rho}_{\mu\nu\,ab33}(k,q) = \Gamma^{(4)C_1\rho}_{\nu\mu ab}(k,q), \tag{4.20}$$

$$\Gamma^{(4)D\rho}_{\mu\nu\,ab33}(k,q) = (\delta_{ab}+\delta_{3a}\delta_{3b})\frac{ig_\rho^4}{2}T\sum_{n(even)}\Big[\int\frac{d^3p}{(2\pi)^3}D_\pi(p)D_\rho^{\phi\theta}(k+p) D_\rho^{\gamma\lambda}(k+p)D_\rho^{\alpha\beta}(q+k+p)(p-k)_\theta(p-k)_\lambda \big((q-p-k)_\alpha g_{\mu\gamma}-(2q+p+k)_\gamma g_{\mu\alpha}+(q+2k+2p)_\mu g_{\gamma\alpha}\big) \big((q-p-k)_\beta g_{\nu\phi}-(2q+p+k)_\phi g_{\nu\beta} +(q+2k+2p)_\nu g_{\beta\phi}\big)\Big]_{p_0=iw_n} + (k\to -k), \tag{4.21}$$

$$\Gamma^{(4)E\rho}_{\mu\nu\,ab33}(k,q) = (\delta_{ab}+\delta_{3a}\delta_{3b})\frac{ig_\rho^4}{2}T\sum_{n(even)}\Big[\int\frac{d^3p}{(2\pi)^3}D_\pi(p)^2D_\pi(p+q)D_{\rho\,\alpha\beta}(k+p) (2p+q)_\mu(p-k)^\alpha(p-k)^\beta(2p+q)_\nu\Big]_{p_0=iw_n} + (k\to -k), \tag{4.22}$$

$$\Gamma^{(4)F_1\rho}_{\mu\nu\,ab33}(k,q) = -2\delta_{3a}\delta_{3b}\frac{ig_\rho^4}{2}T\sum_{n(even)}\Bigg[\int\frac{d^3p}{(2\pi)^3}D_\pi(p)D_\pi(p+q)D_\rho^{\gamma\lambda}(k+p)$$
$$D_\rho^{\alpha\beta}(q+k+p)(q-k+p)_\beta(2p+q)_\nu(p-k)_\lambda$$
$$((q-k-p)_\alpha g_{\mu\gamma}-(2q+p+k)_\gamma g_{\mu\alpha}$$
$$+(q+2k+2p)_\mu g_{\gamma\alpha})\Bigg]_{p_0=iw_n}, \tag{4.23}$$

$$\Gamma^{(4)F_2\rho}_{\mu\nu\,ab33}(k,q) = \Gamma^{(4)F_1\rho}_{\nu\mu ab}(k,q), \tag{4.24}$$

$$\Gamma^{(4)G\rho}_{\mu\nu\,ab33}(k,q) = -2(\delta_{3a}\delta_{3b}+\delta_{ab})\frac{ig_\rho^4}{2}T\sum_{n(even)}\Bigg[\int\frac{d^3p}{(2\pi)^3}D_\pi(p)^2D_\rho^{\alpha\beta}(k+p)$$
$$(k-p)_\alpha(k-p)_\beta g_{\mu\nu}\Bigg]_{p_0=iw_n}, \tag{4.25}$$

$$\Gamma^{(4)H\rho}_{\mu\nu\,ab33}(k,q) = -2(\delta_{3a}\delta_{3b}+\delta_{ab})\frac{ig_\rho^4}{2}T\sum_{n(even)}\Bigg[\int\frac{d^3p}{(2\pi)^3}D_\pi(p)D_\rho^{\alpha\lambda}(k+p)D_\rho^{\beta\gamma}(k+p)$$
$$(k-p)_\alpha(k-p)_\beta(g_{\mu\lambda}g_{\nu\gamma}+g_{\mu\gamma}g_{\nu\lambda}-2g_{\mu\nu}g_{\lambda\gamma})\Bigg]_{p_0=iw_n}. \tag{4.26}$$

The corrections to the $\rho\rho\pi\pi$ vertex from σ resonant scattering are given by:

$$\Gamma^{(4)E\sigma}_{\mu\nu\,ab33}(k,q) = (\delta_{ab}-\delta_{3a}\delta_{3b})\frac{ig_\rho^2g_\sigma^2}{2}T\sum_{n(even)}\Bigg[\int\frac{d^3p}{(2\pi)^3}D_\pi(p)^2D_\pi(p+q)D_\sigma(k+p)$$
$$((k+p)^2-m_\pi^2)(2p+q)_\mu(2p+q)_\nu\Bigg]_{p_0=iw_n}$$
$$+(k\to -k), \tag{4.27}$$

$$\Gamma^{(4)G\sigma}_{\mu\nu\,ab33}(k,q) = -2(\delta_{ab}-\delta_{3a}\delta_{3b})\frac{ig_\rho^2g_\sigma^2}{2}T\sum_{n(even)}\Bigg[\int\frac{d^3p}{(2\pi)^3}D_\pi(p)^2D_\sigma(k+p)$$
$$((k+p)^2-m_\pi^2)g_{\mu\nu}\Bigg]_{p_0=iw_n}. \tag{4.28}$$

One must calculate all diagrams resulting from replacing a vacuum vertex with a corresponding vertex correction. For the four-point vertex corrections, we also include diagrams resulting from interchanging rho or pion propagators when they produce unique vertex corrections. These terms are represented above by the $k\to -k$ and $\mu\nu\leftrightarrow\nu\mu$ terms. Each term also includes a systemati-

zation factor of $\frac{1}{2}$, as was the case for the pion and rho self-energies. Finally, we have not included a form factor in the above equations, because the addition of the form factors will be discussed in section 4.4. Furthermore, for our final calculation we drop all vertex corrections containing multiple rho propagators, because they are suppressed by powers of $\frac{1}{m_\rho^2}$. However, these diagrams will be included when demonstrating analytically how the Ward identities are maintained. Finally, we perform the summation for the vertex corrections after simplifying the expression using a spectral representation. The results are shown in the appendix.

4.3 Satisfying the Ward identities

Here we show analytically that the vertex corrections satisfy eqs. 4.2 and 4.3. In this section we use sharp propagators within Σ_π and the vertex correction. The complications that arise from adding particle widths and form factors will be addressed in 4.4 and 4.5 respectively. To begin, we make note that with some algebra one can show:

$$q^\mu(2p+q)_\mu = ((q+p)^2 - m_\pi^2) - (p^2 - m_\pi^2), \tag{4.29}$$

and

$$\begin{aligned}
&q^\mu((p-q)_\nu g_{\lambda\mu} + (2q+p)_\lambda g_{\mu\nu} - (2p+q)_\mu g_{\nu\lambda}) \\
&\Big(- g^{\alpha\nu} + \frac{(q+p)^\alpha (q+p)^\nu}{m_\rho^2}\Big)\Big(- g^{\beta\lambda} + \frac{p^\beta p^\lambda}{m_\rho^2}\Big) = \\
&\big((q+p)^2 - m_\rho^2\big)\Big(- g^{\alpha\beta} + \frac{p^\alpha p^\beta}{m_\rho^2}\Big) \\
&-\big(p^2 - m_\rho^2\big)\Big(- g^{\alpha\beta} + \frac{(q+p)^\alpha (q+p)^\beta}{m_\rho^2}\Big).
\end{aligned} \tag{4.30}$$

We now show that eq. 4.2 is satisfied by the corrections to the $\rho\pi\pi$ vertex ($\Gamma^{(3)A\rho}_{\mu\,ab3}$, $\Gamma^{(3)B\rho}_{\mu\,ab3}$, $\Gamma^{(3)C\rho}_{\mu\,ab3}$, $\Gamma^{(3)D\rho}_{\mu\,ab3}$, and $\Gamma^{(3)C\sigma}_{\mu\,ab3}$). One can use eqs. 4.29 and 4.30 to show that:

$$
\begin{aligned}
q^\mu\Gamma^{(3)C\rho}_{\mu\,ab3}(k,q) &= \epsilon_{3ab}\frac{g_\rho^3}{2}T\sum_{n(even)}\left[\int\frac{d^3p}{(2\pi)^3}D_\pi(p)D_\rho^{\nu\lambda}(q+k+p)(q+k-p)_\lambda(-q+k-p)_\nu\right]_{p_0=iw_n}\\
&\quad -\epsilon_{3ab}\frac{g_\rho^3}{2}T\sum_{n(even)}\left[\int\frac{d^3p}{(2\pi)^3}D_\pi(q+p)D_\rho^{\nu\lambda}(q+k+p)(q+k-p)_\lambda(-q+k-p)_\nu\right]_{p_0=iw_n}\\
&= \frac{g_\rho\epsilon_{3ab}}{2}\big(\Sigma_{\pi(\rho)}(q+k)-\Sigma_{\pi(\rho)}(k)\big)\\
&\quad +\epsilon_{3ab}\frac{g_\rho^3}{2}T\sum_{n(even)}\left[\int\frac{d^3p}{(2\pi)^3}D_\pi(p)D_\rho^{\nu\lambda}(q+k+p)(-2q)_\lambda(q+k-p)_\nu\right]_{p_0=iw_n}\\
&\quad -\epsilon_{3ab}\frac{g_\rho^3}{2}T\sum_{n(even)}\left[\int\frac{d^3p}{(2\pi)^3}D_\pi(p)D_\rho^{\nu\lambda}(k+p)(2q)_\lambda(k-p)_\nu\right]_{p_0=iw_n}, \qquad (4.31)\\
q^\mu\Gamma^{(3)D\rho}_{\mu\,ab3}(k,q) &= -\epsilon_{3ab}\frac{g_\rho^3}{2}T\sum_{n(even)}\left[\int\frac{d^3p}{(2\pi)^3}D_\pi(p)D_\rho^{\nu\lambda}(k+p)(q+k-p)_\nu(k-p)_\lambda\right]_{p_0=iw_n}\\
&\quad +\epsilon_{3ab}\frac{g_\rho^3}{2}T\sum_{n(even)}\left[\int\frac{d^3p}{(2\pi)^3}D_\pi(p)D_\rho^{\nu\lambda}(q+k+p)(q+k-p)_\nu(k-p)_\lambda\right]_{p_0=iw_n}\\
&= \frac{g_\rho\epsilon_{3ab}}{2}\big(\Sigma_{\pi(\rho)}(q+k)-\Sigma_{\pi(\rho)}(k)\big)\\
&\quad +\epsilon_{3ab}\frac{g_\rho^3}{2}T\sum_{n(even)}\left[\int\frac{d^3p}{(2\pi)^3}D_\pi(p)D_\rho^{\nu\lambda}(q+k+p)(-q)_\nu(q+k-p)_\lambda\right]_{p_0=iw_n}\\
&\quad -\epsilon_{3ab}\frac{g_\rho^3}{2}T\sum_{n(even)}\left[\int\frac{d^3p}{(2\pi)^3}D_\pi(p)D_\rho^{\nu\lambda}(k+p)(q)_\nu(k-p)_\lambda\right]_{p_0=iw_n} \qquad (4.32)\\
q^\mu\Gamma^{(3)C\sigma}_{\mu\,ab3}(k,q) &= \epsilon_{3ab}\frac{g_\rho g_\sigma^2}{2}T\sum_{n(even)}\left[\int\frac{d^3p}{(2\pi)^3}D_\pi(p)D_\sigma(q+k+p)((q+k+p)^2-m_\pi^2)\right]_{p_0=iw_n}\\
&\quad -\epsilon_{3ab}\frac{g_\rho g_\sigma^2}{2}T\sum_{n(even)}\left[\int\frac{d^3p}{(2\pi)^3}D_\pi(q+p)D_\sigma(q+k+p)((q+k+p)^2-m_\pi^2)\right]_{p_0=iw_n}\\
&= g_\rho\epsilon_{3ab}\big(\Sigma_{\pi(\sigma)}(q+k)-\Sigma_{\pi(\sigma)}(k)\big). \qquad (4.33)
\end{aligned}
$$

It is straight forward to use the above equations to show:

$$
\begin{aligned}
&q^{\mu}\Gamma^{(3)C\rho}_{\mu\,ab3}(k,q)+q^{\mu}\Gamma^{(3)D\rho}_{\mu\,ab3}(k,q)+q^{\mu}\Gamma^{(3)C\sigma}_{\mu\,ab3}(k,q)= \\
&g_{\rho}\epsilon_{3ab}\big(\Sigma_{\pi}(q+k)-\Sigma_{\pi}(k)\big) \\
&-\epsilon_{3ab}\frac{3g_{\rho}^{3}}{2}T\sum_{n(even)}\left[\int\frac{d^{3}p}{(2\pi)^{3}}D_{\pi}(p)D_{\rho}^{\nu\lambda}(q+k+p)q_{\lambda}(q+k-p)_{\nu}\right]_{p_0=iw_n} \\
&-\epsilon_{3ab}\frac{3g_{\rho}^{3}}{2}T\sum_{n(even)}\left[\int\frac{d^{3}p}{(2\pi)^{3}}D_{\pi}(p)D_{\rho}^{\nu\lambda}(k+p)q_{\lambda}(k-p)_{\nu}\right]_{p_0=iw_n}. \qquad (4.34)
\end{aligned}
$$

The last two terms in the eq. 4.34 are exactly canceled by $q^{\mu}\Gamma^{(3)A\rho}_{\mu\,ab3}$ and $q^{\mu}\Gamma^{(3)B\rho}_{\mu\,ab3}$, thus we find:

$$
\begin{aligned}
&q^{\mu}\Gamma^{(3)A\rho}_{\mu\,ab3}(k,q)+q^{\mu}\Gamma^{(3)B\rho}_{\mu\,ab3}(k,q)+q^{\mu}\Gamma^{(3)C\rho}_{\mu\,ab3}(k,q)+q^{\mu}\Gamma^{(3)D\rho}_{\mu\,ab3}(k,q)+q^{\mu}\Gamma^{(3)C\sigma}_{\mu\,ab3}(k,q) \\
&=g_{\rho}\epsilon_{3ab}\big(\Sigma_{\pi}(q+k)-\Sigma_{\pi}(k)\big), \qquad (4.35)
\end{aligned}
$$

and eq. 4.2 is satisfied. Next we show that eq. 4.3 is satisfied. To begin, we break the corrections to the $\rho\rho\pi\pi$ vertex into the following four subgroups:

$$
\begin{aligned}
\Gamma^{(4)X1}_{\mu\nu\,ab}(k,q) &= \Gamma^{(4)A\rho}_{\mu\nu\,ab33}(k,q)+\Gamma^{(4)B_1\rho}_{\mu\nu\,ab33}(k,q)+\Gamma^{(4)C_1\rho}_{\mu\nu\,ab33}(k,q), \\
\Gamma^{(4)X2}_{\mu\nu\,ab}(k,q) &= \Gamma^{(4)B_1\rho}_{\nu\mu\,ab33}(k,q)+\Gamma^{(4)E\rho}_{\mu\nu\,ab33}(k,q)+\Gamma^{(4)F_1\rho}_{\mu\nu\,ab33}(k,q)+\Gamma^{(4)G\rho}_{\mu\nu\,ab33}(k,q), \\
\Gamma^{(4)X3}_{\mu\nu\,ab}(k,q) &= \Gamma^{(4)C_1\rho}_{\nu\mu\,ab33}(k,q)+\Gamma^{(4)D\rho}_{\mu\nu\,ab33}(k,q)+\Gamma^{(4)F_1\rho}_{\nu\mu\,ab33}(k,q)+\Gamma^{(4)H\rho}_{\mu\nu\,ab33}(k,q), \\
\Gamma^{(4)X4}_{\mu\nu\,ab}(k,q) &= \Gamma^{(4)E\sigma}_{\mu\nu\,ab33}(k,q)+\Gamma^{(4)G\sigma}_{\mu\nu\,ab33}(k,q). \qquad (4.36)
\end{aligned}
$$

It is straight forward to show that eq. 4.3 will be satisfied if the subgroups fulfill:

$$
\begin{aligned}
q^\mu \Gamma^{(4)X1}_{\mu\nu\,ab}(k,q) &= ig_\rho\big(\epsilon_{3ca}(\Gamma^{(3)A\rho}_{\nu\,bc3}(k,-q)+\Gamma^{(3)B\rho}_{\nu\,bc3}(k,-q)) \qquad (4.37)\\
&\quad -\epsilon_{3bc}(\Gamma^{(3)A\rho}_{\nu\,ca3}(k+q,-q)+\Gamma^{(3)B\rho}_{\nu\,ca3}(k+q,-q))\big),\\
q^\mu \Gamma^{(4)X2}_{\mu\nu\,ab}(k,q) &= ig_\rho\big(\epsilon_{3ca}\Gamma^{(3)C\rho}_{\nu\,bc3}(k,-q)-\epsilon_{3bc}\Gamma^{(3)C\rho}_{\nu\,ca3}(k+q,-q)\big), \qquad (4.38)\\
q^\mu \Gamma^{(4)X3}_{\mu\nu\,ab}(k,q) &= ig_\rho\big(\epsilon_{3ca}\Gamma^{(3)D\rho}_{\nu\,bc3}(k,-q)-\epsilon_{3bc}\Gamma^{(3)D\rho}_{\nu\,ca3}(k+q,-q)\big), \qquad (4.39)\\
q^\mu \Gamma^{(4)X4}_{\mu\nu\,ab}(k,q) &= ig_\rho\big(\epsilon_{3ca}\Gamma^{(3)C\sigma}_{\nu\,bc3}(k,-q)-\epsilon_{3bc}\Gamma^{(3)C\sigma}_{\nu\,ca3}(k+q,-q)\big). \qquad (4.40)
\end{aligned}
$$

Thus, we must show that eqs. 4.37 through 4.40 are satisfied. We start by calculating $q^\mu \Gamma^{(4)X1}_{\mu\nu\,ab}$. One can use eqs. 4.29 and 4.30 to show:

$$
\begin{aligned}
q^\mu \Gamma^{(4)X1}_{\mu\nu\,ab}(k,q) &= (-3\delta_{3a}\delta_{3b}+5\delta_{ab})\frac{ig_\rho^4}{2}T\sum_{n(even)}\left[\int\frac{d^3p}{(2\pi)^3}D_\pi(p)D_{\rho\,\mu\nu}(q+k+p)(q^\mu)\right]_{p_0=iw_n}\\
&\quad -2\delta_{ab}\frac{ig_\rho^4}{2}T\sum_{n(even)}\left[\int\frac{d^3p}{(2\pi)^3}D_\pi(p)D_{\rho\,\mu\nu}(k+p)(p-k)^\mu\right]_{p_0=iw_n}\\
&\quad +2\delta_{ab}\frac{ig_\rho^4}{2}T\sum_{n(even)}\left[\int\frac{d^3p}{(2\pi)^3}D_\pi(p+q)D_{\rho\,\mu\nu}(k+p)(p-k)^\mu\right]_{p_0=iw_n}\\
&\quad +(\delta_{ab}-3\delta_{3a}\delta_{3b})\frac{ig_\rho^4}{2}T\sum_{n(even)}\left[\int\frac{d^3p}{(2\pi)^3}D_\pi(p)D_{\rho\,\mu\nu}(k+p)(p-k)^\mu\right]_{p_0=iw_n}\\
&\quad -(\delta_{ab}-3\delta_{3a}\delta_{3b})\frac{ig_\rho^4}{2}T\sum_{n(even)}\left[\int\frac{d^3p}{(2\pi)^3}D_\pi(p)D_{\rho\,\mu\nu}(q+k+p)(p-k)^\mu\right]_{p_0=iw_n}\\
&\quad +(k\to -k). \qquad (4.41)
\end{aligned}
$$

After some algebra one can rewrite eq. 4.41 as:

$$
\begin{aligned}
q^\mu \Gamma^{(4)X1}_{\mu\nu\,ab}(k,q) &= -3(\delta_{ab}-\delta_{3a}\delta_{3b})\frac{ig_\rho^4}{2}T\sum_{n(even)}\left[\int\frac{d^3p}{(2\pi)^3}D_\pi(p)D_{\rho\,\mu\nu}(q+k+p)(q+k-p)^\mu\right]_{p_0=iw_n}\\
&\quad +3(\delta_{ab}-\delta_{3a}\delta_{3b})\frac{ig_\rho^4}{2}T\sum_{n(even)}\left[\int\frac{d^3p}{(2\pi)^3}D_\pi(p)D_{\rho\,\mu\nu}(q-k+p)(q-k-p)^\mu\right]_{p_0=iw_n}. \qquad (4.42)
\end{aligned}
$$

It is straight forward to show that the above expression is equivalent to the right hand side of eq. 4.37, by inserting $\Gamma^{(3)A\rho}_{\mu\, ab3}$ and $\Gamma^{(3)B\rho}_{\mu\, ab3}$ into eq. 4.37 and evaluating the resulting isospin contractions.

Next we will evaluate $q^\mu \Gamma^{(4)X2}_{\mu\nu\, ab}$. One can use eq. 4.29 and 4.30 to show:

$$
\begin{aligned}
q^\mu \Gamma^{(4)X2}_{\mu\nu\, ab}(k,q) \;=\; & \Big\{ -2\delta_{ab}\frac{ig_\rho^4}{2}T\sum_{n(even)}\Big[\int \frac{d^3p}{(2\pi)^3} D_\pi(p) D_\pi(p+q) D_{\rho\,\mu\lambda}(k+p) \\
& (2p+q)_\nu (q^\mu)(p-k)^\lambda\Big]_{p_0=iw_n} \\
& +(\delta_{ab}+\delta_{3a}\delta_{3b})\frac{ig_\rho^4}{2}T\sum_{n(even)}\Big[\int \frac{d^3p}{(2\pi)^3} D_\pi(p)^2 D_{\rho\,\mu\lambda}(k+p) \\
& (2p+q)_\nu (p-k)^\mu (p-k)^\lambda\Big]_{p_0=iw_n} \\
& -(\delta_{ab}+\delta_{3a}\delta_{3b})\frac{ig_\rho^4}{2}T\sum_{n(even)}\Big[\int \frac{d^3p}{(2\pi)^3} D_\pi(p) D_\pi(p+q) D_{\rho\,\mu\lambda}(k+p) \\
& (2p+q)_\nu (p-k)^\mu (p-k)^\lambda\Big]_{p_0=iw_n} + (k\to -k)\Big\} \\
& +2\delta_{3a}\delta_{3b}\frac{ig_\rho^4}{2}T\sum_{n(even)}\Big[\int \frac{d^3p}{(2\pi)^3} D_\pi(p) D_\pi(p+q) D_{\rho\,\mu\lambda}(k+p) \\
& (2p+q)_\nu (q-k+p)^\mu (p-k)^\lambda\Big]_{p_0=iw_n} \\
& -2\delta_{3a}\delta_{3b}\frac{ig_\rho^4}{2}T\sum_{n(even)}\Big[\int \frac{d^3p}{(2\pi)^3} D_\pi(p) D_\pi(p+q) \\
& D_{\rho\,\mu\lambda}(q+k+p)(2p+q)_\nu (q-k+p)^\mu (p-k)^\lambda\Big]_{p_0=iw_n} \\
& -2(\delta_{3a}\delta_{3b}+\delta_{ab})\frac{ig_\rho^4}{2}T\sum_{n(even)}\Big[\int \frac{d^3p}{(2\pi)^3} D_\pi(p)^2 D_{\rho\,\mu\lambda}(k+p) \\
& (q_\nu)(k-p)^\mu (k-p)^\lambda\Big]_{p_0=iw_n}. \qquad (4.43)
\end{aligned}
$$

The above integrals can be combined to give:

$$
\begin{aligned}
q^{\mu}\Gamma^{(4)X2}_{\mu\nu\,ab}(k,q) &= -(\delta_{ab}-\delta_{3a}\delta_{3b})\frac{ig_{\rho}^{4}}{2}T\sum_{n(even)}\Bigg[\int\frac{d^{3}p}{(2\pi)^{3}}D_{\pi}(p)D_{\pi}(p+q)D_{\rho\,\mu\lambda}(q+k+p) \\
&\quad (2p+q)_{\nu}(q-k+p)^{\mu}(q+k-p)^{\lambda}\Bigg]_{p_0=iw_n} \\
&\quad -(\delta_{ab}-\delta_{3a}\delta_{3b})\frac{ig_{\rho}^{4}}{2}T\sum_{n(even)}\Bigg[\int\frac{d^{3}p}{(2\pi)^{3}}D_{\pi}(p)D_{\pi}(p+q)D_{\rho\,\mu\lambda}(q-k+p) \\
&\quad (2p+q)_{\nu}(q+k+p)^{\mu}(q-k-p)^{\lambda}\Bigg]_{p_0=iw_n} \\
&\quad . \qquad (4.44)
\end{aligned}
$$

It is now straight forward to show that eq. 4.38 is satisfied by inserting the definition of $\Gamma^{(3)C\rho}_{\mu\,ab3}$ into the right hand side of eq. 4.38.

We now calculate $q^\mu \Gamma^{(4)X3}_{\mu\nu\,ab}$, using eq. 4.29 and 4.30:

$$
\begin{aligned}
q^\mu\Gamma^{(4)X3}_{\mu\nu\,ab}(k,q) \;=\; & \Big\{ -(\delta_{ab}-3\delta_{3a}\delta_{3b})\frac{ig_\rho^4}{2}T\sum_{n(even)}\Big[\int\frac{d^3p}{(2\pi)^3}D_\pi(p)D_\rho^{\mu\alpha}(k+p)D_\rho^{\lambda\beta}(q+k+p)(p-k)_\alpha \\
& (q_\beta)\big(-(2q+k+p)_\mu g_{\nu\lambda}+(q-p-k)_\lambda g_{\mu\nu}+(q+2k+2p)_\nu g_{\mu\lambda}\big)\Big]_{p_0=iw_n} \\
& -(\delta_{ab}+\delta_{3a}\delta_{3b})\frac{ig_\rho^4}{2}T\sum_{n(even)}\Big[\int\frac{d^3p}{(2\pi)^3}D_\pi(p)D_\rho^{\mu\alpha}(k+p)D_\rho^{\lambda\beta}(k+p)(p-k)_\alpha \\
& (p-k)_\beta\big(-(2q+p+k)_\mu g_{\nu\lambda}+(q-p-k)_\lambda g_{\nu\mu}+(q+2k+2p)_\nu g_{\mu\lambda}\big)\Big]_{p_0=iw_n} \\
& +(\delta_{ab}+\delta_{3a}\delta_{3b})\frac{ig_\rho^4}{2}T\sum_{n(even)}\Big[\int\frac{d^3p}{(2\pi)^3}D_\pi(p)D_\rho^{\mu\alpha}(k+p)D_\rho^{\lambda\beta}(q+k+p)(p-k)_\alpha \\
& (p-k)_\beta\big(-(2q+p+k)_\mu g_{\nu\lambda}+(q-p-k)_\lambda g_{\nu\mu}+(q+2k+2p)_\nu g_{\mu\lambda}\big)\Big]_{p_0=iw_n} \\
& +(k\to -k)\Big\} \\
& -2\delta_{3a}\delta_{3b}\frac{ig_\rho^4}{2}T\sum_{n(even)}\Big[\int\frac{d^3p}{(2\pi)^3}D_\pi(p)D_\rho^{\mu\alpha}(k+p)D_\rho^{\lambda\beta}(q+k+p)(p-k)_\alpha \\
& (q-k+p)_\beta(-(2q+p+k)_\mu g_{\nu\lambda}+(q-k-p)_\lambda g_{\mu\nu}+(q+2k+2p)_\nu g_{\mu\lambda})\Big]_{p_0=iw_n} \\
& +2\delta_{3a}\delta_{3b}\frac{ig_\rho^4}{2}T\sum_{n(even)}\Big[\int\frac{d^3p}{(2\pi)^3}D_\pi(p+q)D_\rho^{\mu\alpha}(k+p)D_\rho^{\lambda\beta}(q+k+p)(p-k)_\alpha \\
& (q-k+p)_\beta(-(2q+p+k)_\mu g_{\nu\lambda}+(q-k-p)_\lambda g_{\mu\nu}+(q+2k+2p)_\nu g_{\mu\lambda})\Big]_{p_0=iw_n} \\
& -2(\delta_{3a}\delta_{3b}+\delta_{ab})\frac{ig_\rho^4}{2}T\sum_{n(even)}\Big[\int\frac{d^3p}{(2\pi)^3}D_\pi(p)D_\rho^{\mu\alpha}(k+p)D_\rho^{\lambda\beta}(k+p) \\
& (k-p)_\alpha(k-p)_\beta(q_\mu g_{\nu\lambda}+q_\lambda g_{\mu\nu}-2q_\nu g_{\mu\lambda})\Big]_{p_0=iw_n}. \qquad (4.45)
\end{aligned}
$$

After performing some algebra one can rewrite the above equations as:

$$
\begin{aligned}
q^{\mu}\Gamma^{(4)X3}_{\mu\nu\,ab}(k,q) &= (\delta_{ab}-\delta_{3a}\delta_{3b})\frac{ig_{\rho}^{4}}{2}T\sum_{n(even)}\Bigg[\int\frac{d^{3}p}{(2\pi)^{3}}D_{\pi}(p)D_{\rho}^{\mu\alpha}(k+p)D_{\rho}^{\lambda\beta}(q+k+p)(k-p)_{\alpha} \\
&\quad (q+k-p)_{\beta}(-(2q+p+k)_{\mu}g_{\nu\lambda}+(q-k-p)_{\lambda}g_{\mu\nu}+(q+2k+2p)_{\nu}g_{\mu\lambda})\Bigg]_{p_0=iw_n} \\
&\quad -(\delta_{ab}-\delta_{3a}\delta_{3b})\frac{ig_{\rho}^{4}}{2}T\sum_{n(even)}\Bigg[\int\frac{d^{3}p}{(2\pi)^{3}}D_{\pi}(p)D_{\rho}^{\mu\alpha}(-k+p)D_{\rho}^{\lambda\beta}(q-k+p)(k+p)_{\alpha} \\
&\quad (q-k-p)_{\beta}(-(2q+p-k)_{\mu}g_{\nu\lambda}+(q+k-p)_{\lambda}g_{\mu\nu}+(q-2k+2p)_{\nu}g_{\mu\lambda})\Bigg]_{p_0=iw_n}.
\end{aligned}
\tag{4.46}
$$

It is straight forward to show the right hand side of eq. 4.39 is equal to the above expression, using the definition of $\Gamma^{(3)D\rho}_{\mu\,ab3}$.

Finally, we show that 4.40 holds. One can use eq. 4.29 to show:

$$
\begin{aligned}
q^{\mu}\Gamma^{(4)X4}_{\mu\nu\,ab}(k,q) &= \Big\{(\delta_{ab}-\delta_{3a}\delta_{3b})\frac{ig_{\rho}^{2}g_{\sigma}^{2}}{2}T\sum_{n(even)}\Bigg[\int\frac{d^{3}p}{(2\pi)^{3}}D_{\pi}(p)^{2}D_{\sigma}(k+p) \\
&\quad ((k+p)^{2}-m_{\pi}^{2})(2p+q)_{\nu}\Bigg]_{p_0=iw_n} \\
&\quad -\Big\{(\delta_{ab}-\delta_{3a}\delta_{3b})\frac{ig_{\rho}^{2}g_{\sigma}^{2}}{2}T\sum_{n(even)}\Bigg[\int\frac{d^{3}p}{(2\pi)^{3}}D_{\pi}(p)D_{\pi}(p+q)D_{\sigma}(k+p) \\
&\quad ((k+p)^{2}-m_{\pi}^{2})(2p+q)_{\nu}\Bigg]_{p_0=iw_n}+(k\to -k)\Big\} \\
&\quad -2(\delta_{ab}-\delta_{3a}\delta_{3b})\frac{ig_{\rho}^{2}g_{\sigma}^{2}}{2}T\sum_{n(even)}\Bigg[\int\frac{d^{3}p}{(2\pi)^{3}}D_{\pi}(p)^{2}D_{\sigma}(k+p) \\
&\quad ((k+p)^{2}-m_{\pi}^{2})q_{\nu}\Bigg]_{p_0=iw_n}.
\end{aligned}
\tag{4.47}
$$

One can rewrite the above equation as:

$$
\begin{aligned}
q^{\mu}\Gamma^{(4)X4}_{\mu\nu\,ab}(k,q) &= -(\delta_{ab}-\delta_{3a}\delta_{3b})\frac{ig_{\rho}^{2}g_{\sigma}^{2}}{2}T\sum_{n(even)}\Bigg[\int\frac{d^{3}p}{(2\pi)^{3}}D_{\pi}(p)D_{\pi}(p-q)D_{\sigma}(-q+k+p) \\
&\quad ((-q+k+p)^{2}-m_{\pi}^{2})(2p-q)_{\nu}\Bigg]_{p_{0}=iw_{n}} \\
&\quad +(\delta_{ab}-\delta_{3a}\delta_{3b})\frac{ig_{\rho}^{2}g_{\sigma}^{2}}{2}T\sum_{n(even)}\Bigg[\int\frac{d^{3}p}{(2\pi)^{3}}D_{\pi}(p)D_{\pi}(p-q)D_{\sigma}(k+p) \\
&\quad ((k+p)^{2}-m_{\pi}^{2})(2p-q)_{\nu}\Bigg]_{p_{0}=iw_{n}}, \qquad (4.48)
\end{aligned}
$$

which is equal to the right hand side of eq. 4.40. Thus we see that the listed vertex corrections fulfill the Ward identities.

4.4 Vertex correction form factors

In this section, we introduce form factors to the vertex corrections. Ref. [46] calculated interactions of pions with nucleons, and implemented non-relativistic approximations. Consequently, ref. [46]'s πNN and $\pi N\Delta$ form factors, depended only on the pion's three-momentum (the lab frame momentum). For example, if Σ_{π}^{0} is the pion self-energy without form factors, the regularized pion self-energy is given by:

$$
\bar{\Sigma}_{\pi}(k)=\Sigma_{\pi}^{0}(k)\Big(\frac{\Lambda_{1}^{2}}{\Lambda_{2}^{2}+\vec{k}^{2}}\Big)^{2}, \qquad (4.49)
$$

where we write a bar over the self-energy to denote regularization with the lab frame momentum. We have deviated slightly from reference [46], in that their form factor used the same cut off in the numerator and denominator. We write a more general form factor, however reference [46]'s formalism can easily be extended to this case. Reference [46] generated the form factor by attaching a heavy pion propagator, $\frac{1}{-\vec{k}^{2}-\Lambda_{2}^{2}}$, to the external pions in Σ_{π}, and assigning a factor of $i\Lambda_{1}^{2}$ to the "vertex" were the pion is converted to a heavy pion. This method was also used to regularize

the vertex corrections, $\Gamma'^{(3)}_{\mu\,ab3}$ and $\Gamma'^{(4)}_{\mu\nu\,ab33}$, giving:

$$\begin{aligned}\bar{\Gamma}^{(3)}_{\mu\,ab3}(k,q) &= \Gamma'^{(3)}_{\mu\,ab3}(k,q)\Big(\frac{\Lambda_1^2}{\Lambda_2^2+\vec{k}^2}\Big)\Big(\frac{\Lambda_1^2}{\Lambda_2^2+(\vec{q}+\vec{k})^2}\Big),\\ \bar{\Gamma}^{(4)}_{\mu\nu\,ab33}(k,q) &= \Gamma'^{(4)}_{\mu\nu\,ab33}(k,q)\Big(\frac{\Lambda_1^2}{\Lambda_2^2+\vec{k}^2}\Big)^2,\end{aligned} \tag{4.50}$$

where $\bar{\Gamma}'^{(3)}_{\mu\,ab3}$ and $\bar{\Gamma}'^{(4)}_{\mu\nu\,ab33}$ denote vertex corrections that are regularized with the lab frame momentum. However, the regularized corrections violate the Ward identities, because the pion self-energy and the corrections to the $\rho\rho\pi\pi$ vertex are regularized by $\Big(\frac{\Lambda_1^2}{\Lambda_2^2+\vec{k}^2}\Big)^2$ while the corrections to the $\rho\pi\pi$ vertex are regularized by $\Big(\frac{\Lambda_1^2}{\Lambda_2^2+\vec{k}^2}\Big)\Big(\frac{\Lambda_1^2}{\Lambda_2^2+(\vec{q}+\vec{k})^2}\Big)$. Therefore, the form factors generate violations of eqs. 4.2 and 4.3 given by:

$$\begin{aligned}V_3(k,q) &= g_\rho\epsilon_{3ab}\big(-\Sigma^0_\pi(k+q)\big[FF_0(q+k)^2-FF_0(q+k)FF_0(k)\big]\\ &\quad+\Sigma^0_\pi(k)\big[FF_0(k)^2-FF_0(q+k)FF_0(k)\big]\big),\end{aligned} \tag{4.51}$$

$$\begin{aligned}V_4(k,q) &= ig_\rho\big(\epsilon_{3ca}\Gamma'^{(3)}_{\nu\,bc3}(k,-q)\big[FF_0(k)FF_0(-q+k)-FF_0(-q+k)^2\big]\\ &\quad-\epsilon_{3bc}\Gamma'^{(3)}_{\nu\,ca3}(k+q,-q)\big[FF_0(q+k)FF_0(k)-FF_0(k)^2\big]\big),\end{aligned} \tag{4.52}$$

with,

$$FF_0(k)=\frac{\Lambda_1^2}{\Lambda_2^2+\vec{k}^2}. \tag{4.53}$$

$$\frac{\Lambda_1^2}{\Lambda_2^2+\vec{k}^2}\to\frac{\Lambda_1^2}{\Lambda_2^2+q_{\rm CM}[p,k]^2} \tag{4.54}$$

In ref. [46] additional vertex corrections were generated to remove this violation. The additional vertex corrections can be derived by coupling a rho meson to the heavy pion propagators. In figure 4.8 we represent this schema diagrammatically for the pion self-energy and the vertex corrections to the $\rho\pi\pi$ vertex.

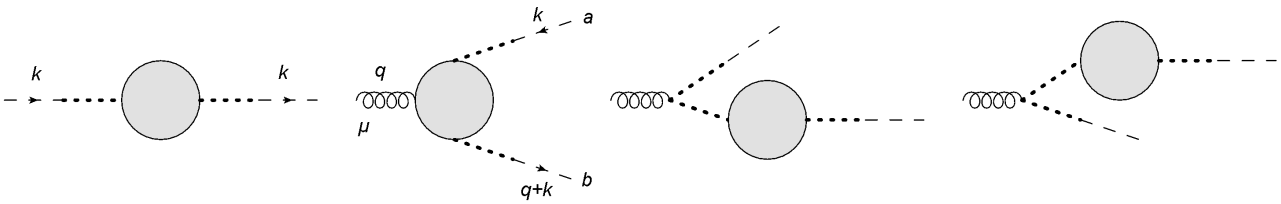

Figure 4.8: From left to right: the pion self-energy regularized with heavy pion propagators, the vertex corrections to the $\rho\pi\pi$ vertex regularized with heavy pion propagators, and additional vertex corrections generated by coupling a rho meson to a heavy pion propagator in the pion self-energy.

Similarly, one can generate corrections to the $\rho\rho\pi\pi$ vertex by coupling two rho mesons to heavy pion propagators [46], as demonstrated in figure 4.9.

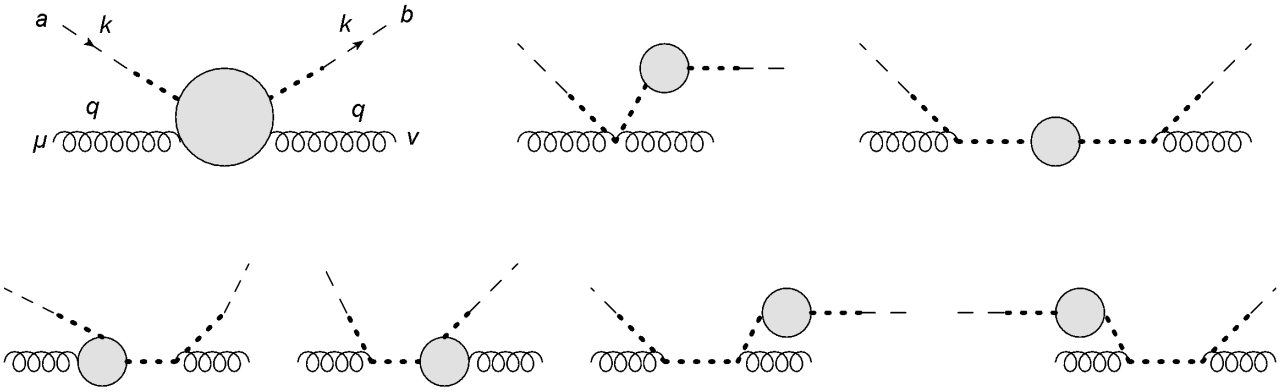

Figure 4.9: The regularized $\rho\rho\pi\pi$ vertex corrections, and the additional vertex corrections to the $\rho\rho\pi\pi$ vertex generated by coupling two rho mesons to heavy pion propagators in the pion self-energy.

The additional vertex corrections can be expressed in terms of the pion self-energy and the original corrections to the $\rho\pi\pi$ vertex, such that the total regularized vertex corrections become

[46]:

$$\begin{aligned}
\tilde{\Gamma}^{(3)}_{\mu\,ab3}(k,q) &= \Gamma'^{(3)}_{\mu\,ab3}(k,q)\Big(\frac{\Lambda_1^2}{\Lambda_2^2+\vec{k}^2}\Big)\Big(\frac{\Lambda_1^2}{\Lambda_2^2+(\vec{q}+\vec{k})^2}\Big) \\
&\quad +g_\rho\epsilon_{3ab}(2k+q)_i\Big(\frac{\Sigma_\pi^0(q+k)}{\Lambda_2^2+\vec{k}^2}\Big(\frac{\Lambda_1^2}{\Lambda_2^2+(\vec{q}+\vec{k})^2}\Big)^2+\frac{\Sigma_\pi^0(k)}{\Lambda_2^2+(\vec{q}+\vec{k})^2}\Big(\frac{\Lambda_1^2}{\Lambda_2^2+\vec{k}^2}\Big)^2\Big),
\end{aligned} \tag{4.55}$$

$$\begin{aligned}
\tilde{\Gamma}^{(4)}_{\mu\nu\,ab33}(k,q) &= \Gamma'^{(4)}_{\mu\nu\,ab33}(k,q)\Big(\frac{\Lambda_1^2}{\Lambda_2^2+\vec{k}^2}\Big)^2 \\
&\quad -\frac{ig_\rho\epsilon_{3ca}}{\Lambda_2^2+\vec{k}^2}\Big[(2k-q)_i\Gamma'^{(3)}_{\nu\,bc3}(k,-q)\Big(\frac{\Lambda_1^2}{\Lambda_2^2+\vec{k}^2}\Big)\Big(\frac{\Lambda_1^2}{\Lambda_2^2+(-\vec{q}+\vec{k})^2}\Big) \\
&\quad +(2k+q)_j\Gamma'^{(3)}_{\mu\,cb3}(-q-k,q)\Big(\frac{\Lambda_1^2}{\Lambda_2^2+\vec{k}^2}\Big)\Big(\frac{\Lambda_1^2}{\Lambda_2^2+(\vec{q}+\vec{k})^2}\Big)\Big] \\
&\quad -\frac{ig_\rho\epsilon_{3bc}}{\Lambda_2^2+\vec{k}^2}\Big[(2k+q)_i\Gamma'^{(3)}_{\nu\,ac3}(-k,-q)\Big(\frac{\Lambda_1^2}{\Lambda_2^2+\vec{k}^2}\Big)\Big(\frac{\Lambda_1^2}{\Lambda_2^2+(\vec{q}+\vec{k})^2}\Big) \\
&\quad +(2k-q)_j\Gamma'^{(3)}_{\mu\,ca3}(-q+k,q)\Big(\frac{\Lambda_1^2}{\Lambda_2^2+\vec{k}^2}\Big)\Big(\frac{\Lambda_1^2}{\Lambda_2^2+(-\vec{q}+\vec{k})^2}\Big)\Big] \\
&\quad -ig_\rho^2(\delta_{ab}-\delta_{3a}\delta_{3b})\Bigg\{(2k-q)_i(2k-q)_j\Bigg[\frac{\Sigma_\pi^0(-q+k)}{(\Lambda_2^2+\vec{k}^2)^2}\Big(\frac{\Lambda_1^2}{\Lambda_2^2+(-\vec{q}+\vec{k})^2}\Big)^2 \\
&\quad +\frac{2\Sigma_\pi^0(k)}{(\Lambda_2^2+(-\vec{q}+\vec{k})^2)(\Lambda_2^2+\vec{k}^2)}\Big(\frac{\Lambda_1^2}{\Lambda_2^2+\vec{k}^2}\Big)^2\Bigg] \\
&\quad +(2k+q)_i(2k+q)_j\Bigg[\frac{\Sigma_\pi^0(q+k)}{(\Lambda_2^2+\vec{k}^2)^2}\Big(\frac{\Lambda_1^2}{\Lambda_2^2+(\vec{q}+\vec{k})^2}\Big)^2 \\
&\quad +\frac{2\Sigma_\pi^0(k)}{(\Lambda_2^2+(\vec{q}+\vec{k})^2)(\Lambda_2^2+\vec{k}^2)}\Big(\frac{\Lambda_1^2}{\Lambda_2^2+\vec{k}^2}\Big)^2\Bigg] \\
&\quad -4\delta_{ij}\frac{\Sigma_\pi^0(k)}{\Lambda_2^2+\vec{k}^2}\Big(\frac{\Lambda_1^2}{\Lambda_2^2+\vec{k}^2}\Big)^2\Bigg\},
\end{aligned} \tag{4.56}$$

where the short-hand i and j are used to represent the spatial components of μ and ν. For $i=0$ or $j=0$ the corresponding term should be dropped.

It is straight forward to show that the above procedure satisfies the Ward identities, if $\Gamma'^{(3)}_{\mu\,ab3}$ and $\Gamma'^{(4)}_{\mu\nu\,ab33}$ satisfy eqs. 4.2 and 4.3. However, there are two complications that arise when applying the regularization procedure from ref. [46] with the form factors introduced in chapter 3. First, in chapter 3 different form factors were introduce for the S- and P-wave contributions to the self-

energy, and second, the center of mass momentum was used to define the form factors in chapter 3.

In order to extend the approach from ref. [46] to multiple form factors we note that $\Sigma^0_{\pi(\rho)}$ and its vertex corrections ($\Gamma'^{(3)\rho}_{\mu\, ab3}$ and $\Gamma'^{(4)\rho}_{\mu\nu\, ab33}$) independently satisfy eqs. 4.2 and 4.3, such that:

$$\begin{aligned} q^\mu \Gamma'^{(3)\rho}_{\mu\, ab3} &= g_\rho \epsilon_{3ab}(-\Sigma^0_{\pi(\rho)}(k+q) + \Sigma^0_{\pi(\rho)}(k)), && (4.57)\\ q^\mu \Gamma'^{(4)\rho}_{\mu\nu\, ab33} &= i g_\rho(\epsilon_{3ca}\Gamma'^{(3)\rho}_{\nu\, bc3}(k,-q) - \epsilon_{3bc}\Gamma'^{(3)\rho}_{\nu\, ca3}(k+q,-q)). && (4.58)\end{aligned}$$

Similarly, $\Sigma^0_{\pi(\sigma)}$ and its vertex corrections ($\Gamma'^{(3)\sigma}_{\mu\, ab3}$ and $\Gamma'^{(4)\sigma}_{\mu\nu\, ab33}$) satisfy:

$$\begin{aligned} q^\mu \Gamma'^{(3)\sigma}_{\mu\, ab3} &= g_\rho \epsilon_{3ab}(-\Sigma^0_{\pi(\sigma)}(k+q) + \Sigma^0_{\pi(\sigma)}(k)), && (4.59)\\ q^\mu \Gamma'^{(4)\sigma}_{\mu\nu\, ab33} &= i g_\rho(\epsilon_{3ca}\Gamma'^{(3)\sigma}_{\nu\, bc3}(k,-q) - \epsilon_{3bc}\Gamma'^{(3)\sigma}_{\nu\, ca3}(k+q,-q)). && (4.60)\end{aligned}$$

Equations 4.57 through 4.60 demonstrate that the sigma and rho resonances form subgroups that independently satisfy the Ward identities. Thus, the regularization procedure from ref. [46] can be applied separately to S- and P-wave scattering, using the appropriate form factor for each case. The total regularized vertex corrections are then just the sum of the corrections for the rho and sigma resonances:

$$\begin{aligned} \tilde{\Gamma}^{(3)}_{\mu\, ab3}(k,q) &= \Gamma'^{(3)\rho}_{\mu\, ab3}(k,q)\Big(\frac{\Lambda^2_{1\rho}}{\Lambda^2_{2\rho}+\vec{k}^2}\Big)\Big(\frac{\Lambda^2_{1\rho}}{\Lambda^2_{2\rho}+(\vec{q}+\vec{k})^2}\Big) + \Gamma'^{(3)\sigma}_{\mu\, ab3}(k,q)\Big(\frac{\Lambda^2_{1\sigma}}{\Lambda^2_{2\sigma}+\vec{k}^2}\Big)\Big(\frac{\Lambda^2_{1\sigma}}{\Lambda^2_{2\sigma}+(\vec{q}+\vec{k})^2}\Big)\\ &\quad + g_\rho\epsilon_{3ab}(2k+q)_i\Big(\frac{\Sigma^0_{\pi(\rho)}(q+k)}{\Lambda^2_{2\rho}+\vec{k}^2}\Big(\frac{\Lambda^2_{1\rho}}{\Lambda^2_{2\rho}+(\vec{q}+\vec{k})^2}\Big)^2 + \frac{\Sigma^0_{\pi(\rho)}(k)}{\Lambda^2_{2\rho}+(\vec{q}+\vec{k})^2}\Big(\frac{\Lambda^2_{1\rho}}{\Lambda^2_{2\rho}+\vec{k}^2}\Big)^2\Big)\\ &\quad + g_\rho\epsilon_{3ab}(2k+q)_i\Big(\frac{\Sigma^0_{\pi(\sigma)}(q+k)}{\Lambda^2_{2\sigma}+\vec{k}^2}\Big(\frac{\Lambda^2_{1\sigma}}{\Lambda^2_{2\sigma}+(\vec{q}+\vec{k})^2}\Big)^2 + \frac{\Sigma^0_{\pi(\sigma)}(k)}{\Lambda^2_{2\sigma}+(\vec{q}+\vec{k})^2}\Big(\frac{\Lambda^2_{1\sigma}}{\Lambda^2_{2\sigma}+\vec{k}^2}\Big)^2\Big), \end{aligned} \quad (4.61)$$

$$
\begin{aligned}
\tilde{\Gamma}^{(4)}_{\mu\nu\,ab33}(k,q) &= \Gamma'^{(4)\rho}_{\mu\nu\,ab33}(k,q)\Big(\frac{\Lambda_{1\rho}^2}{\Lambda_{2\rho}^2+\vec{k}^2}\Big)^2+\Gamma'^{(4)\sigma}_{\mu\nu\,ab33}(k,q)\Big(\frac{\Lambda_{1\sigma}^2}{\Lambda_{2\sigma}^2+\vec{k}^2}\Big)^2\\
&-\frac{ig_\rho\epsilon_{3ca}}{\Lambda_{2\rho}^2+\vec{k}^2}\Big[(2k-q)_i\Gamma'^{(3)\rho}_{\nu\,bc3}(k,-q)\Big(\frac{\Lambda_{1\rho}^2}{\Lambda_{2\rho}^2+\vec{k}^2}\Big)\Big(\frac{\Lambda_{1\rho}^2}{\Lambda_{2\rho}^2+(-\vec{q}+\vec{k})^2}\Big)\\
&+(2k+q)_j\Gamma'^{(3)\rho}_{\mu\,cb3}(-q-k,q)\Big(\frac{\Lambda_{1\rho}^2}{\Lambda_{2\rho}^2+\vec{k}^2}\Big)\Big(\frac{\Lambda_{1\rho}^2}{\Lambda_{2\rho}^2+(\vec{q}+\vec{k})^2}\Big)\\
&+(2k-q)_i\Gamma'^{(3)\sigma}_{\nu\,bc3}(k,-q)\Big(\frac{\Lambda_{1\sigma}^2}{\Lambda_{2\sigma}^2+\vec{k}^2}\Big)\Big(\frac{\Lambda_{1\sigma}^2}{\Lambda_{2\sigma}^2+(-\vec{q}+\vec{k})^2}\Big)\\
&+(2k+q)_j\Gamma'^{(3)\sigma}_{\mu\,cb3}(-q-k,q)\Big(\frac{\Lambda_{1\sigma}^2}{\Lambda_{2\sigma}^2+\vec{k}^2}\Big)\Big(\frac{\Lambda_{1\sigma}^2}{\Lambda_{2\sigma}^2+(\vec{q}+\vec{k})^2}\Big)\Big]\\
&-\frac{ig_\rho\epsilon_{3bc}}{\Lambda_{2\rho}^2+\vec{k}^2}\Big[(2k+q)_i\Gamma'^{(3)\rho}_{\nu\,ac3}(-k,-q)\Big(\frac{\Lambda_{1\rho}^2}{\Lambda_{2\rho}^2+\vec{k}^2}\Big)\Big(\frac{\Lambda_{1\rho}^2}{\Lambda_{2\rho}^2+(\vec{q}+\vec{k})^2}\Big)\\
&+(2k-q)_j\Gamma'^{(3)\rho}_{\mu\,ca3}(-q+k,q)\Big(\frac{\Lambda_{1\rho}^2}{\Lambda_{2\rho}^2+\vec{k}^2}\Big)\Big(\frac{\Lambda_{1\rho}^2}{\Lambda_{2\rho}^2+(-\vec{q}+\vec{k})^2}\Big)\\
&+(2k+q)_i\Gamma'^{(3)\sigma}_{\nu\,ac3}(-k,-q)\Big(\frac{\Lambda_{1\sigma}^2}{\Lambda_{2\sigma}^2+\vec{k}^2}\Big)\Big(\frac{\Lambda_{1\sigma}^2}{\Lambda_{2\sigma}^2+(\vec{q}+\vec{k})^2}\Big)\\
&+(2k-q)_j\Gamma'^{(3)\sigma}_{\mu\,ca3}(-q+k,q)\Big(\frac{\Lambda_{1\sigma}^2}{\Lambda_{2\sigma}^2+\vec{k}^2}\Big)\Big(\frac{\Lambda_{1\sigma}^2}{\Lambda_{2\sigma}^2+(-\vec{q}+\vec{k})^2}\Big)\Big]\\
&-ig_\rho^2(\delta_{ab}-\delta_{3a}\delta_{3b})\Bigg\{(2k-q)_i(2k-q)_j\Bigg[\frac{\Sigma^0_{\pi(\rho)}(-q+k)}{(\Lambda_{2\rho}^2+\vec{k}^2)^2}\Big(\frac{\Lambda_{1\rho}^2}{\Lambda_{2\rho}^2+(-\vec{q}+\vec{k})^2}\Big)^2\\
&+\frac{2\Sigma^0_{\pi(\rho)}(k)}{(\Lambda_{2\rho}^2+(-\vec{q}+\vec{k})^2)(\Lambda_{2\rho}^2+\vec{k}^2)}\Big(\frac{\Lambda_{1\rho}^2}{\Lambda_{2\rho}^2+\vec{k}^2}\Big)^2+\frac{\Sigma^0_{\pi(\sigma)}(-q+k)}{(\Lambda_{2\sigma}^2+\vec{k}^2)^2}\Big(\frac{\Lambda_{1\sigma}^2}{\Lambda_{2\sigma}^2+(-\vec{q}+\vec{k})^2}\Big)^2\\
&+\frac{2\Sigma^0_{\pi(\sigma)}(k)}{(\Lambda_{2\sigma}^2+(-\vec{q}+\vec{k})^2)(\Lambda_{2\sigma}^2+\vec{k}^2)}\Big(\frac{\Lambda_{1\sigma}^2}{\Lambda_{2\sigma}^2+\vec{k}^2}\Big)^2\Bigg]\\
&+(2k+q)_i(2k+q)_j\Bigg[\frac{\Sigma^0_{\pi(\rho)}(q+k)}{(\Lambda_{2\rho}^2+\vec{k}^2)^2}\Big(\frac{\Lambda_{1\rho}^2}{\Lambda_{2\rho}^2+(\vec{q}+\vec{k})^2}\Big)^2\\
&+\frac{2\Sigma^0_{\pi(\rho)}(k)}{(\Lambda_{2\rho}^2+(\vec{q}+\vec{k})^2)(\Lambda_{2\rho}^2+\vec{k}^2)}\Big(\frac{\Lambda_{1\rho}^2}{\Lambda_{2\rho}^2+\vec{k}^2}\Big)^2+\frac{\Sigma^0_{\pi(\sigma)}(q+k)}{(\Lambda_{2\sigma}^2+\vec{k}^2)^2}\Big(\frac{\Lambda_{1\sigma}^2}{\Lambda_{2\sigma}^2+(\vec{q}+\vec{k})^2}\Big)^2\\
&+\frac{2\Sigma^0_{\pi(\sigma)}(k)}{(\Lambda_{2\sigma}^2+(\vec{q}+\vec{k})^2)(\Lambda_{2\sigma}^2+\vec{k}^2)}\Big(\frac{\Lambda_{1\sigma}^2}{\Lambda_{2\sigma}^2+\vec{k}^2}\Big)^2\Bigg]\\
&-4\delta_{ij}\frac{\Sigma^0_{\pi(\rho)}(k)}{\Lambda_{2\rho}^2+\vec{k}^2}\Big(\frac{\Lambda_{1\rho}^2}{\Lambda_{2\rho}^2+\vec{k}^2}\Big)^2-4\delta_{ij}\frac{\Sigma^0_{\pi(\sigma)}(k)}{\Lambda_{2\sigma}^2+\vec{k}^2}\Big(\frac{\Lambda_{1\sigma}^2}{\Lambda_{2\sigma}^2+\vec{k}^2}\Big)^2\Bigg\}. \qquad (4.62)
\end{aligned}
$$

Next we address the uses of the center of mass momentum in the form factor. For $\pi\pi$-scattering we cannot apply the non-relativistic approximations used in ref. [46]. Therefore, we utilize a form factor depending on the center of mass momentum (q_{CM}). Furthermore, the dependence on q_{CM} rather than $\vec{k}$ prevents the introduction of spurious momentum dependencies. While, the use of q_{CM} makes the pion self-energy more robust, it is not clear how to satisfy the Ward identities in this framework. However, one can see from eqs. 4.51 and 4.52 that the violation of the Ward identities is proportional to a difference between form factors. For q_{CM} this difference becomes:

$$\begin{aligned}
\tilde{\text{X}}_{(\rho/\sigma)}[p,k] &= \big(\text{FF}_{(\rho/\sigma)}[p,k]^2 - \text{FF}_{(\rho/\sigma)}[-q+p,q+k]\text{FF}_{(\rho/\sigma)}[p,k]\big) \\
&= \text{FF}_{(\rho/\sigma)}[p,k]^2\text{FF}_{(\rho/\sigma)}[-q+p,q+k] \\
&\quad \big(\text{FF}_{(\rho/\sigma)}[-q+p,q+k]^{-1} - \text{FF}_{(\rho/\sigma)}[p,k]^{-1}\big) \\
&= \text{FF}_{(\rho/\sigma)}[p,k]\text{FF}_{(\rho/\sigma)}[-q+p,q+k]\frac{\big(q_{\text{CM}}[-q+p,q+k]^2 - q_{\text{CM}}[p,k]^2\big)}{\Lambda_{2(\rho/\sigma)}^2 + q_{\text{CM}}[p,k]^2} \\
&= \text{FF}_{(\rho/\sigma)}[p,k]\text{FF}_{(\rho/\sigma)}[-q+p,q+k]\frac{1}{(\Lambda_{2(\rho/\sigma)}^2 + q_{\text{CM}}[p,k]^2)(p+k)^2} \\
&\quad \big[(q\cdot k)^2 + 2k^2(q\cdot p) + 2(q\cdot k)(q\cdot p) + (q\cdot p)^2 - k^2q^2 \\
&\quad -p^2(2q\cdot k + q^2) - 2(p\cdot k)(q\cdot k - q\cdot p + q^2)\big]. \qquad (4.63)
\end{aligned}$$

One can see from eq. 4.63 that the violation is proportional to a difference in pion momentum squared over $\Lambda_{2(\rho/\sigma)}^2$. In order to extract the electric conductivity one must calculate the zero momentum low energy limit. In this limit the violation is suppressed, because $\Lambda_{2(\rho/\sigma)}$ is on the order of several hundred MeV, while the difference in q_{CM}s is on the order of a few MeV. Therefore, the violation of gauge invariance due to adding the form factor will be suppressed at small q_0. This is expected because form factors are constructed to constrain high energy behavior, while minimally affecting the low energy regime.

Furthermore, the leading order in the numerator of 4.63 goes like q_0^2, while $\Lambda_{2\rho}$ is on the order of 1 GeV for the rho resonance. Thus, the violation due to the form factors in $\Sigma_{\pi(\rho)}$ should still be suppressed around the rho mass. Although $\Lambda_{2\sigma}$ is significantly smaller ($\approx 400\,\text{MeV}$) than m_ρ,

the effects of $\pi\pi$-resonant scattering through a sigma resonance on the EM spectral function are suppressed for large q_0. Therefore, the violation of gauge invariance due to using q_{CM} in the form factor is expected to be small even for q_0 around the rho mass. Thus, we will follow the approach of ref. [46] in generating form factors and the additional vertex corrections involving heavy pion propagators, however, at the vertices where a heavy pion propagator couples to a thermal loop we will replace the lab frame momentum, $\vec{k}$, with the center of mass momentum, $q_{\rm CM}$. The regularized vertex corrections then become:

$$\Gamma''^{(4)A\rho}_{\mu\nu\,ab33}(k,q) = (-3\delta_{3a}\delta_{3b}+5\delta_{ab})\frac{ig_\rho^4}{2}T\sum_{n(even)}\Bigg[\int\frac{d^3p}{(2\pi)^3}D_\pi(p)D_\rho^{\mu\nu}(q+k+p)$$
$$\mathbf{FF}_\rho[q+p,k]^2\Bigg]_{p_0=iw_n}+(k\to -k), \tag{4.64}$$
$$\Gamma''^{(4)B_1\rho}_{\mu\nu\,ab33}(k,q) = -2\delta_{ab}\frac{ig_\rho^4}{2}T\sum_{n(even)}\Bigg[\int\frac{d^3p}{(2\pi)^3}D_\pi(p)D_\pi(p+q)D_{\rho\nu\beta}(k+p)$$
$$(2p+q)_\mu(p-k)^\beta\mathbf{FF}_\rho[p,k]^2\Bigg]_{p_0=iw_n}+(k\to -k)), \tag{4.65}$$
$$\Gamma''^{(4)C_1\rho}_{\mu\nu\,ab33}(k,q) = -(\delta_{ab}-3\delta_{3a}\delta_{3b})\frac{ig_\rho^4}{2}T\sum_{n(even)}\Bigg[\int\frac{d^3p}{(2\pi)^3}D_\pi(p)D_\rho^{\lambda\beta}(k+p)D_\rho^{\gamma\alpha}(q+k+p)$$
$$(p-k)_\beta g_{\alpha\nu}(-(2q+k+p)_\lambda g_{\mu\gamma}-(-q+p+k)_\gamma g_{\mu\lambda}+(q+2k+2p)_\mu g_{\gamma\lambda})$$
$$\mathbf{FF}_\rho[p,k]\mathbf{FF}_\rho[q+p,k]\Bigg]_{p_0=iw_n}+(k\to -k)), \tag{4.66}$$
$$\Gamma''^{(4)D\rho}_{\mu\nu\,ab33}(k,q) = (\delta_{ab}+\delta_{3a}\delta_{3b})\frac{ig_\rho^4}{2}T\sum_{n(even)}\Bigg[\int\frac{d^3p}{(2\pi)^3}D_\pi(p)D_\rho^{\phi\theta}(k+p)$$
$$D_\rho^{\gamma\lambda}(k+p)D_\rho^{\alpha\beta}(q+k+p)(p-k)_\theta(p-k)_\lambda$$
$$((q-p-k)_\alpha g_{\mu\gamma}-(2q+p+k)_\gamma g_{\mu\alpha}+(q+2k+2p)_\mu g_{\gamma\alpha})$$
$$((q-p-k)_\beta g_{\nu\phi}-(2q+p+k)_\phi g_{\nu\beta}+(q+2k+2p)_\nu g_{\beta\phi})$$
$$\mathbf{FF}_\rho[p,k]^2\Bigg]_{p_0=iw_n}+(k\to -k), \tag{4.67}$$
$$\Gamma''^{(4)E\rho}_{\mu\nu\,ab33}(k,q) = (\delta_{ab}+\delta_{3a}\delta_{3b})\frac{ig_\rho^4}{2}T\sum_{n(even)}\Bigg[\int\frac{d^3p}{(2\pi)^3}D_\pi(p)^2D_\pi(p+q)D_\rho(k+p)_{\alpha\beta}$$
$$(2p+q)_\mu(p-k)^\alpha(p-k)^\beta(2p+q)_\nu$$
$$\mathbf{FF}_\rho[p,k]^2\Bigg]_{p_0=iw_n}+(k\to -k), \tag{4.68}$$

$$\Gamma''^{(4)F_1\rho}_{\mu\nu\,ab33}(k,q) = -2\delta_{3a}\delta_{3b}\frac{ig_\rho^4}{2}T\sum_{n(even)}\Bigg[\int\frac{d^3p}{(2\pi)^3}D_\pi(p)D_\pi(p+q)D_\rho^{\gamma\lambda}(k+p)$$
$$D_\rho^{\alpha\beta}(q+k+p)(q-k+p)_\beta(2p+q)_\nu(p-k)_\lambda$$
$$((q-k-p)_\alpha g_{\mu\gamma}-(2q+p+k)_\gamma g_{\mu\alpha}+(q+2k+2p)_\mu g_{\gamma\alpha})$$
$$\mathrm{FF}_\rho[p,k]\mathrm{FF}_\rho[q+p,k]\Bigg]\Bigg|_{p_0=iw_n}, \tag{4.69}$$

$$\Gamma''^{(4)G\rho}_{\mu\nu\,ab33}(k,q) = -2(\delta_{3a}\delta_{3b}+\delta_{ab})\frac{ig_\rho^4}{2}T\sum_{n(even)}\Bigg[\int\frac{d^3p}{(2\pi)^3}D_\pi(p)^2D_\rho^{\alpha\beta}(k+p)$$
$$(k-p)_\alpha(k-p)_\beta g_{\mu\nu}\mathrm{FF}_\rho[p,k]^2\Bigg]\Bigg|_{p_0=iw_n}, \tag{4.70}$$

$$\Gamma''^{(4)H\rho}_{\mu\nu\,ab33}(k,q) = -2(\delta_{3a}\delta_{3b}+\delta_{ab})\frac{ig_\rho^4}{2}T\sum_{n(even)}\Bigg[\int\frac{d^3p}{(2\pi)^3}D_\pi(p)D_\rho^{\alpha\lambda}(k+p)D_\rho^{\beta\gamma}(k+p)$$
$$(k-p)_\alpha(k-p)_\beta(g_{\mu\lambda}g_{\nu\gamma}+g_{\mu\gamma}g_{\nu\lambda}-2g_{\mu\nu}g_{\lambda\gamma})$$
$$\mathrm{FF}_\rho[p,k]^2\Bigg]\Bigg|_{p_0=iw_n}, \tag{4.71}$$

$$\Gamma''^{(4)E\sigma}_{\mu\nu\,ab33}(k,q) = (\delta_{ab}-\delta_{3a}\delta_{3b})\frac{ig_\rho^2g_\sigma^2}{2}T\sum_{n(even)}\Bigg[\int\frac{d^3p}{(2\pi)^3}D_\pi(p)^2D_\pi(p+q)D_\sigma(k+p)$$
$$((k+p)^2-m_\pi^2)(2p+q)_\mu(2p+q)_\nu\mathrm{FF}_\sigma[p,k]^2\Bigg]\Bigg|_{p_0=iw_n}$$
$$+(k\to-k), \tag{4.72}$$

$$\Gamma''^{(4)G\sigma}_{\mu\nu\,ab33}(k,q) = -2(\delta_{ab}-\delta_{3a}\delta_{3b})\frac{ig_\rho^2g_\sigma^2}{2}T\sum_{n(even)}\Bigg[\int\frac{d^3p}{(2\pi)^3}D_\pi(p)^2D_\sigma(k+p)$$
$$((k+p)^2-m_\pi^2)g_{\mu\nu}\mathrm{FF}_\sigma[p,k]^2\Bigg]\Bigg|_{p_0=iw_n}. \tag{4.73}$$

The total vertex corrections, including terms where the rho meson couples to a heavy pion propa-

gator, are then given by:

$$\begin{aligned}\tilde{\Gamma}'^{(3)}_{\mu\,ab3}(k,q) &= \Gamma''^{(3)\rho}_{\mu\,ab3}(k,q)+\Gamma''^{(3)\sigma}_{\mu\,ab3}(k,q)\\ &+g_\rho\epsilon_{3ab}(2k+q)_i\Big(\frac{\Sigma_{\pi(\rho)}(q+k)}{\Lambda^2_{\rho2}+\vec{k}^2}+\frac{\Sigma_{\pi(\rho)}(k)}{\Lambda^2_{\rho2}+(\vec{q}+\vec{k})^2}\Big)\\ &+g_\rho\epsilon_{3ab}(2k+q)_i\Big(\frac{\Sigma_{\pi(\sigma)}(q+k)}{\Lambda^2_{\sigma2}+\vec{k}^2}+\frac{\Sigma_{\pi(\sigma)}(k)}{\Lambda^2_{\sigma2}+(\vec{q}+\vec{k})^2}\Big),\end{aligned} \tag{4.74}$$

$$\begin{aligned}\tilde{\Gamma}'^{(4)}_{\mu\nu\,ab33}(k,q) &= \Gamma''^{(4)\rho}_{\mu\nu\,ab33}(k,q)+\Gamma''^{(4)\sigma}_{\mu\nu\,ab33}(k,q)-\frac{ig_\rho\epsilon_{3ca}}{\Lambda^2_{\rho2}+\vec{k}^2}\Big[(2k-q)_i\Gamma''^{(3)\rho}_{\nu\,bc3}(k,-q)\\ &+(2k+q)_j\Gamma''^{(3)\rho}_{\mu\,cb3}(-q-k,q)\Big]-\frac{ig_\rho\epsilon_{3ca}}{\Lambda^2_{\sigma2}+\vec{k}^2}\Big[(2k-q)_i\Gamma''^{(3)\sigma}_{\nu\,bc3}(k,-q)\\ &+(2k+q)_j\Gamma''^{(3)\sigma}_{\mu\,cb3}(-q-k,q)\Big]-\frac{ig_\rho\epsilon_{3bc}}{\Lambda^2_{\rho2}+\vec{k}^2}\Big[(2k+q)_i\Gamma''^{(3)\rho}_{\nu\,ac3}(-k,-q)\\ &+(2k-q)_j\Gamma''^{(3)\rho}_{\mu\,ca3}(-q+k,q)\Big]-\frac{ig_\rho\epsilon_{3bc}}{\Lambda^2_{\sigma2}+\vec{k}^2}\Big[(2k+q)_i\Gamma''^{(3)\sigma}_{\nu\,ac3}(-k,-q)\\ &+(2k-q)_j\Gamma''^{(3)\sigma}_{\mu\,ca3}(-q+k,q)\Big]\\ &-ig^2_\rho(\delta_{ab}-\delta_{3a}\delta_{3b})\Bigg\{(2k-q)_i(2k-q)_j\Bigg[\frac{\Sigma_{\pi(\rho)}(-q+k)}{(\Lambda^2_{\rho2}+\vec{k}^2)^2}\\ &+\frac{2\Sigma_{\pi(\rho)}(k)}{(\Lambda^2_{\rho2}+(-\vec{q}+\vec{k})^2)(\Lambda^2_{\rho2}+\vec{k}^2)}+\frac{\Sigma_{\pi(\sigma)}(-q+k)}{(\Lambda^2_{\sigma2}+\vec{k}^2)^2}\\ &+\frac{2\Sigma_{\pi(\sigma)}(k)}{(\Lambda^2_{\sigma2}+(-\vec{q}+\vec{k})^2)(\Lambda^2_{\sigma2}+\vec{k}^2)}\Bigg]+(2k+q)_i(2k+q)_j\Bigg[\frac{\Sigma_{\pi(\rho)}(q+k)}{(\Lambda^2_{\rho2}+\vec{k}^2)^2}\\ &+\frac{2\Sigma_{\pi(\rho)}(k)}{(\Lambda^2_{\rho2}+(\vec{q}+\vec{k})^2)(\Lambda^2_{\rho2}+\vec{k}^2)}+\frac{\Sigma_{\pi(\sigma)}(q+k)}{(\Lambda^2_{\sigma2}+\vec{k}^2)^2}+\frac{2\Sigma_{\pi(\sigma)}(k)}{(\Lambda^2_{\sigma2}+(\vec{q}+\vec{k})^2)(\Lambda^2_{\sigma2}+\vec{k}^2)}\Bigg]\\ &-4\delta_{ij}\frac{\Sigma_{\pi(\rho)}(k)}{\Lambda^2_{\rho2}+\vec{k}^2}-4\delta_{ij}\frac{\Sigma_{\pi(\sigma)}(k)}{\Lambda^2_{\sigma2}+\vec{k}^2}\Bigg\},\end{aligned} \tag{4.75}$$

where $\Gamma''^{(3)(\rho/\sigma)}$ and $\Gamma''^{(4)(\rho/\sigma)}$ are the regularized vertex corrections given in eqs. 4.64 through 4.73. Finally, we note that in chapter 5 we will assess the effect of the additional vertex corrections, induced by adding a form factor, on the rho self-energy as an additional measure of the violation of gauge invariance due to using the center of mass momentum.

4.5 Dressing intermediate particles

The vertex corrections contain intermediate rho, sigma, and pion propagators. As was seen with the Landau cut of $\Sigma_\rho^{\mu\nu}$, if these propagators are not dressed the conductivity will be infinite. We dress the rho and sigma propagators with the vacuum rho and sigma self-energies and treat the intermediate pion propagators self-consistently. However, thermal pions within vertex corrections and the pion self-energy are not dressed, allowing us to make use of the identitiy from eq. 2.41. The dressed pion, rho and sigma propagators are given by eqs. 1.18, 2.10, and 3.24, respectively. The widths in the pion and rho propagators violates gauge invariance. However, the violation due to dressing D_ρ only occurs in vertex corrections containing multiple rho propagators, and is thus suppressed by $\frac{1}{m_\rho^2}$. The violation due to dressing intermediate pion propagators within vertex corrections can be corrected by dressing the $\rho\pi\pi$ vertices that couple to an external ρ with three point-vertex corrections and dressing thermal pion propagators, creating a self-consistency equation. These effects are expected to be small, due to the small pion width, thus we will not calculate these corrections in this work.

4.6 Removing double counting

We must take care when calculating $\Sigma_\rho^{\mu\nu}$ to avoid double counting self-energy contributions. Double counting is encountered due to the self consistent treatment of the $\rho\pi\pi$ vertex and the pion propagator. For the corrections to the $\rho\pi\pi$ vertex double counting is encountered due to the presence of the Landua cut within vertex corrections, ie thermal $\pi\pi$-scattering with the external rho. Furthermore, double counting is generated in all the corrections to the $\rho\rho\pi\pi$ vertex.

For the corrections to the $\rho\pi\pi$ vertex, double counting occurs due to $\Gamma''^{(3)C\rho}_{\mu\,ab3}$ and $\Gamma''^{(3)C\sigma}_{\mu\,ab3}$. In figure 4.10 we demonstrate how these diagrams can generate double counting. Figure 4.10 displays the rho self-energy diagrams generated by dressing the left hand vertex in the rho self-energy with $\Gamma''^{(3)C\rho}_{\mu\,ab3}$ and the right hand vertex with the bare $\rho\pi\pi$ vertex, and vice versa. However, in figure 4.10 we replace the pions in the vertex correction with heavy pions. When heavy pions are used in the vertex correction the two diagrams are unique. However, if one replaces the heavy pions with

physical pions the diagrams become identical.

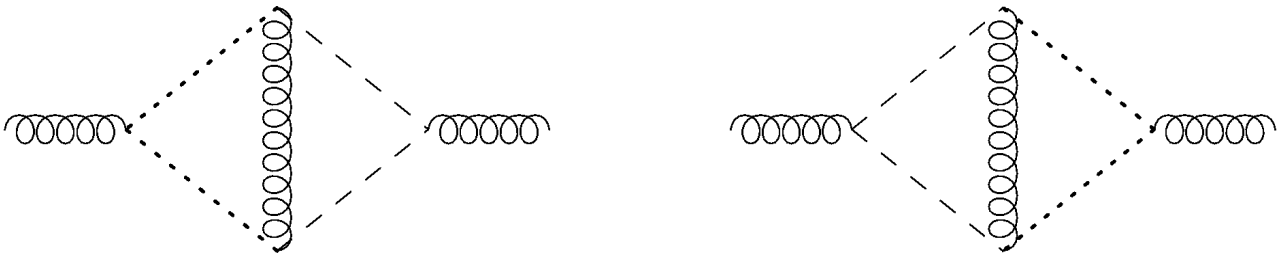

Figure 4.10: (Left/Right): Rho self-energy obtained by dressing the $\pi\pi$-loop with $\Gamma''^{(3)C\rho}_{\mu\,ab3}$ on the left/right hand $\rho\pi\pi$ vertex. The pion propagators within $\Gamma''^{(3)C\rho}_{\mu\,ab3}$ are replaced with heavy pions. One can see that the self-energies become identical when the heavy pions are replaced with physical pions.

Furthermore, consider the contribution to the rho self-energy obtained by dressing the left hand vertex in $\Sigma^{\mu\nu}_{\rho}$ with $\Gamma''^{(3)C\rho}_{\mu\,ab3}$ and the right hand vertex with $\Gamma''^{(3)A\rho}_{\mu\,ab3}$, as shown in figure 4.11. As figure 4.11 demonstrates, this diagram can also be obtained by dressing the right hand vertex in $\Sigma^{\mu\nu}_{\rho}$ with $\Gamma''^{(3)C\rho}_{\mu\,ab3}$ and considering the second order vertex correction where the $\rho\pi\pi$ vertex within $\Gamma''^{(3)C\rho}_{\mu\,ab3}$ is dressed with $\Gamma''^{(3)A\rho}_{\mu\,ab3}$. Similar arguments apply for all of the second order vertex corrections produced by dressing the $\rho\pi\pi$ vertices in $\Gamma''^{(3)C\rho}_{\mu\,ab3}$ and $\Gamma''^{(3)C\sigma}_{\mu\,ab3}$.

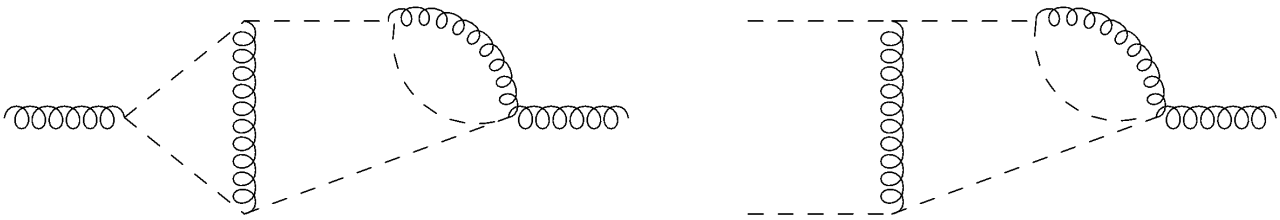

Figure 4.11: Left: Rho self-energy contribution generated by dressing the $\pi\pi$-loop's left $\rho\pi\pi$ vertex with $\Gamma''^{(3)C\rho}_{\mu\,ab3}$ and the right vertex with $\Gamma''^{(3)A\rho}_{\mu\,ab3}$. Right: Second order vertex correction produced by dressing $\Gamma''^{(3)C\rho}_{\mu\,ab3}$ with $\Gamma''^{(3)A\rho}_{\mu\,ab3}$. One sees that the first diagram can be produced by dressing the $\pi\pi$-loop's right hand vertex with the second order vertex correction.

This double counting is encountered because the thermal particles in the vertex corrections are identical to those in the rho self-energy. However, the vertex corrections are defined such that they do not include vacuum particles, therefore we only encounter double counting when dressing the Landau cut of $\Sigma^{\mu\nu}_{\rho}$. One can avoid encountering double counting in the $\pi\pi$-loop by only dressing the right hand $\rho\pi\pi$ vertex with the self consistently calculated $\Gamma''^{(3)C\rho}_{\mu\, ab3}$ or $\Gamma''^{(3)C\sigma}_{\mu\, ab3}$ vertex correction.

Next, we address double counting in the corrections to the $\rho\rho\pi\pi$ vertex. As was seen for the unitarity cut of the $\pi\pi$-loop, double counting is avoided when we dress the vacuum tad pole loop and its Bose enhancement. However, when the pion in the tad pole loop is thermal, all of the four-point corrections generate double counting.

There are two scenarios that generate double counting in the four-point vertex corrections: First, the rho self-energy contribution derived from the correction is equivalent to a previously calculated rho self-energy diagram. This occurs in $\Gamma''^{(4)B_1\rho}_{\mu\nu\, ab33}$, $\Gamma''^{(4)B_2\rho}_{\mu\nu\, ab33}$, $\Gamma''^{(4)E\rho}_{\mu\nu\, ab33}$, $\Gamma''^{(4)F_1\rho}_{\mu\nu\, ab33}$, $\Gamma''^{(4)F_2\rho}_{\mu\nu\, ab33}$, $\Gamma''^{(4)G\rho}_{\mu\nu\, ab33}$, $\Gamma''^{(4)E\sigma}_{\mu\nu\, ab33}$, and $\Gamma''^{(4)G\sigma}_{\mu\nu\, ab33}$. The self-energy contributions resulting from these vertex corrections are shown in figure 4.12.

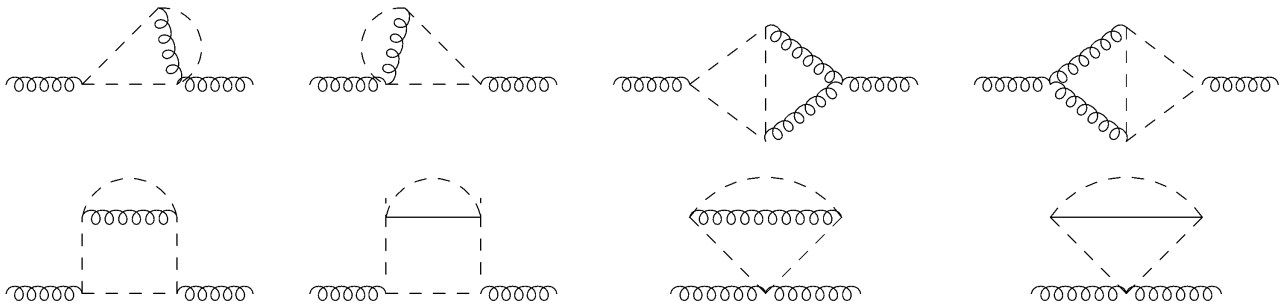

Figure 4.12: Rho self-energy diagrams generated by dressing the tap pole loop with vertex corrections. The above contributions are identical to previously encountered rho self-energy diagrams. From left to right the top row of diagrams are generated by $\Gamma''^{(4)B_1\rho}_{\mu\nu\, ab33}$, $\Gamma''^{(4)B_2\rho}_{\mu\nu\, ab33}$, $\Gamma''^{(4)F_1\rho}_{\mu\nu\, ab33}$ and, $\Gamma''^{(4)F_2\rho}_{\mu\nu\, ab33}$. From left to right the bottom row of diagrams are generated by $\Gamma''^{(4)E\rho}_{\mu\nu\, ab33}$, $\Gamma''^{(4)G\rho}_{\mu\nu\, ab33}$, $\Gamma''^{(4)E\sigma}_{\mu\nu\, ab33}$, and $\Gamma''^{(4)G\sigma}_{\mu\nu\, ab33}$.

One can see that $\Gamma''^{(4)B_1\rho}_{\mu\nu\, ab33}$, $\Gamma''^{(4)B_2\rho}_{\mu\nu\, ab33}$, $\Gamma''^{(4)F_1\rho}_{\mu\nu\, ab33}$, and $\Gamma''^{(4)F_2\rho}_{\mu\nu\, ab33}$ can be generated from the $\pi\pi$-loop using corrections to the $\rho\pi\pi$ vertex (specifically $\Gamma''^{(3)A\rho}_{\mu\, ab3}$ and $\Gamma''^{(3)D\rho}_{\mu\, ab3}$). Alternatively, $\Gamma''^{(4)E\rho}_{\mu\nu\, ab33}$, $\Gamma''^{(4)G\rho}_{\mu\nu\, ab33}$,

$\Gamma''^{(4)E\sigma}_{\mu\nu\,ab33}$, and $\Gamma''^{(4)G\sigma}_{\mu\nu\,ab33}$ simply dress a pion propagator in $\Sigma^{\mu\nu}_{\rho}$ with a thermal $\pi\rho$ or $\pi\sigma$ loop. However, these diagrams where already included by resumming the pion propagators with $\Sigma^{\mu\nu}_{\pi}$.

In the second scenario a unique diagram is generated by the vertex corrections, however the diagram includes a $\pi\pi$-loop in which the two pions have identical 4-momentum. This configuration generates double counting, because the pions are indistinguishable. Therefore, an additional symmetry factor of $\frac{1}{2}$ is added when the tad pole loop contains a thermal pion. This scenario occurs in $\Gamma''^{(4)A\rho}_{\mu\nu\,ab33}$, $\Gamma''^{(4)C_1\rho}_{\mu\nu\,ab33}$, $\Gamma''^{(4)C_2\rho}_{\mu\nu\,ab33}$, $\Gamma''^{(4)D\rho}_{\mu\nu\,ab33}$, and $\Gamma''^{(4)H\rho}_{\mu\nu\,ab33}$, the resulting rho self-energy contributions are shown in figure 4.13.

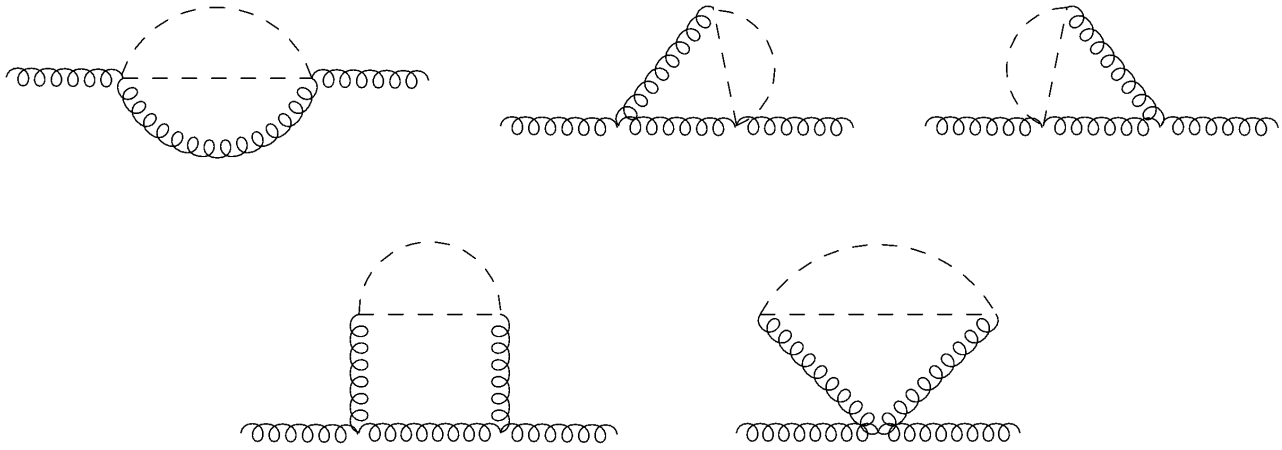

Figure 4.13: Rho self-energy diagrams generated by dressing the tap pole loop with vertex corrections. The above contributions produce double counting due to the presence of $\pi\pi$-loops involving pions with identical 4-momentum. From left to right the top row of diagrams are generated by $\Gamma''^{(4)A\rho}_{\mu\nu\,ab33}$, $\Gamma''^{(4)C_1\rho}_{\mu\nu\,ab33}$, and $\Gamma''^{(4)C_2\rho}_{\mu\nu\,ab33}$. From left to right the bottom row of diagrams are generated by $\Gamma''^{(4)D\rho}_{\mu\nu\,ab33}$ and $\Gamma''^{(4)H\rho}_{\mu\nu\,ab33}$.

Finally, we show that the rho self-energy will remain gauge invariant if all double counting is removed. Figures 4.14 and 4.15 show the rho self-energy diagrams generated when $\Sigma^{\mu\nu}_{\rho}$'s vertices are full dressed, with D_π and the $\rho\pi\pi$ vertex handled self consistently.

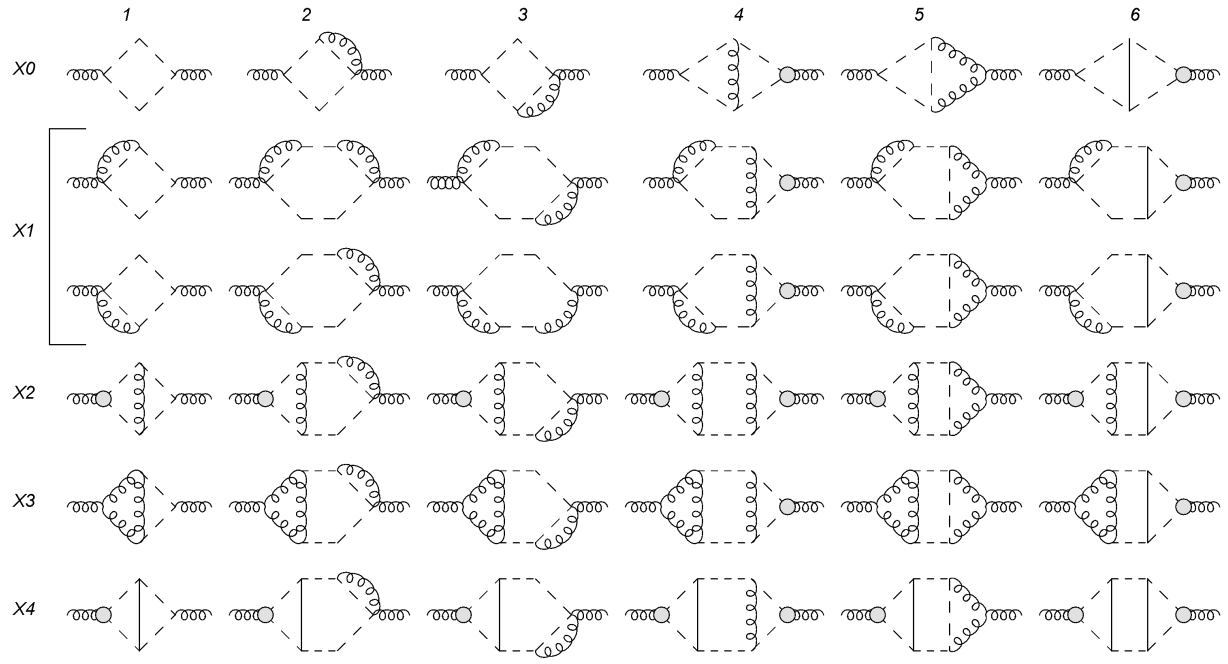

Figure 4.14: Self-energies resulting from dressing the $\pi\pi$-loop with three-point vertex corrections. Rows labeled X0 through X4 correspond to gauge invariant subgroups when combined with the corresponding row in figure 4.15. Gray bubbles represent the dressing of a $\rho\pi\pi$ vertex with three-point vertex corrections.

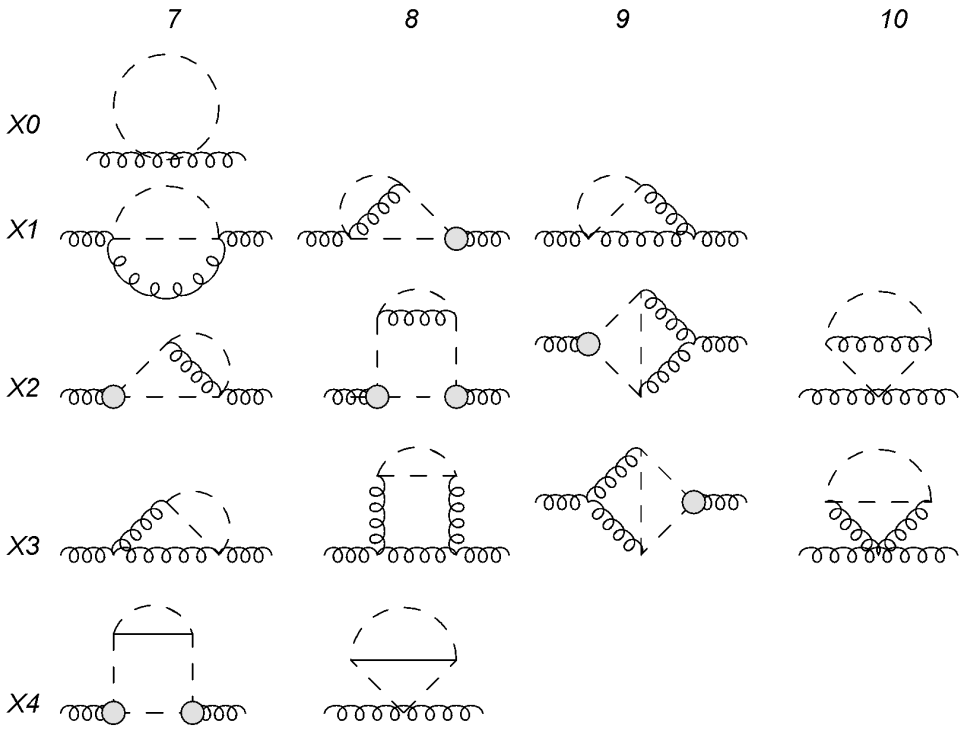

Figure 4.15: Self-energies resulting from dressing the tadpole loop with vertex corrections. Rows labeled X0 through X1 correspond to gauge invariant subgroups when combined with the corresponding row in figure 4.14. Gray bubbles represent the dressing of a $\rho\pi\pi$ vertex with three-point vertex corrections.

The figures show the first order vertex corrections, while higher order corrections are represented with gray bubbles. The self-energies are organized into groups which are 4-dimensionally transverse, so that each group is independently gauge invariant. These sub groups correspond to the sub groups established in section 4.2.1 that were used to show the satisfaction of the Ward identities. Let us consider the Landau cut of the rho self-energy, where double counting is encountered. We have shown that the diagrams in sub groups X2 and X4 must all be removed to avoid double counting. However, because X2 and X4 are independently transverse their removal does not break gauge invariance.

Next we consider sub group X1. We have established that diagrams (X1,7) and (X1,9) require an additional symmetry factor of $\frac{1}{2}$. Furthermore, when the gray bubble in diagram (X1,8) is expanded, one can reproduce all X1 diagrams in fig. 4.14. Therefore, one can avoid double

counting by adding a factor of $\frac{1}{2}$ to all diagrams in sub group X1, which does not violate gauge invariance. Sub group X3 produces a similar scenario. Diagrams (X3,7), (X3,8), and (X3,10) require an additional symmetry factor, while diagram (X3,9) can reproduce all diagrams in figure 4.14 belonging to sub group X3. Therefore, one can again avoid double counting by adding a factor of $\frac{1}{2}$ to the entire subgroup. Therefore, all double counting can be removed from the Landau cut without violating gauge invariance. Finally, we note that we have omitted the additional vertex corrections, generated by adding form factors from figures 4.14 and 4.15. This was done for simplicity, and because these corrections do not produce double counting.

In this work we only calculate first order vertex corrections. Thus, we will not dress the $\rho\pi\pi$ vertices within vertex corrections. Therefore, in our final calculations we are not required to drop diagrams (X2,2) through (X2,6) to avoid double counting, because the second order vertex corrections are not explicitly included.

4.7 Transverse projection of the rho self-energy

In this section we calculate the transverse projection of $\Sigma_\rho^{\mu\nu}$ for arbitrary $\rho\pi\pi$ and $\rho\rho\pi\pi$ vertices, $\Gamma^{(3)}_{\mu\,ab3}(k,q)$ and $\Gamma^{(4)}_{\mu\nu\,ab33}(k,q)$, at $\vec{q}=0$. The results are then used to calculate the transverse projection of $\Sigma_\rho^{\mu\nu}$ for dressed vertices.

To begin, we calculate:

$$\lim_{\vec{q}\to 0}\frac{1}{2}P_T^{\mu\nu}\Gamma^{(3)}_{\mu\,ab3}(k,q)\Gamma^{(3)}_{\nu\,ba3}(q+k,-q), \tag{4.76}$$

which appears in $\Sigma_\rho^{\mu\nu}$'s $\pi\pi$-loop. $\Gamma^{(3)}_{\mu\,ab3}(k,q)$ is a Lorentz vector, and thus must be proportional to the 4-momenta we have introduced in the calculation, p_μ, k_μ, and q_μ. However, we have integrated over p, therefore we can express $\Gamma^{(3)}_{\mu\,ab3}(k,q)$ in terms of only the 4-momenta external to the vertex (k_μ, and q_μ):

$$\Gamma^{(3)}_{\mu\,ab3}(k,q)=k_\mu\Gamma^{(3)}_{k\,ab3}(k,q)+q_\mu\Gamma^{(3)}_{q\,ab3}(k,q), \tag{4.77}$$

where $\Gamma^{(3)}_{k\,ab3}$ and $\Gamma^{(3)}_{q\,ab3}$ can be determined in terms of $\Gamma^{(3)}_{\mu\,ab3}$ by contracting eq. 4.77 with k_μ and q_μ. The projection in eq. 4.76 can now be written as:

$$\begin{aligned}
&\lim_{\vec{q}\to 0}\frac{1}{2}P_T^{\mu\nu}\Gamma^{(3)}_{\mu\,ab3}(k,q)\Gamma^{(3)}_{\nu\,ba3}(q+k,-q)\\
=\;&\lim_{\vec{q}\to 0}\frac{1}{2}\Big(\vec{k}^2\Gamma^{(3)}_{k\,ab3}(k,q)\Gamma^{(3)}_{k\,ba3}(q+k,-q)+\vec{k}\cdot\vec{q}\,\Gamma^{(3)}_{k\,ab3}(k,q)\Gamma^{(3)}_{q\,ba3}(q+k,-q)+\\
&\vec{k}\cdot\vec{q}\,\Gamma^{(3)}_{q\,ab3}(k,q)\Gamma^{(3)}_{k\,ba3}(q+k,-q)+\vec{q}^2\Gamma^{(3)}_{q\,ab3}(k,q)\Gamma^{(3)}_{q\,ba3}(q+k,-q)\\
&-\frac{1}{\vec{q}^2}\Big[(\vec{k}\cdot\vec{q})^2\Gamma^{(3)}_{k\,ab3}(k,q)\Gamma^{(3)}_{k\,ba3}(q+k,-q)+(\vec{k}\cdot\vec{q})\vec{q}^2\,\Gamma^{(3)}_{k\,ab3}(k,q)\Gamma^{(3)}_{q\,ba3}(q+k,-q)\\
&+(\vec{k}\cdot\vec{q})\vec{q}^2\,\Gamma^{(3)}_{q\,ab3}(k,q)\Gamma^{(3)}_{k\,ba3}(q+k,-q)+\vec{q}^4\,\Gamma^{(3)}_{q\,ab3}(k,q)\Gamma^{(3)}_{q\,ba3}(q+k,-q)\Big]\Big)\\
=\;&\frac{\vec{k}^2}{2}\Big(1-\cos(\theta)^2\Big)\Gamma^{(3)}_{k\,ab3}(k,q)\Gamma^{(3)}_{k\,ba3}(q+k,-q)\big|_{\vec{q}=0},
\end{aligned}\tag{4.78}$$

where $\cos(\theta)$ is the angle between $\vec{k}$ and $\vec{q}$. We are free to align the z-axis with $\vec{q}$, so that $\cos(\theta)$ is also the angle between $\vec{k}$ and the z-axis. One can determine $\Gamma^{(3)}_{k\,ab3}$ by contracting the left and right hand sides of equation 4.77 with k_i:

$$\Gamma^{(3)}_{k\,ab3}=\frac{k_i\Gamma^{(3)}_{i\,ab3}}{\vec{k}^2}-\frac{k_iq_i\Gamma^{(3)}_{q\,ab}}{\vec{k}^2}.\tag{4.79}$$

At zero-momentum one finds:

$$\Gamma^{(3)}_{k\,ab}=\frac{k_i\Gamma^{(3)}_{i\,ab3}}{\vec{k}^2}=\frac{\Gamma^{(3)}_{3\,ab3}}{|\vec{k}|},\tag{4.80}$$

where we have evaluated $k_i\Gamma^{(3)}_{i\,ab3}$ in the frame where $\vec{k}$ is aligned with the z-axis. One can use eq. 4.80 and 4.76 to show:

$$\frac{1}{2}P_T^{\mu\nu}\Gamma^{(3)}_{\mu\,ab3}\Gamma^{(3)}_{\nu\,ab3}\;=\;\frac{1}{2}(1-\cos(\theta)^2)\Gamma^{(3)}_{3\,ab3}(k,q)\Gamma^{(3)}_{3\,ab3}(q+k,-q)\big|_{\vec{q}}.\tag{4.81}$$

Next we calculate the transverse projection of an arbitrary $\rho\rho\pi\pi$ vertex. As was seen for $\Gamma^{(3)}_{\mu\,ab3}$, $\Gamma^{(4)}_{\mu\nu\,ab33}$ can be expressed in terms of combinations of the external 4-momenta k_μ and q_μ. However,

because $\Gamma^{(4)}_{\mu\nu\,ab33}$ is a tensor it can also include terms proportional to $g_{\mu\nu}$, as was the case for the vacuum $\rho\rho\pi\pi$ vertex. Thus we rewrite $\Gamma^{(4)}_{\mu\nu\,ab33}$ as:

$$\Gamma^{(4)}_{\mu\nu\,ab33}(k,q) = g_{\mu\nu}\Gamma^{(4)}_{1\,ab33}(k,q) + k_\mu k_\nu \Gamma^{(4)}_{2\,ab33}(k,q) + q_\mu k_\nu \Gamma^{(4)}_{3\,ab33}(k,q) + q_\mu q_\nu \Gamma^{(4)}_{4\,ab33}(k,q). \tag{4.82}$$

The transverse projection of $\Gamma^{(4)}_{\mu\nu\,ab33}$ at zero-momentum is given by:

$$\begin{aligned}
&\lim_{\vec{q}\to 0} \frac{1}{2} P_T^{\mu\nu} \Gamma^{(4)}_{\mu\nu\,ab33}(k,q) \\
=\ &\lim_{\vec{q}\to 0} \frac{1}{2}\Big[-3\Gamma^{(4)}_{1\,ab33}(k,q) + \vec{k}^2\Gamma^{(4)}_{2\,ab33}(k,q) + \vec{k}\cdot\vec{q}\,\Gamma^{(4)}_{3\,ab33}(k,q) + \vec{q}^{\,2}\,\Gamma^{(4)}_{4\,ab33}(k,q) \\
&\frac{1}{\vec{q}^2}\Big(\vec{q}^{\,2}\Gamma^{(4)}_{1\,ab33}(k,q) - (\vec{k}\cdot\vec{q})^2\Gamma^{(4)}_{2\,ab33}(k,q) - (\vec{k}\cdot\vec{q})\vec{q}^{\,2}\,\Gamma^{(4)}_{3\,ab33}(k,q) - \vec{q}^{\,4}\Gamma^{(4)}_{4\,ab33}(k,q)\Big)\Big] \\
=\ &\lim_{\vec{q}\to 0} \frac{1}{2}\Big(-2\Gamma^{(4)}_{1\,ab33}(k,q) + (1-\cos(\theta)^2)\vec{k}^2\Gamma^{(4)}_{2\,ab33}(k,q)\Big)\big|_{\vec{q}=0}.
\end{aligned} \tag{4.83}$$

One can calculate $\Gamma^{(4)}_{1\,ab33}$ and $\Gamma^{(4)}_{2\,ab33}$ by contracting eq. 4.82 with $k_i k_j$ and δ_{ij} at $\vec{q}=0$:

$$k_i k_j \Gamma^{(4)}_{ij\,ab33}(k,q)\big|_{\vec{q}=0} = -\vec{k}^2\Gamma^{(4)}_{1\,ab33}(k,q) + \vec{k}^4\Gamma^{(4)}_{2\,ab33}(k,q)\big|_{\vec{q}=0}, \tag{4.84}$$

$$\delta_{ij}\Gamma^{(4)}_{ij\,ab33}(k,q)\big|_{\vec{q}=0} = -3\Gamma^{(4)}_{1\,ab33}(k,q) + \vec{k}^2\Gamma^{(4)}_{2\,ab33}(k,q)\big|_{\vec{q}=0}. \tag{4.85}$$

The above system of equations can be solve to obtain:

$$\Gamma^{(4)}_{1\,ab33}(k,q)\big|_{\vec{q}=0} = -\frac{\Gamma^{(4)}_{ii\,ab33}(k,q)}{2} + \frac{k_i k_j \Gamma^{(4)}_{ij\,aa33}(k,q)}{2\vec{k}^2}\big|_{\vec{q}=0}, \tag{4.86}$$

$$\Gamma^{(4)}_{2\,ab33}(k,q)\big|_{\vec{q}=0} = \frac{-\Gamma^{(4)}_{ii\,ab33}(k,q)}{2\vec{k}^2} + \frac{3k_i k_j \Gamma^{(4)}_{ij\,ab33}(k,q)}{2\vec{k}^4}\big|_{\vec{q}=0}. \tag{4.87}$$

After inserting eqs. 4.86 and 4.87 into eq. 4.83 one finds:

$$\lim_{\vec{q}\to 0}\frac{1}{2}P_T^{\mu\nu}\Gamma^{(4)}_{\mu\nu\, aa33}(k,q)=\frac{1}{4}\Big((1+\cos(\theta)^2)\Gamma^{(4)}_{ii\, ab33}(k,q)+(1-3\cos(\theta)^2)\frac{k_ik_j\Gamma^{(4)}_{ij\, ab33}(k,q)}{\vec{k}^2}\Big)\Big|_{\vec{q}=0}. \tag{4.88}$$

The second term will vanish after performing the angular integrations in $\Sigma_\rho^{\mu\nu}$. Thus, we can write the transverse projection of the rho self-energy in terms of only $\Gamma^{(3)}_{\mu\, ab3}$ and $\Gamma^{(4)}_{iiab33}$:

$$\begin{aligned}\frac{1}{2}\rho_{T\,\mu\nu}\Sigma_\rho^{\mu\nu}(q_0,\vec{q}=0) &= \frac{2\pi}{3}T\sum_{n(even)}\int\frac{d|\vec{k}|\vec{k}^2}{(2\pi)^3}\Big[D_\pi(k)D_\pi(q+k)\big(g_\rho\epsilon_{3ab}(2|\vec{k}|)+\Gamma'^{(3)}_{3\,ab3}(k,q)\big)\\ &\quad \big(g_\rho\epsilon_{3ba}(2|\vec{k}|)+\Gamma'^{(3)}_{3\,ba3}(k+q,-q)\big)\Big]_{k_0=i\omega_n}\\ &\quad +\frac{1}{2}\frac{4\pi}{3}T\sum_{n(even)}\int\frac{d|\vec{k}|\vec{k}^2}{(2\pi)^3}\Big[D_\pi(k)\big(g_\rho^2\frac{-3}{\pi}-i\Gamma'^{(4)}_{ii\, aa33}(k,q)\big)\Big]_{k_0=i\omega_n},\end{aligned} \tag{4.89}$$

where we have performed the angular integrations analytically. The vertex corrections introduce nontrivial energy dependence into the vertices. Furthermore, the vertex corrections are complex, and must be written with a spectral representation, before the Matsubara sums are performed. In the appendix we establish the relevant spectral representations and calculate the Matsubara summations in eq. 4.89.

5. ELECTROMAGNETIC SPECTRAL FUNCTION IN PION MATTER

In this chapter we analyze the the EM-spectral function in hot pion matter and extract the conductivity. In section 5.1 we calculate Σ_ρ^T when pion propagators are dressed with Σ_π, but do not include vertex corrections. In section 5.2 we analyze the EM-spectral function without vertex corrections. The conductivity over temperature, without vertex corrections, is plotted and analyzed in section 5.3. We introduce vertex corrections to the rho self-energy in sections 5.4. Finally, we present the EM-spectral function with vertex corrections in section 5.5, and extract the conductivity over temperature in section 5.6.

5.1 Rho self-energy without vertex corrections

Figures 5.1 and 5.2 display the imaginary and real parts of the transverse projection of the rho self-energy for various temperatures, at $\vec{q} = 0$. The pion propagators within Σ_ρ^T are dressed with Σ_π. The medium effects on $\mathrm{Re}\Sigma_\rho^T$ are repulsive, causing the rho mass to increase. $\mathrm{Im}\Sigma_\rho^T$ increases with temperature for all q_0, but the increase is especially pronounced in the low energy regime. In vacuum, $\mathrm{Im}\Sigma_\rho^T$ is zero below $2m_\pi$, but at finite temperature a bump develops at low energy, which corresponds to the transport peak in Π_{EM}.

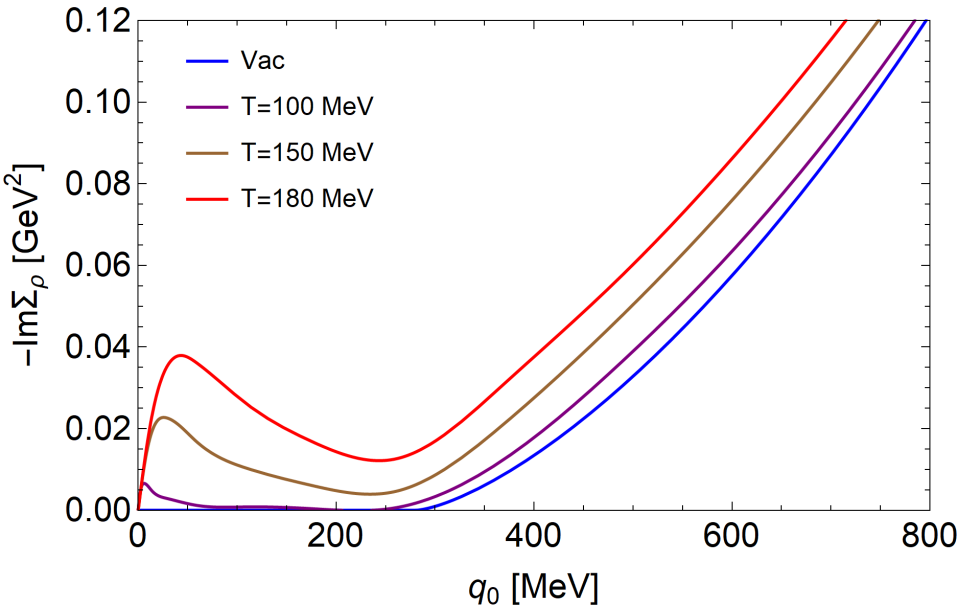

Figure 5.1: Imaginary part of the transverse projection of the rho self-energy in vacuum (blue), at T=100 MeV (purple), T=150 MeV (brown), and T=180 MeV (red), plotted as a function of energy at $\vec{q} = 0$.

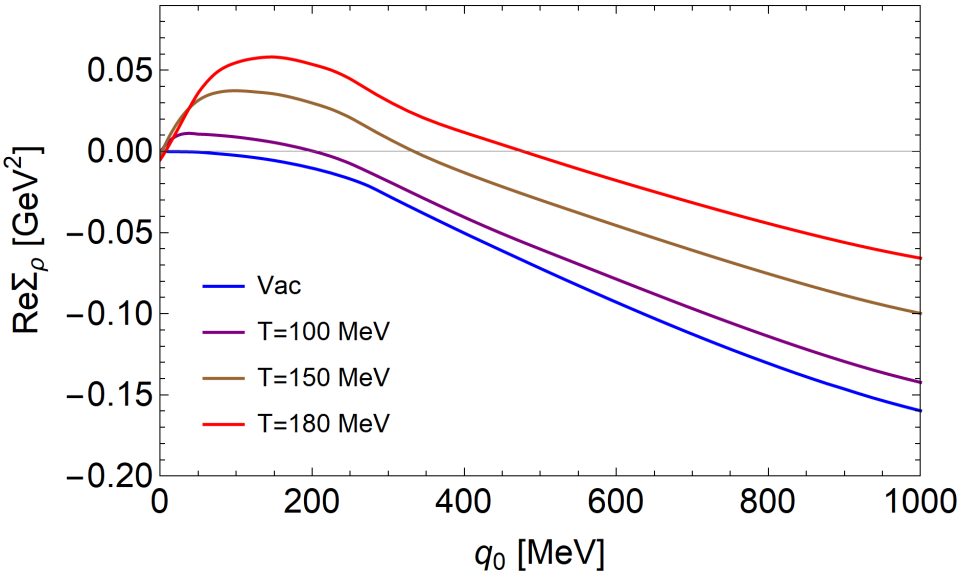

Figure 5.2: Real part of the transverse projection of the rho self-energy in vacuum (blue), at T=100 MeV (purple), T=150 MeV (brown), and T=180 MeV (red), plotted as a function of energy at $\vec{q} = 0$.

Figure 5.3 plots the Landau and unitarity cuts of Σ_ρ^T separately. Though the unitary cut can penetrate below the $2m_\pi$ threshold, due to the finite pion width, it is essentially zero below 220 MeV. While not a true threshold, the unitarity cut appears negligible compared to the Landau cut, which provides a large increase at low q_0.

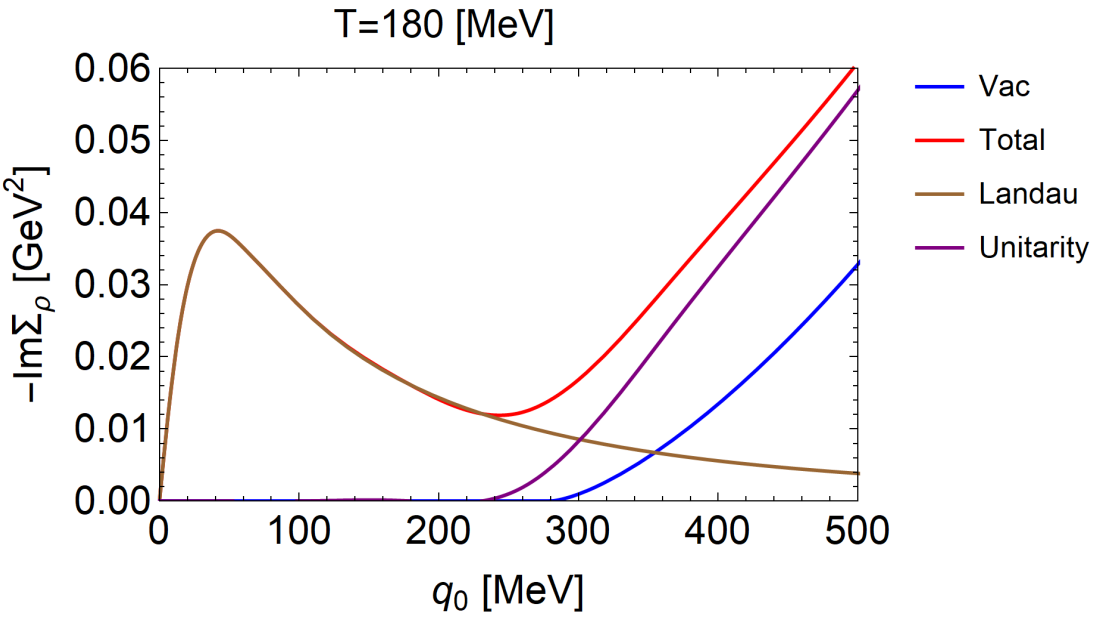

Figure 5.3: Imaginary part of the transverse projection of the rho self-energy as a function of energy at $\vec{q} = 0$ for T=180 MeV. The Landau (brown) and unitarity (purple) cuts are plotted separately, as well as the total (red) and the vacuum (blue). We see the low energy behavior is dominated by the Landau cut.

5.2 EM spectral function without vertex corrections

In this section we calculate the EM spectral function without vertex corrections. In figure 5.4 we plot $\Pi^{ii}_{\rm EM}/q_0$ for various temperatures, scaled such that the conductivity corresponds to the intercept at zero energy. At high energy, the rho's width and mass increase due to an increase in Σ_ρ^T. While the the rho's width is expected to increase with temperature, the repulsive shift of m_ρ is due in part to the fact that our calculation is not chirally symmetric. We do not attempt the preserve chiral symmetry in the present analysis, since doing so while also maintaining gauge invariance is

beyond the scope of this work.

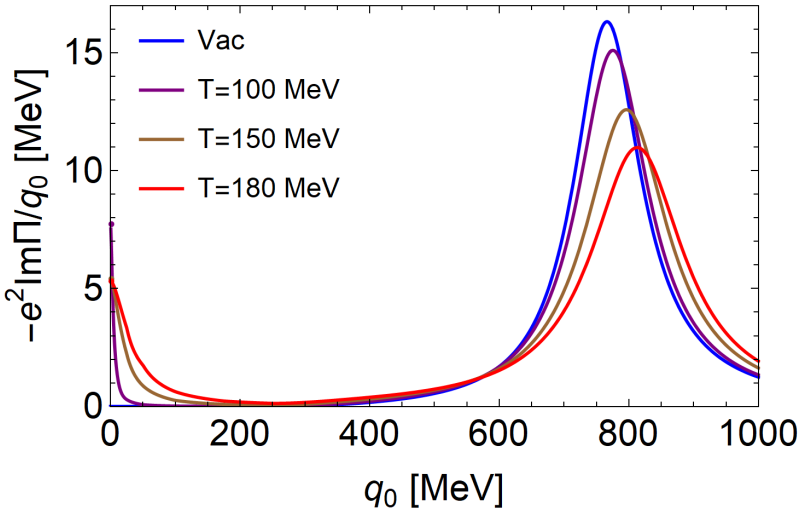

Figure 5.4: Imaginary part of the electromagnetic spectral function, scaled such that the zero-energy intercept corresponds to σ_{el}, plotted as a function of energy at $\vec{q} = 0$, for; vacuum (blue), at T=100 MeV (purple), T=150 MeV (brown), and T=180 MeV (red). For finite temperature a transport peak develops at low energy. Additionally, we see the rho's width and mass increase with temperature.

Figure 5.5 shows the scaled EM spectral function focusing on low energies. The transport peak broadens as temperature increases, because Σ_π increases with temperature. This is similar to the Lorentzian-like structure found in ref. [35] that broadened with increasing coupling. At the same time the conductivity decreases significantly when going from 100 MeV to 150 MeV, but increases slightly between 150 MeV and 180 MeV. This demonstrates that a minimum can develop in the conductivity, caused by a misalignment of thermal pion energies with that of the resonant particles towards higher temperatures.

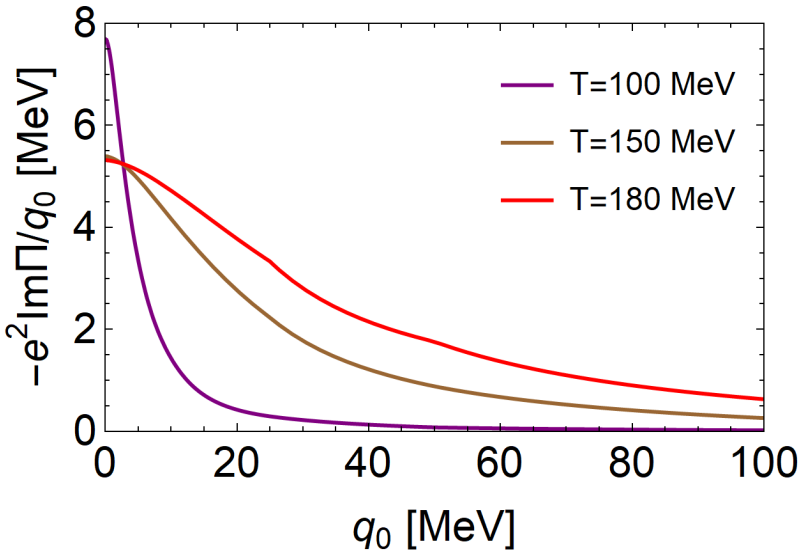

Figure 5.5: Imaginary part of the electromagnetic correlator, scaled such that the zero-energy intercept corresponds to σ_{el}, plotted as a function of energy at $\vec{q} = 0$, for: T=100 MeV (purple), T=150 MeV (brown), and T=180 MeV (red). We focus on the low energy region, emphasizing the transport peak. The peak broadens as the interaction strength increases with temperature.

Finally, figures 5.6 and 5.7 plot the EM spectral function when only S-wave (sigma resonance) or P-wave (rho resonance) scattering are considered, as well as the result when scattering is allowed through both channels. From figure 5.6, one can see that the three scenarios have little impact on the rho pole, where the unitarity cut dominates. The broadening of the rho pole is primarily due to the addition of Bose enhancement terms $(1 + f(\omega_k) + f(q_0 + \omega_k))$ in the rho self-energy, with the relatively small pion width causing only slight broadening. Additionally, we note that the broadening is augmented due to the increase in the P-wave phase space of the vacuum self-energy, caused by the shift in the rho mass. Conversely, figure 5.7 indicates that both resonances have significant impact on the low energy behavior of the spectral function, where the Landau cut dominates. This is expected because $\lim_{q_0 \to 0} \Pi^{ii}_{\mathrm{EM}}(q_0, 0)/q_0$ is approximately proportional to $\frac{1}{\Sigma_\pi}$, and is particularly sensitive to Σ_π's low momentum behavior, as will be shown in section 5.3.

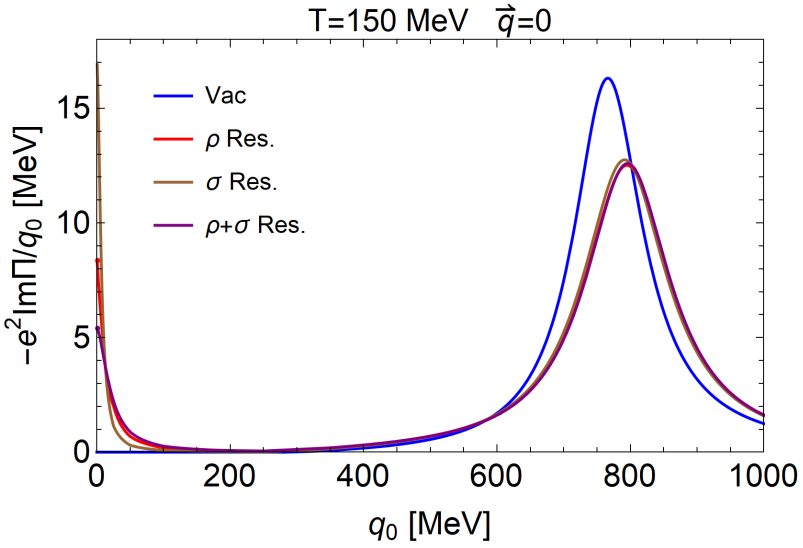

Figure 5.6: Imaginary part of the electromagnetic correlator, scaled such that the zero-energy intercept corresponds to σ_{el}, plotted as a function of energy at $\vec{q} = 0$ and T=150 MeV. The vacuum is plotted in blue, results for only P-wave scattering are plotted in red, results for only S-wave scattering are plotted in brown, and results allowing P- and S-wave scattering are plotted in purple. The energy range is chosen to emphasize the rho pole.

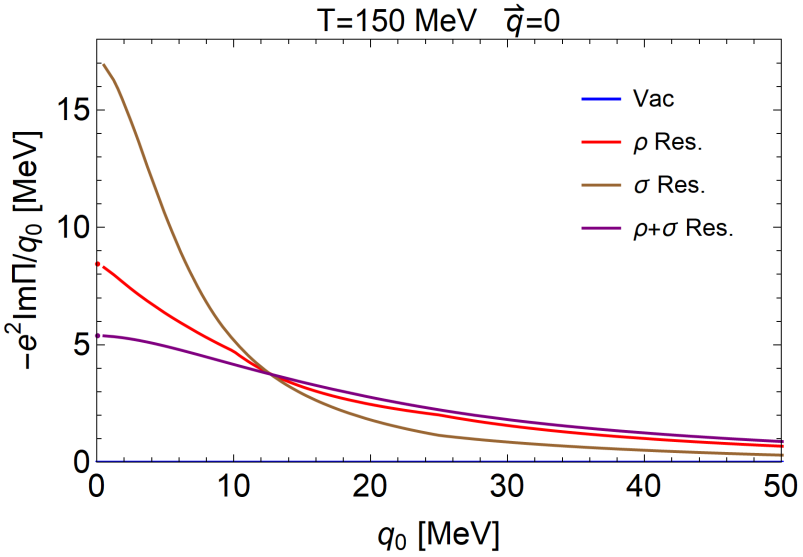

Figure 5.7: Imaginary part of the electromagnetic correlator, scaled such that the zero-energy intercept corresponds to σ_{el}, plotted as a function of energy at $\vec{q} = 0$ and T=150 MeV. The vacuum is plotted in blue, results for only P-wave scattering are plotted in red, results for only S-wave scattering are plotted in brown, and results allowing P- and S-wave scattering are plotted in purple. The energy range is chosen to emphasize the transport peak

5.3 σ/T without vertex corrections

Figure 5.8 displays our results for the conductivity divided by temperature without vertex corrections, as a function of temperature. The conductivity over temperature decreases as a function of temperature, but may develop a minimum beyond 180 MeV. We also plot the results when considering only S-wave (sigma resonance) or P-wave (rho resonance) scattering. For high temperatures the rho resonance generates a significantly smaller conductivity than the sigma. Since the conductivity is inversely related to resistance the conductivity adds roughly inversely. Thus the smallest individual contribution will exert greater influence on the total conductivity. P-wave scattering provides the greater influence at higher temperatures, however the S-wave is more influential below temperatures of approximately 110MeV. This hierarchy develops because $\Sigma_{\pi(\sigma)}$ dominates the pion self-energy at low momentum, while $\Sigma_{\pi(\rho)}$ dominates at large momentum, as the rho's mass (770 MeV) is larger than the sigma's (500 MeV). Transport coefficients are inherently low-energy phenomena, however as temperature increases our calculation probes higher momentum. Therefore, we see a crossing between ρ- and σ-contributions in figure 5.8 as we probe higher pion momenta.

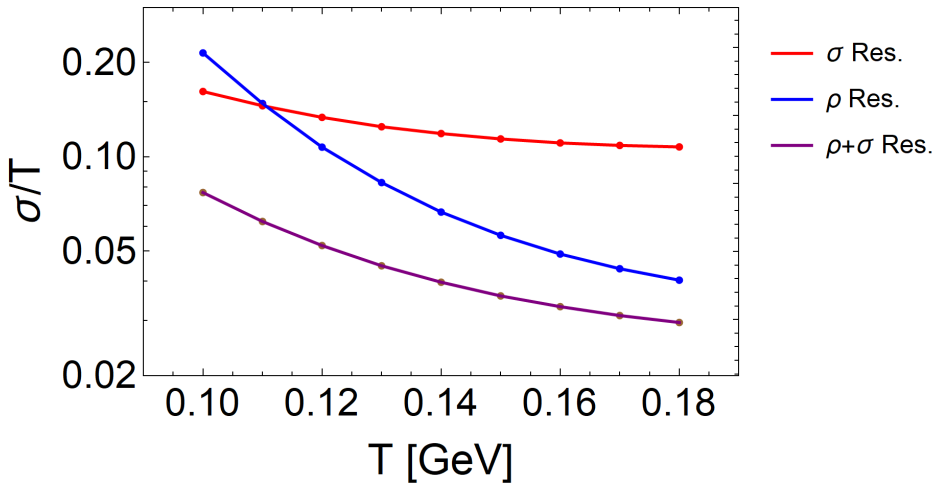

Figure 5.8: Electric conductivity divided by temperature as a function of temperature. The red curve shows the result if one only allows $\pi\pi$-scattering through a sigma resonance, the blue only allows $\pi\pi$-scattering through a rho resonance, and the purple allows scattering through both resonances.

We also compare our full off-shell result to the on-shell approximation from eq. 2.46. This is done by evaluating Γ_π with $\Sigma_\pi\left(\omega_k, \vec{k}\right)/\omega_k$ in eq. 2.46. Figure 5.9 compares the two calculations. Our results show that the approximation works fairly well, but becomes progressively worse as the interaction rate $\left(\frac{\mathrm{Im}\Sigma_\pi}{\omega_k}\right)$ increases with temperature. This suggests that the off-shell effects will become important in the strong-coupling limit.

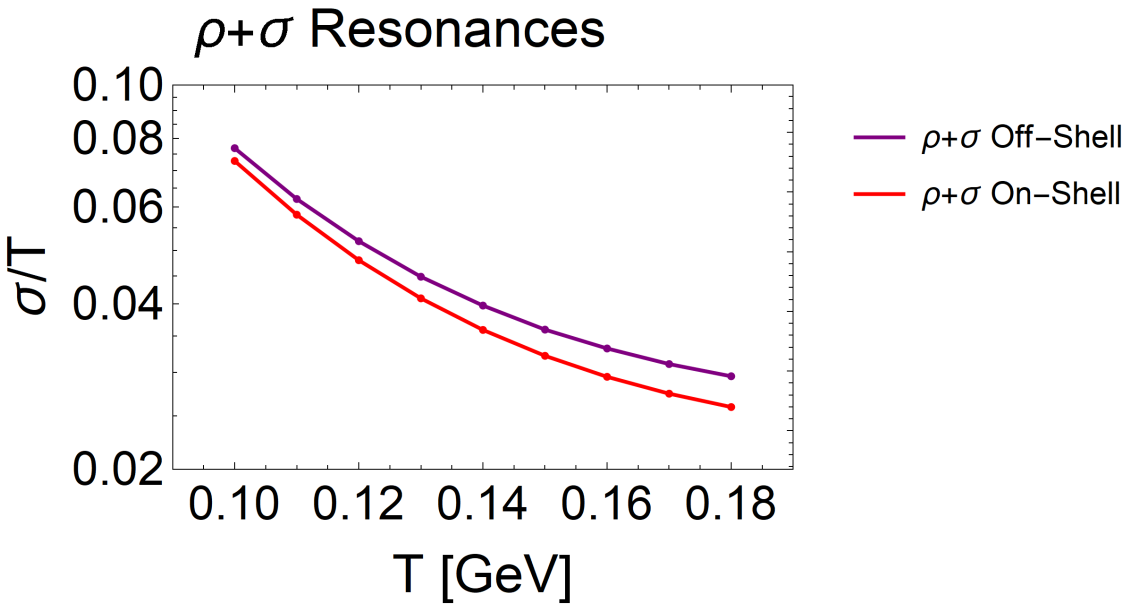

Figure 5.9: Electric conductivity divided by temperature as a function of temperature. We compare the full off-shell calculation (purple) to the on-shell approximation from 2.46 (red).

One can analyze how different pion momenta contribute to the conductivity by plotting the $\vec{k}$ integrand in $\lim_{q_0\to 0}\Sigma_\rho(q_0, \vec{q}=0)/q_0$. This integrand is given by:

$$\mathrm{K}_\sigma(|\vec{k}|, T) \quad = \quad \frac{4\pi g_\rho^2}{3(2\pi)^3} 4\vec{k}^4 \int_0^\infty \frac{dv}{-\pi} \mathrm{Im}[D_\pi(v, \vec{k})]^2 \frac{e^{\frac{v}{T}}}{T(-1+e^{\frac{v}{T}})^2}, \tag{5.1}$$

where the $q_0 \to 0$ limit has been performed analytically. Figures 5.10 and 5.11 show $\mathrm{K}_\sigma(|\vec{k}|, T)$ as a function of momentum at various temperatures when only rho or sigma $\pi\pi$-resonant scattering is considered. The rho's contribution peaks below 150 MeV, while the sigma peaks above 200 MeV.

In both cases, the peak shifts to higher $\vec{k}$ and broadens with temperature. These peaks represent the momenta most preferable for conducting charge, and are determined by the interplay of the pion self-energy and the density. For example, the rho's peak at T=100 MeV is remarkably large, relative to other temperatures, because at $T = 100\,\text{MeV}$ is it difficult to find thermal pions with enough energy to form a rho resonance, ie. $\Sigma_{\pi(\rho)}$ is small. Consequently, the pions interact quite weakly and $\text{K}_\sigma(|\vec{k}|, T)$ rises sharply. At higher momentum the P-wave interaction becomes favorable, thus $\text{K}_\sigma(|\vec{k}|, T)$ is suppressed. Alternatively, the sigma resonance is quite broad, facilitating scattering for low energy pions, where $\Sigma_{\pi(\rho)}$ is large. Therefore, in figure 5.11 K_σ is small for low momenta, where S-wave scattering dominates. As $\vec{k}$ increases $\Sigma_{\pi(\sigma)}$ decreases, resulting in a rise in K_σ, until it is eventually diminished due to thermal suppression of high energy pions.

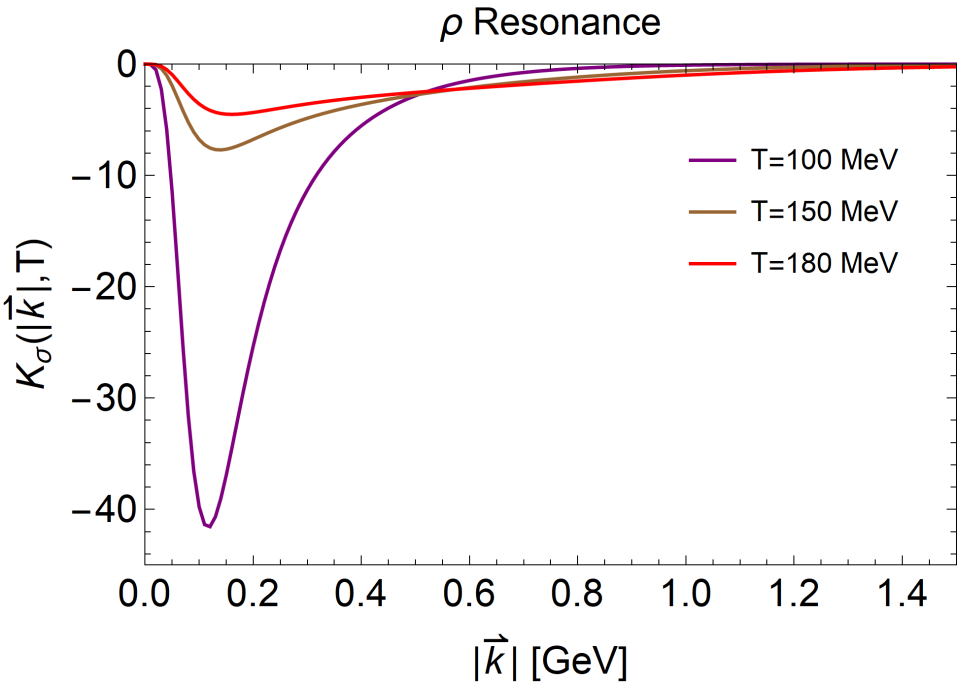

Figure 5.10: $\text{K}_\sigma(|\vec{k}|, T)$ as a function of momentum for T=100 MeV (purple), T=150 MeV (brown), and T=180 MeV (red). The integral of $\text{K}_\sigma(|\vec{k}|, T)$ with respect to $|\vec{k}|$ is proportional to the conductivity. The results only include $\pi\pi$-scattering through a rho resonance.

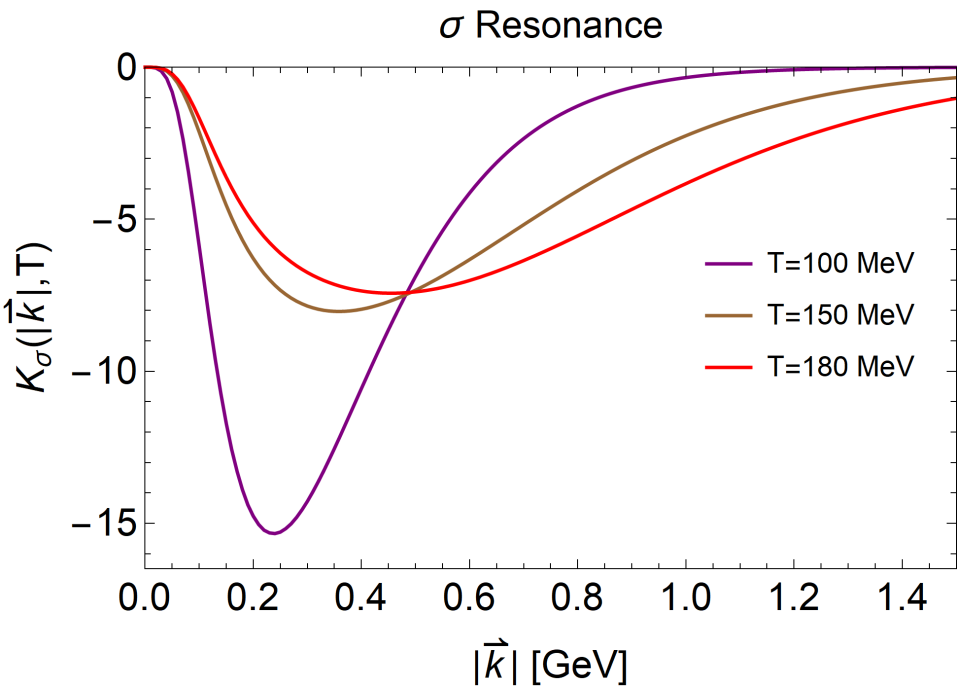

Figure 5.11: $K_\sigma(|\vec{k}|, T)$ as a function of momentum for T=100 MeV (purple), T=150 MeV (brown), and T=180 MeV (red). The integral of $K_\sigma(|\vec{k}|, T)$ with respect to $|\vec{k}|$ is proportional to the conductivity. The results only include $\pi\pi$-scattering through a sigma resonance.

Figure 5.12 plots $K_\sigma(|\vec{k}|, T)$ as a function of momentum for various temperatures, when resonant rho and sigma scattering are included. The conductivity adds inversely, so the total result is smaller than either individual contribution. Although, the S-wave interaction suppresses the low $\vec{k}$ region, a peak is still produced around $\vec{k} = 200$MeV (most noticeably for T=100 MeV). This occurs because even when S-wave interactions are included Σ_π is still smallest at low momentum (fig. 3.7). Thus $K_\sigma(|\vec{k}|, T)$ is largest at smaller momentum, where pions primarily interact through S-wave scattering, but is suppressed at higher momentum where the stronger P-wave interactions become more energetically favorable.

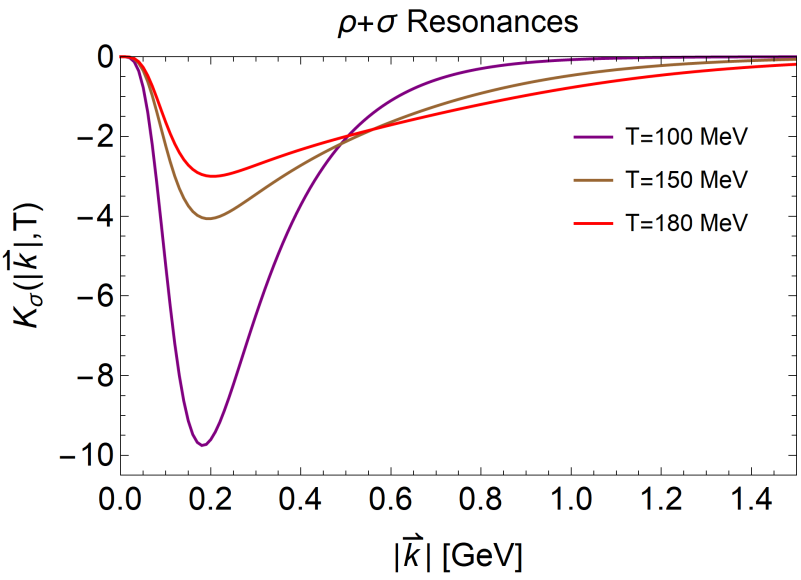

Figure 5.12: $K_\sigma(|\vec{k}|, T)$ as a function of momentum for T=100 MeV (purple), T=150 MeV (brown), and T=180 MeV (red). The integral of $K_\sigma(|\vec{k}|, T)$ with respect to $|\vec{k}|$ is proportional to the conductivity. The results include $\pi\pi$-scattering through rho and sigma resonances.

5.4 Rho self-energy with vertex corrections

Figures 5.13 and 5.14 display the imaginary and real parts of the transverse projection of the rho self-energy, for $\vec{q} = 0$, for T=150 MeV with and without vertex corrections. In figures 5.15 and 5.16 we plot the rho self-energy, at $\vec{q} = 0$, with vertex corrections for various temperatures. The results include interactions through rho and sigma resonances

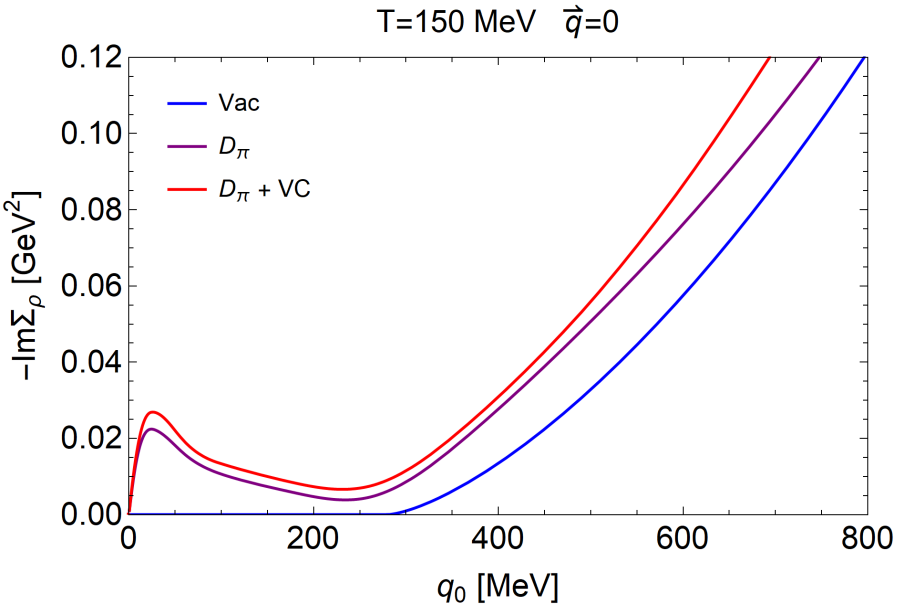

Figure 5.13: Imaginary part of the transverse projection of the rho self-energy in vacuum (blue) and at T=150 MeV with (purple) and without vertex corrections (red). Including vertex corrections results in an increase in $\mathrm{Im}\Sigma_\rho^T$. Results include the rho and sigma resonances.

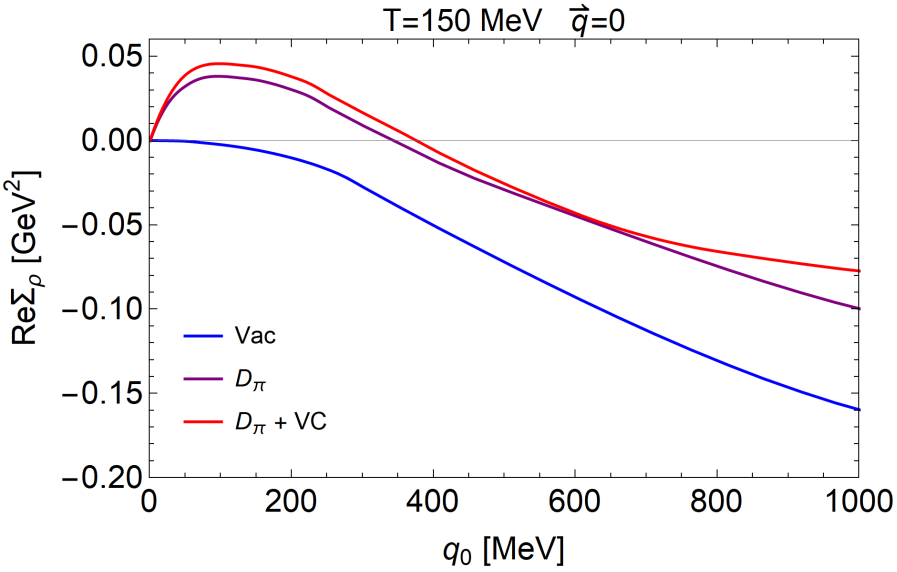

Figure 5.14: Real part of the transverse projection of the rho self-energy in vacuum (blue) and at T=150 MeV with (purple) and without vertex corrections (red). Including vertex corrections results in an increase in $\mathrm{Re}\Sigma_\rho^T$. Results include the rho and sigma resonances.

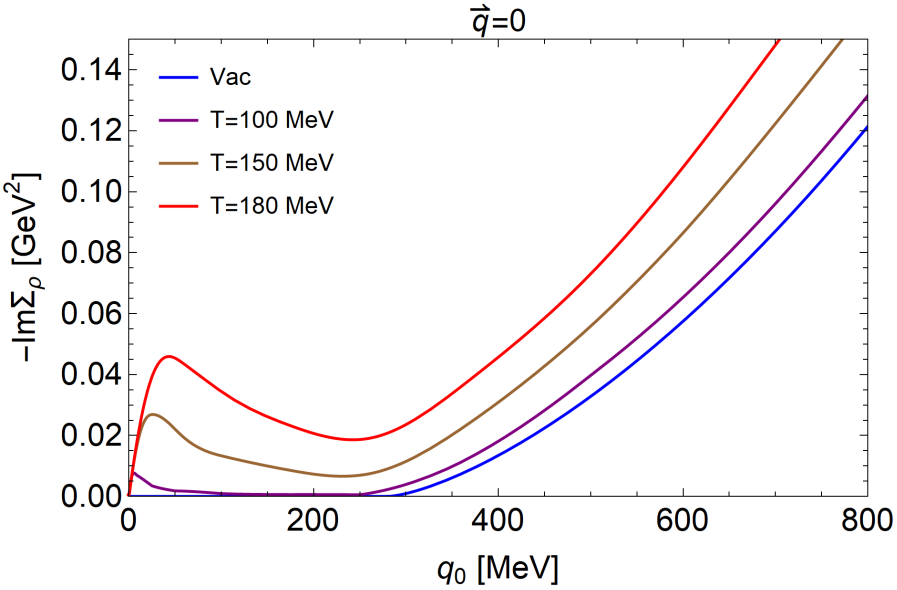

Figure 5.15: Imaginary part of the transverse projection of the rho self-energy at $\vec{q} = 0$ in vacuum (blue), and for various temperatures, T=100 MeV (purple), T=150 MeV (brown), and T=180 MeV (red), including vertex corrections. Results include the rho and sigma resonances.

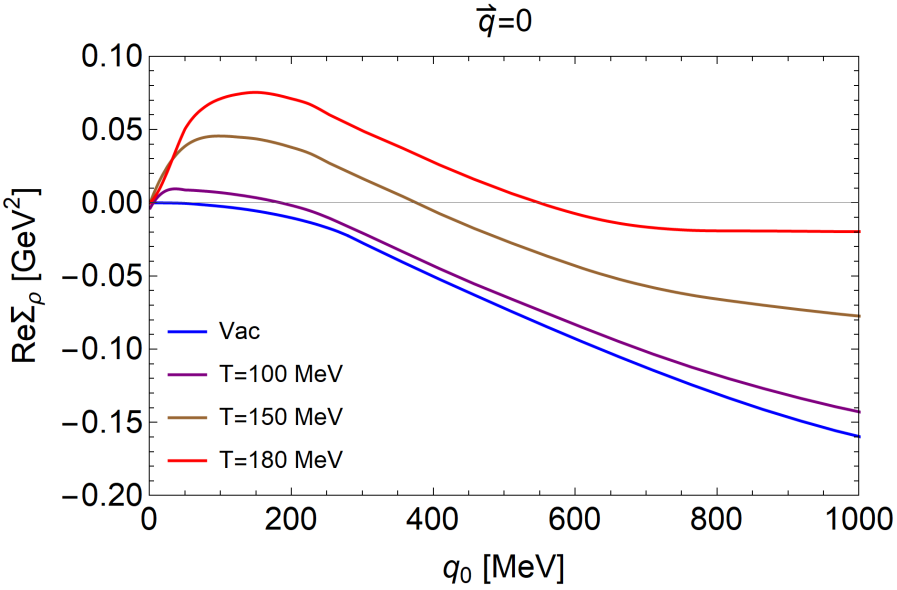

Figure 5.16: Real part of the transverse projection of the rho self-energy in vacuum (blue), and for various temperatures, T=100 MeV (purple), T=150 MeV (brown), and T=180 MeV (red), including vertex corrections. Results include the rho and sigma resonances.

We see that including vertex corrections results in an increase in the rho self-energy, which becomes more pronounced as temperature increases. This increase is expected because the vertex corrections introduce addition interactions for the rho. For q_0 around the rho mass this results in an increased rho width, while at low q_0 we see an increase in the shoulder generated by the Landau cut.

5.5 EM-spectral function with vertex correction

In this section we display the EM spectral function when vertex corrections are included. Figures 5.17 through 5.26 plot $\Pi^{ii}_{\rm EM}/q_0$ for various temperatures at $\vec{q} = 0$, scaled such that the conductivity corresponds to the intercept at zero energy. We include $\pi\pi$-scattering through rho and sigma resonances. Figures 5.17 through 5.20 and figures 5.22 through 5.25 compare the spectral function with and without vertex corrections, respectively, for T=100 MeV, T=120 MeV, T=150 MeV, and T=180 MeV. Additionally, figures 5.21 and 5.26 compare the spectral functions at T=100 MeV, T=150 MeV, and T=180 MeV, when vertex corrections are included. Plots are given which emphasize the rho pole at $q_0 = 770$MeV as well as the low energy transport peak.

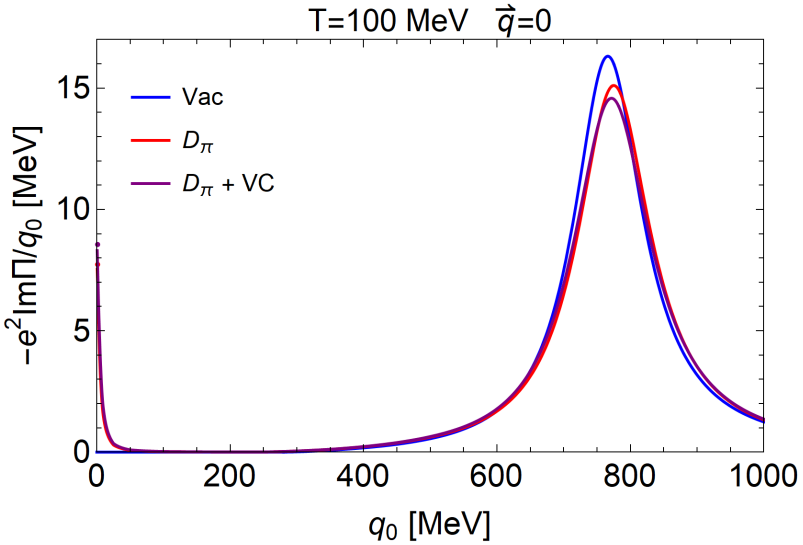

Figure 5.17: The electromagnetic spectral function at T=100 MeV, scaled such that the zero-energy intercept corresponds to $\sigma_{\rm el}$. Results are plotted as a function of energy at $\vec{q} = 0$, for; vacuum (blue), excluding vertex corrections (red), including vertex corrections (purple). The q_0 range is set to emphasize the rho pole.

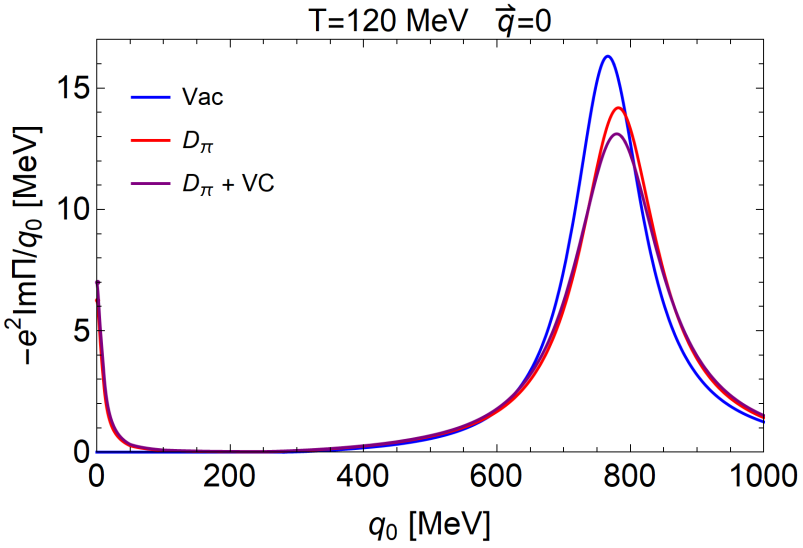

Figure 5.18: The electromagnetic spectral function at T=120 MeV, scaled such that the zero-energy intercept corresponds to σ_{el}. Results are plotted as a function of energy at $\vec{q} = 0$, for; vacuum (blue), excluding vertex corrections (red), including vertex corrections (purple). The q_0 range is set to emphasize the rho pole.

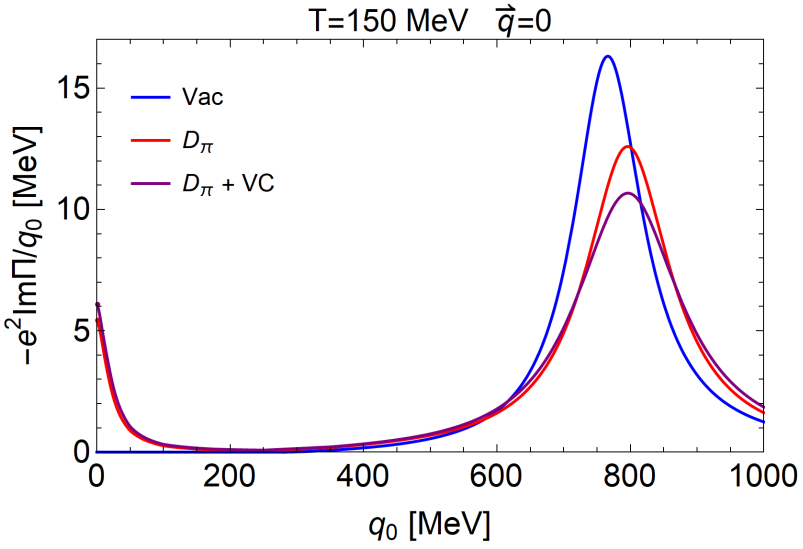

Figure 5.19: The electromagnetic spectral function at T=150 MeV, scaled such that the zero-energy intercept corresponds to σ_{el}. Results are plotted as a function of energy at $\vec{q} = 0$, for; vacuum (blue), excluding vertex corrections (red), including vertex corrections (purple). The q_0 range is set to emphasize the rho pole.

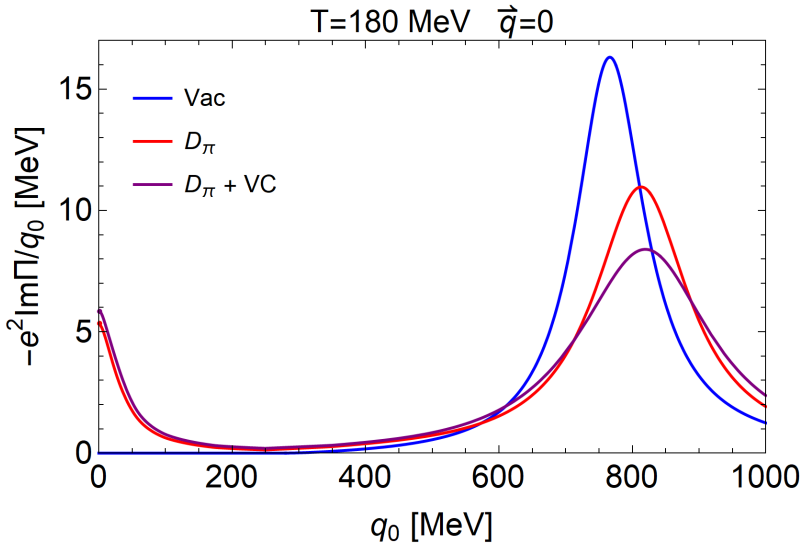

Figure 5.20: The electromagnetic spectral function at T=180 MeV, scaled such that the zero-energy intercept corresponds to σ_{el}. Results are plotted as a function of energy at $\vec{q} = 0$, for; vacuum (blue), excluding vertex corrections (red), including vertex corrections (purple). The q_0 range is set to emphasize the rho pole.

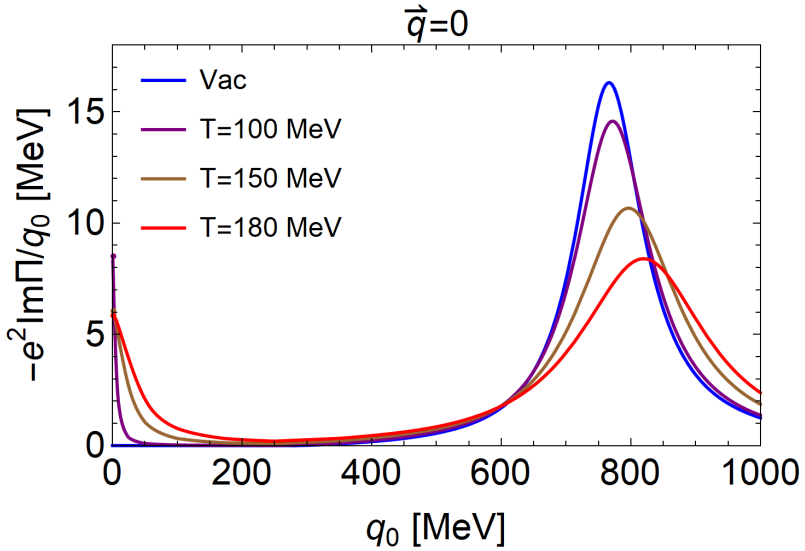

Figure 5.21: The electromagnetic spectral function including vertex correction at T=100 MeV (purple), T=150 MeV (brown), and T=180 MeV (red), scaled such that the zero-energy intercept corresponds to σ_{el}. The vacuum is also plotted in blue. Results are plotted as a function of energy at $\vec{q} = 0$. The q_0 range is set to emphasize the rho pole.

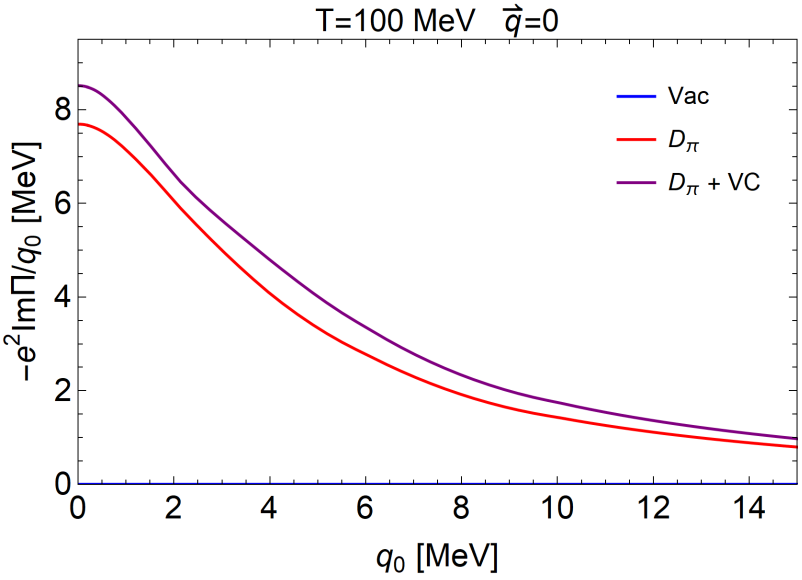

Figure 5.22: The electromagnetic spectral function at T=100 MeV, scaled such that the zero-energy intercept corresponds to σ_{el}. Results are plotted as a function of energy at $\vec{q} = 0$, for; vacuum (blue), excluding vertex corrections (red), including vertex corrections (purple). The q_0 range is set to emphasize the transport peak.

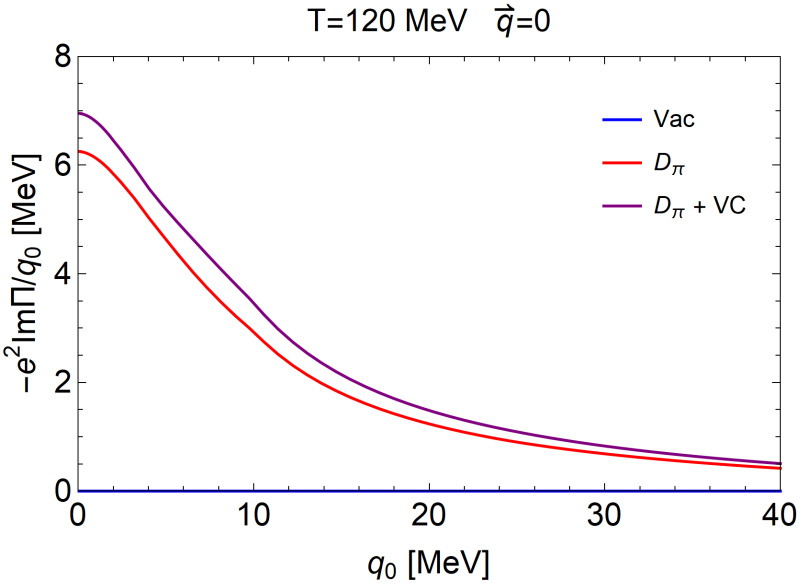

Figure 5.23: The electromagnetic spectral function at T=120 MeV, scaled such that the zero-energy intercept corresponds to σ_{el}. Results are plotted as a function of energy at $\vec{q} = 0$, for; vacuum (blue), excluding vertex corrections (red), including vertex corrections (purple). The q_0 range is set to emphasize the transport peak.

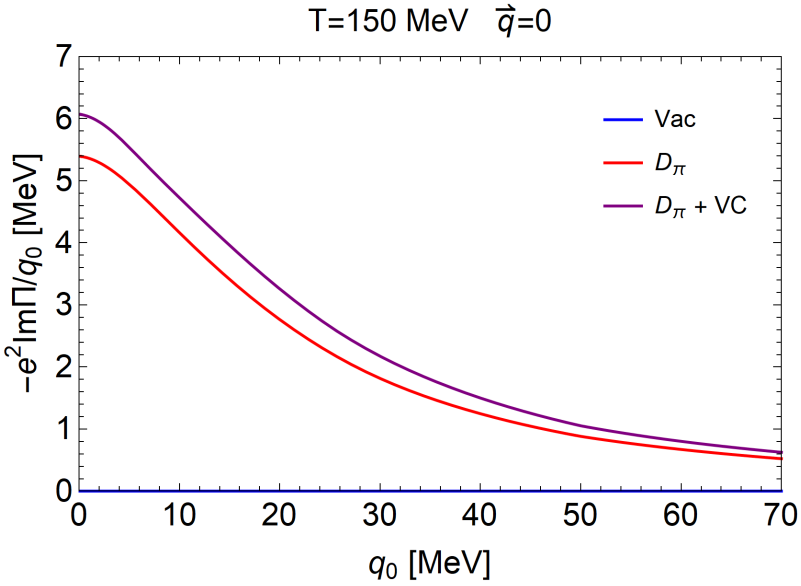

Figure 5.24: The electromagnetic spectral function at T=150 MeV, scaled such that the zero-energy intercept corresponds to σ_{el}. Results are plotted as a function of energy at $\vec{q} = 0$, for; vacuum (blue), excluding vertex corrections (red), including vertex corrections (purple). The q_0 range is set to emphasize the transport peak.

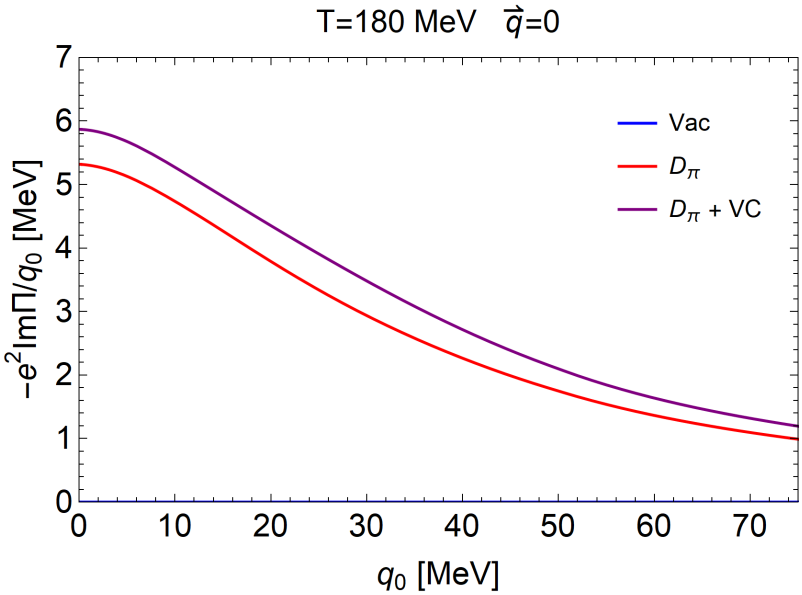

Figure 5.25: The electromagnetic spectral function at T=180 MeV, scaled such that the zero-energy intercept corresponds to σ_{el}. Results are plotted as a function of energy at $\vec{q} = 0$, for; vacuum (blue), excluding vertex corrections (red), including vertex corrections (purple). The q_0 range is set to emphasize the transport peak.

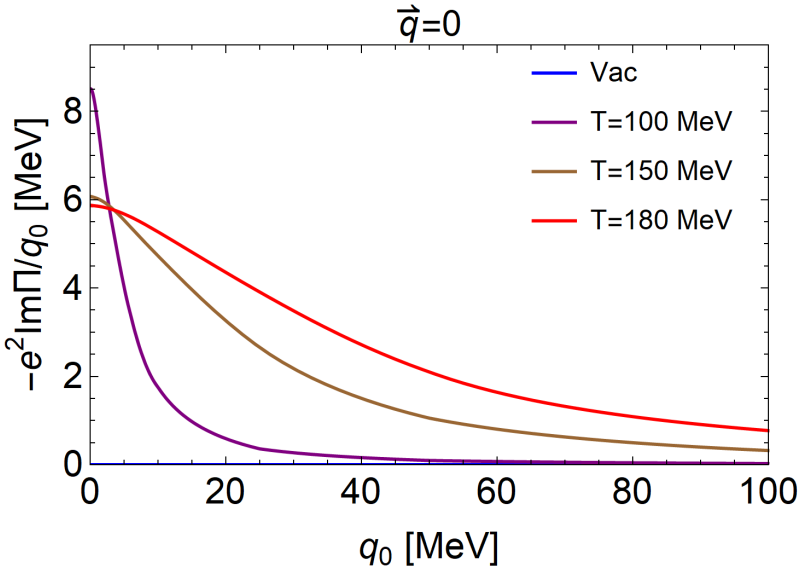

Figure 5.26: The electromagnetic spectral function including vertex correction at T=100 MeV (purple), T=150 MeV (brown), and T=180 MeV (red), scaled such that the zero-energy intercept corresponds to σ_{el}. The vacuum is also plotted in blue. Results are plotted as a function of energy at $\vec{q} = 0$. The q_0 range is set to emphasize the transport peak.

The vertex corrections result in a broadening of the rho peak that increases with temperature. This is expected because the corrections increase the rho's interaction with the medium. Furthermore, we see an increase in the transport peak, due to the vertex corrections. We have shown that at low q_0 the transport peak is roughly proportional to the imaginary part of the rho self-energy. The vertex corrections increase $\mathrm{Im}\Sigma_\rho$, thus the increased transport peak should be expected. However, this is somewhat counter intuitive, because the transport peak is also proportional to the electric conductivity. Therefore, it seems that increasing the medium interaction by including vertex corrections has resulted in a more conductive medium. In order to understand this phenomena, one must observe that the rho meson does not transmit electric charge through the medium. Charge is transmitted by the charged pion states, and in fact any increase in $\mathrm{Im}\Sigma_\pi$ will reduce the conductivity. Thus it is $\mathrm{Im}\Sigma_\pi$ which determines the interaction strength in the medium and not $\mathrm{Im}\Sigma_\rho$. On the other hand, the rho self-energy determines how the external photon couples to the medium. Therefore, the various rho self-energy diagrams represent different channels through which elec-

tric charge can travel. Therefore, the vertex corrections introduce additional channels for charge to flow through, increasing the electric conductivity.

5.6 σ/T with vertex corrections

In this section we examine the electric conductivity, extracted from the transport peak of the EM spectral function. In figure 5.27, we plot the conductivity over temperature with and without vertex correction. Results are shown for $\pi\pi$-scattering through only the rho or sigma resonance, as well as the result when scattering through both resonances are accounted for.

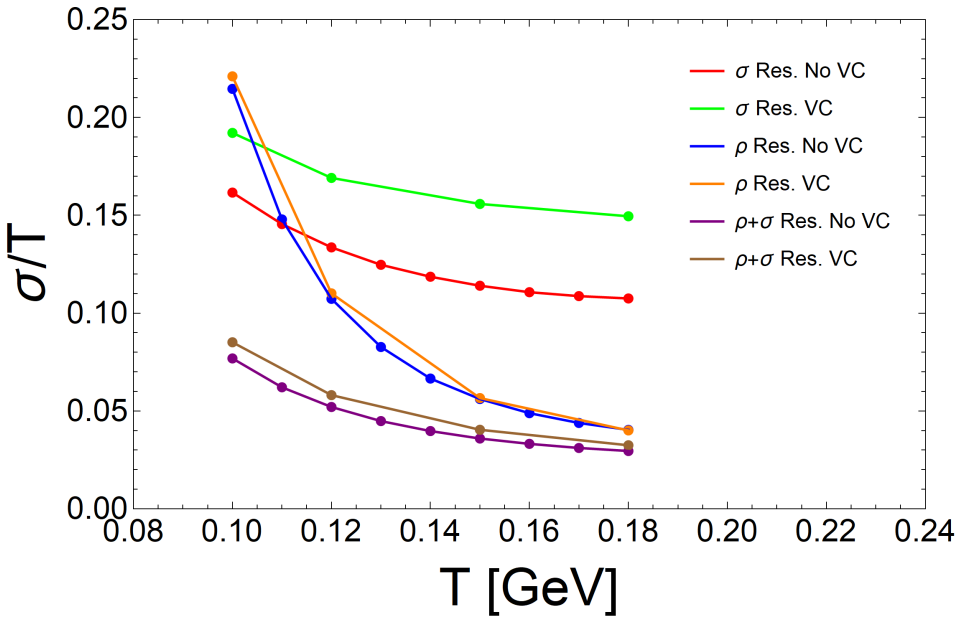

Figure 5.27: Pion gas conductivity over temperature for different $\pi\pi$-scattering resonances, with and without vertex corrections. Results including only the sigma resonance are plotted in red (vertex corrections excluded) and green (vertex corrections included). Results including only the rho resonance are plotted in blue (vertex corrections excluded) and orange (vertex corrections included). Results including both resonances are plotted in purple (vertex corrections excluded) and brown (vertex corrections included).

Figure 5.27 shows that the vertex corrections have the largest impact when only the sigma resonance is included, where they provide on average a $\sim$30% increase in the conductivity. Conversely, the vertex corrections have little impact when only the rho resonance is considered, providing ap-

proximately a 2% increase. When both resonances are included the vertex corrections increase the conductivity by approximately 10%. The relatively large increase in the sigma resonance results is caused primarily by $\Gamma^{(3)C\sigma}_{\mu\, ab3}$. Although one might expect this correction to still provide a significant increase in the conductivity when both resonances are considered, this is not the case. This is because the Landau cut of $\Gamma^{(3)C\sigma}_{\mu\, ab3}$ is proportional to the pion's width. Therefore, when the rho self-energy's Landau cut is dressed with $\Gamma^{(3)C\sigma}_{\mu\, ab3}$ the result is proportional to the pion's width squared. Thus, when the rho resonance is included in Σ_π this contribution experiences significant suppression relative to other rho self-energy diagrams. Due to this suppression, the largest correction to the rho self-energy, when both resonances are included, is from $\Gamma^{(3)E\rho}_{\mu\nu\, ab33}$ and $\Gamma^{(3)E\sigma}_{\mu\nu\, ab33}$, which account for about 70% of the vertex corrections' contribution to the rho self-energy.

In figure 5.28 we examine the impact of the additional vertex corrections induced by the form factor. The conductivity with and without the additional corrections is plotted, as well as the conductivity without vertex corrections. However, form factors are still included in all results, in order to assure convergence of the calculation. One can see that the form factor correction terms provide a small increase in the total conductivity, approximately 2.5%. However, because the contribution of the vertex corrections to the conductivity is rather small, these terms increase the effect of the vertex corrections by about 30%. This increase is fairly concerning, thus we intend to further investigate the violation of gauge invariance due to the form factor in future works.

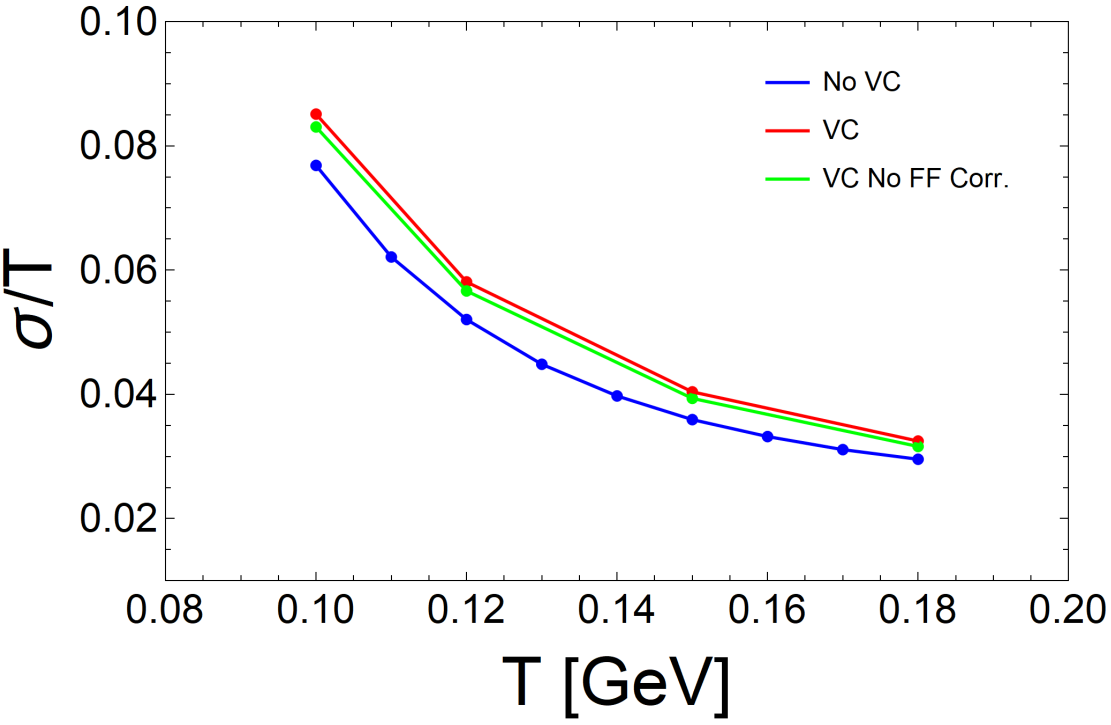

Figure 5.28: Pion gas conductivity over temperature without vertex corrections (blue), with vertex corrections (red), and including all vertex corrections except those induced by the form factor (green). The results include $\pi\pi$-scattering through rho and sigma resonances.

Finally, we compare our results for the hot pion matter conductivity to previous calculations in the literature in figures 5.29 and 5.30. In figure 5.29 we plot only results for hot pion matter, while in figure 5.30 we include results from lattice QCD.

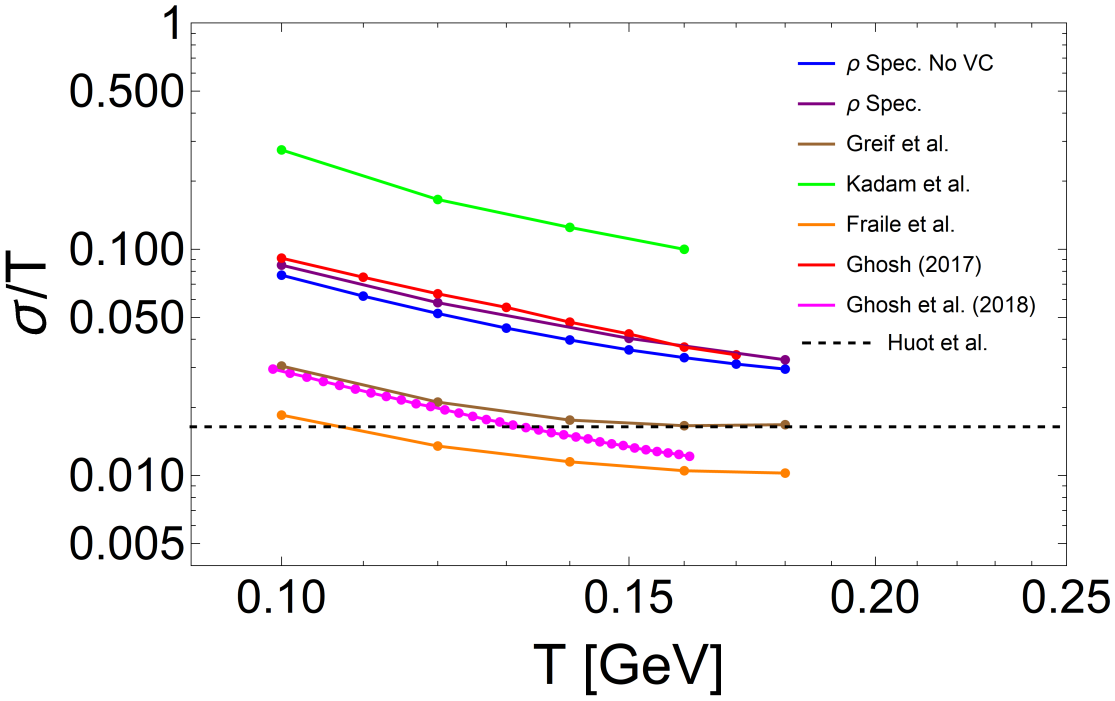

Figure 5.29: Pion matter conductivity over temperature compared to previous calculations in hot pion matter. The black dashed line shows a proposed lower bound from Ref. [22]. Our results are shown with and without vertex corrections in blue and purple, respectively. The kinetic theory results are plotted in brown [21], K-matrix results are plotted in green [29], chiral perturbation theory results are plotted in orange [23], real-time field theory results are plotted in red [30], and the results for the relaxation time approximation to the relativistic transport equation are plotted in magenta [31].

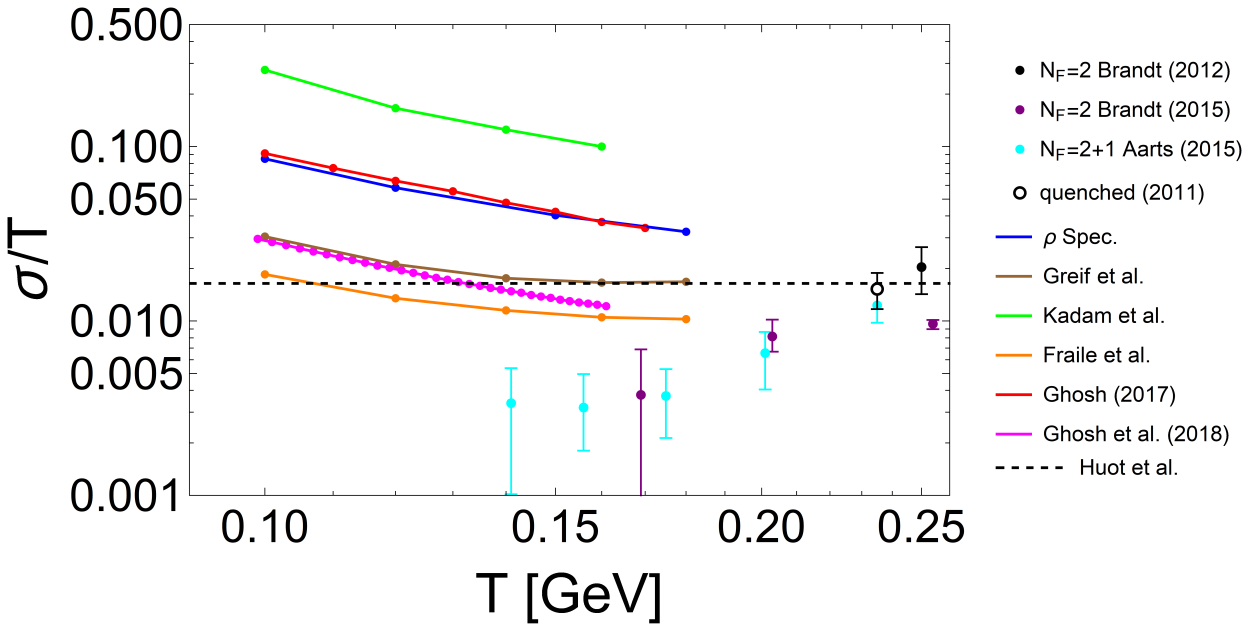

Figure 5.30: Pion matter conductivity over temperature compared to previous pion matter calculations, and lQCD results. The black dashed line shows a proposed lower bound from Ref. [22]. Our results are shown with and without vertex corrections in blue and purple, respectively. The kinetic theory results are plotted in brown [21], K-matrix results are plotted in green [29], chiral perturbation theory results are plotted in orange [23], real-time field theory results are plotted in red [30], and the results for the relaxation time approximation to the relativistic transport equation are plotted in magenta [31]. lQCD results for two $N_F = 2$ calculations are plotted with black and purple points [26, 27]. Finally, lQCD results for $N_F = 2 + 1$ are plotted with cyan points [25].

Our conductivity is significantly larger than the kinetic theory [21], chiral perturbation theory [23], and relaxation time approximation [31] results, but is smaller than the K-matrix calculation [29]. However, our calculation agrees fairly well with the real-time field theory results [30]. References [21], [23], [29] and [30] provide expressions for the conductivity in terms of either the pion width or the collision time, which are similar to our equation 2.46, however our inputs for the pion width vary.

Our calculation and the kinetic theory calculation derive the conductivity from similar pion cross sections. In ref. [21] the cross section is used to calculate the collision term, which is similar to our pion self-energy. The collision term is then used to solve the linearized Boltzmann equation, however when implemented in their electric charge current, ref. [21]'s interaction width appears

to differ from ours by a factor of two. The larger width could account for the smaller conductivity found in ref. [21].

In ref. [29] an expression for the conductivity in terms of the relaxation time is obtained by solving the Boltzmann equation. The pion's interactions are then calculated using the K-matrix formalism. Although ref. [29] implements a similar cross section to our own, they do not include the sigma resonance, which could account for some of the increase in ref. [29]'s calculation relative to our own. Additionally, ref. [29]'s expression for the conductivity differs from eq. 2.46 in that eq. 2.46 is proportional to the collision time, while ref. [29]'s expression is proportional to the relaxation time. Multiple collisions are required for a particle to equilibrize (typically one collision per spacial degree of freedom), thus the relaxation time is larger than the collision time. This difference could also account for an increase in ref. [29]'s conductivity relative to our own.

In ref. [23] chiral perturbation theory is used to derive an expression for the conductivity, which is equivalent to our eq. 2.46. The pion's width is then calculated using the Inverse Amplitude Method, which satisfies unitarity and matches ref. **??**'s low-energy chiral expansion. Although ref [23]'s width utilizes Boltzmann statistics rather than Bose, this should not produce a large effect in the conductivity at low temperatures. More work is needed to understand the apparent discrepancy between our pion width and that of ref. **??**.

In ref. [30] real-time thermal field-theory is used to derive an expression for the conductivity from the Kubo formula in terms of the pion width. Thermal pion widths are then derived from $\rho\pi$ and $\sigma\pi$ loops. As mentioned in section 3.5, ref. [30]'s pion widths are quite similar to our own, however ref. [30] does not dress the rho or sigma mesons with widths and uses a different $\sigma\pi\pi$ vertex. We would expect ref. [30]'s result to be similar to our result without vertex corrections, however [30]'s result is somewhat larger, which could be explained by ref. [30] implementing a smaller pion width.

In ref. [31] the conductivity is estimated by solving the relativistic transport equation in the relaxation time approximation. Pion interactions are derived in terms of elastic scattering amplitudes and consider scattering through both rho and sigma resonances. Furthermore, ref. [31] expresses

their amplitudes in terms of the $\pi\pi$-cross section and demonstrate a vacuum cross section which is similar to our own. However, ref. [31] then derives a mean reaction rate (thermal average over pion momentum) that is approximately four times larger than our own, indicating stronger interactions, which may explain the discrepancy between the results.

From figure 5.30 we see that the pion gas results are significantly larger than lQCD calculations, with most lQCD results falling below the proposed lower bound. Although this violation may seem concerning, the proposed lower bound from ref. [22] depends on the number of degrees of freedom in the calculation. Therefore, it may not be appropriate to compare pion matter and lQCD results to this lower bound. We address a more "universal" bound proposed by ref. [22] in chapter 6. Furthermore, in ref. [25] it is stated that their extraction of the conductivity at low temperature should be taken with caution, because they would not detect possible narrow transport peaks created by hadronic interactions.

Our results support a pion matter conductivity significantly higher than the lower bound proposed in ref. [22], which will impact charge correlations in HIC, however a more complete calculation in hadronic matter is required. Furthermore, our calculations indicate that the effects of the vertex corrections are rather small ($\sim 10\%$), instead the conductivity is dominated by the Landau cut of the rho self-energy, which is related to the pion's width. As demonstrated in eq. 2.46, the conductivity is inversely proportional to the pion's width. Therefore, the conductivity is very sensitive to pionic interactions and a robust calculation of the pion's width is required in order to reliably extract the conductivity.

In this chapter we perform further analysis of the EM spectral function. In section 6.1 we calculate the electric conductivity over the charge susceptibility, which provides a more "universal" lower bound on the conductivity [22]. We then test our EM spectral function against a sum rule calculated in ref. [45] in section 6.2.

6.1 Charge susceptibility

From figure 5.30, we see that several calculations either approach or violate the lower bound proposed in ref. [22]. However, one must be careful when comparing $\frac{\sigma_{el}}{T}$ to the lower bound, because $\frac{\sigma_{el}}{T}$ depends on the number of degrees of freedom in the system. Reference [22] proposed dividing the conductivity by the charge susceptibility. This cancels out the dependence on the degrees of freedom and provides a more "universal" quantity. The proposed lower bound from reference [22] is given by:

$$\frac{\sigma_{\text{el}}}{e^2\Xi} = \frac{1}{2\pi T}. \tag{6.1}$$

In order to compare our results to the lower bound we calculate the charge susceptibility in pion matter. To leading order in e^2 the susceptibility is related to the electromagnetic Debye mass squared by [57, 58, 59, 60]:

$$\Xi \;=\; -\lim_{\vec{q}\to 0}\Pi^{00}_{\text{EM}}(q_0=0,\vec{q}) = m_D^2. \tag{6.2}$$

With in the VDM one can write the Debye mass in terms of the rho propagator and self-energy

[61]:

$$\begin{aligned}
\Xi &= -\lim_{\vec{q}\to 0}\Big[\frac{(m_\rho^0)^4}{g_\rho^2}D_\rho^{00}(q_0=0,\vec{q}) - \frac{(m_\rho^0)^4}{g_\rho^2}D_{\rho\,vac}^{00}(0,0)\Big] \\
&= -\lim_{\vec{q}\to 0}\Big[\frac{(m_\rho^0)^4}{g_\rho^2}\Big(\frac{-1}{-\vec{q}^2-(m_\rho^0)^2-\Sigma_\rho^L(0,\vec{q})}\Big) - \frac{(m_\rho^0)^4}{g_\rho^2}\Big(\frac{-1}{-\vec{q}^2-(m_\rho^0)^2-\Sigma_{\rho\,vac}^L(0,0)}\Big)\Big] \\
&= \frac{(m_\rho^0)^4}{g_\rho^2}\Big(\frac{-1}{(m_\rho^0)^2-\Sigma_\rho^{00}(0,0)}\Big) - \frac{(m_\rho^0)^4}{g_\rho^2}\Big(\frac{-1}{(m_\rho^0)^2-\Sigma_{\rho\,vac}^{00}(0,0)}\Big). \qquad (6.3)
\end{aligned}$$

We see that while the conductivity corresponds to the time-like limit of $\mathrm{Im}\Pi_{\mathrm{EM}}^{\mu\nu}$, the susceptibility is determined by the space-like limit of $\mathrm{Re}\Pi_{\mathrm{EM}}^{\mu\nu}$. Though our formalism can be extended to finite $\vec{q}$, we have not calculated vertex corrections at finite $\vec{q}$, as this is beyond the scope of this work. However, we have seen that the dominant contribution to Σ_ρ comes from dressing the pion propagators with Σ_π. Here we calculate Ξ using the rho self-energy with dressed pion propagators, without including vertex corrections.

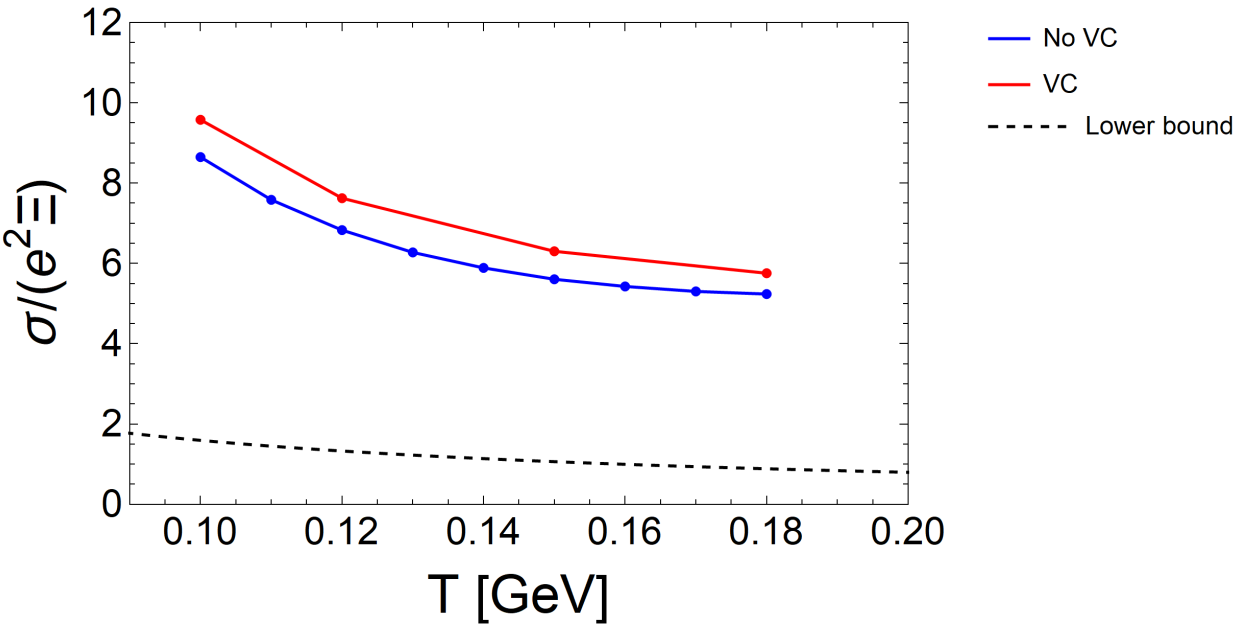

Figure 6.1: Electric conductivity divided by e^2 times the charge susceptibility. The charge susceptibility is calculated from Π_{EM}^{00} without including vertex corrections, however results are plotted for the conductivity with (red) and without (blue) vertex corrections. The black dashed line plots the result for the proposed lower bound from reference [22].

In figure 6.1 we plot our conductivity divided by e^2 times the charge susceptibility compared to the proposed lower bound from eq. 6.1 [22]. We see that our result is approximately a factor of 5 larger than the proposed lower bound. Furthermore, our calculation begins to level off as temperature increases while the lower bound is proportional to $\frac{1}{T}$. Therefore, we see that even when the number of degrees of freedom is accounted for, our result is well above the proposed lower bound.

6.2 Current conservation sum rule

In order to test our calculation, we utilize our EM spectral function to evaluate a sum rule calculated in ref [45]. The sum rule reads:

$$\int_0^\infty dw \frac{1}{w} \mathrm{Im}\Pi(w,T) = \int_0^\infty dw \frac{1}{w} \mathrm{Im}\Pi_{vac}(w). \tag{6.4}$$

Since the EM-correlator is proportional to the rho-spectral function in the VDM one can rewrite the sume rule as:

$$\int_0^\infty dw \frac{1}{w} \mathrm{Im}D_{\rho\, ii}(w,T) = \int_0^\infty dw \frac{1}{w} \mathrm{Im}D_{\rho\, ii\, vac}(w). \tag{6.5}$$

Equation 6.5 can be rewritten in the form of a dispersion relation at zero energy:

$$\lim_{q_0\to 0} \int_0^\infty dw \frac{2w}{q_0^2 - w^2} \mathrm{Im}D_{\rho\, ii}(w,T) = \lim_{q_0\to 0} \int_0^\infty dw \frac{2w}{q_0^2 - w^2} \mathrm{Im}D_{\rho\, ii\, vac}(w). \tag{6.6}$$

The dispersion relations can be solved analytically, as long as the rho propagator is analytic. Performing these integrations gives:

$$\mathrm{Re}D_{\rho\, ii}(0,T) = \mathrm{Re}D_{\rho\, ii\, vac}(0). \tag{6.7}$$

Equation 6.7 implies that to satisfy the sum rule D_ρ must be analytic and $\mathrm{Re}\Sigma_{\rho\, ii}(0,T) = 0$.

Calc	T=100 MeV	T=120 MeV	T=150 MeV	T=180 MeV
No VC	.32%	.34%	.36%	.57%
VC	.92%	.67%	.33%	.24%
VC No FF Corr.	.38%	.39%	.32%	.35%

Table 6.1: Violation of the sum rule proposed in ref. [45].

The energy dependent portion of $\mathrm{Re}\Sigma_\rho^T$ has been calculated with a dispersion relation, therefore D_ρ is guaranteed to be analytic. Furthermore, one can see from figures 5.2 and 5.14 that $\mathrm{Re}\Sigma_\rho^T(q_0 = 0, \vec{q} = 0)$ shows little deviation from zero. Therefore, we expect the violation of the sum rule to be small. In order to quantify the violation of the sum rule, we calculate the percent change in the left hand side of eq. 6.5 relative to the vacuum value. The violations with and without vertex correction are given in table 6.1. We see that before including vertex corrections the violation is extremely small, on average being less than .5%. When vertex corrections are included the violation increases for T=100 MeV and 120 MeV, but is reduced for T=150 MeV and 180 MeV. Furthermore, we see that the addition of the corrections induced by the form factors tend to increase the violation, especially for low temperature. Although the increase is a bit troubling, and provides further motivation to investigate a form factor that do not violate gauge invariance, it is reassuring that the violation is consistently less than 1%. In order to gain precision at this level we would likely require higher numerical precision and may need to calculate further iterations of the self-consistency equation induced by introducing the pion self-energy. This would require the dressing of thermal pions with Σ_π and the calculation of higher order vertex corrections.

7. SUMMARY AND FUTURE WORK

The creation of the QGP and hot hadronic matter has been a major accomplishment of HIC experiments at the LHC and RHIC. One means to study the medium created in HICs is to extract transport coefficients, which probe the low-energy, long-wavelength limit of the medium and are taken as inputs in transport models [16, 17].

In this work we set out to calculate the electric conductivity, which is expected to impact the evolution of charge correlations in HICs [20]. In particular, we calculated the conductivity of hot pion matter. The pion's mass is much smaller than that of nucleons and other mesons, thus $\pi\pi$-scattering is expected to play the leading role at low temperatures and chemical potentials. Previous calculations of the electric conductivity of pion matter and hot hadronic matter have varied considerably[21, 22, 23, 24, 25, 26, 27, 28, 29, 30, 31].

We have performed a quantum calculation based on successful descriptions of thermal dilepton emission rates [19, 62], where the EM spectral function was related to the imaginary part of the rho meson's propagator using the VDM. Interactions with the thermal medium were evaluated through the rho self-energy, $\Sigma_\rho^{\mu\nu}$. In pion matter a transport peak was generated by the Landau cut of $\Sigma_\rho^{\mu\nu}$, which corresponds to $\rho\pi$ scattering. However, it was found that $\pi\pi$-scattering needed to be considered in order to generate the pion's width and obtain a finite conductivity.

We included S- and P-wave scattering through sigma and rho resonances respectively, by resumming the pion propagators within $\Sigma_\rho^{\mu\nu}$ with pion self-energies. We then corrected for the violation of gauge invariance induced by this dressing with corrections to the $\rho\pi\pi$ and $\rho\rho\pi\pi$ vertices.

In order to calculate the vertex corrections, we followed the approach from refs. [46, 44] and generated vertex corrections by coupling rho mesons to Σ_π. The vertex corrections contain intermediate rho, sigma, and pi mesons, which transmit charge through the medium. Therefore, these mesons where dressed with widths in order to extract a finite conductivity.

Dressing the pion propagators creates a self-consistency equation, because the vertex corrections contain $\rho\pi\pi$ vertices. Furthermore, because the thermal particle in the rho self-energy's

Landau cut is identical to the thermal particle in Σ_π and the vertex corrections, the vertex corrections generated double counting, which was identified and removed. Finally, we regularized Σ_π and the vertex corrections with a form factor depending on the center of mass momentum, in order to avoid spurious momentum dependencies. Although this addition violates gauge invariance, we find that the violation is parametrically suppressed by the form factor cut off relative to the typical thermal pion momentum. We have then calculated approximate corrections for the violation.

The effect of the vertex corrections on the conductivity is rather small, resulting in approximately a 10% increase in the conductivity, with the primary contribution to the conductivity coming from the Landau cut of the rho self-energy. Furthermore, we have seen that both S- and P-wave $\pi\pi$-scattering contribute significantly to the conductivity. Although, the vertex corrections do not tend to improve the current conservation sum rule, the violations with or without vertex corrections are less than 1%, and correcting these violations will likely require the calculation of higher order vertex corrections, the dressing of thermal pions with Σ_π, and higher numerical precision. The choice of the center of mass momentum in the form factor may also contribute to the violation.

Our results support a conductivity significantly larger than existing calculations with kinetic theory, chiral perturbation theory, or the relaxation time approximation to the relativistic transport equation [21, 23, 31]. The result is also significantly smaller than the K-matrix calculation from ref. [29], but agrees fairly well with the real-time field theory calculation in ref. [30]. However, the variation in the conductivity does not appear to be due to the choice of formalism. The different calculations produce similar expressions for the conductivity in terms of the pion width. However, the various calculations input different pion widths, leading to differing conductivities. Furthermore, our conductivity is well above the quantum lower bound proposed in ref. [22], even when the dependency on the number of degrees of freedom is removed by dividing by the charge susceptibility.

We intend to extend our formalism to the strong coupling limit by increasing g_ρ. In this limit, the higher order corrections and the effect of the center of mass form factor may not be as heavily suppressed, therefore these effects will require further investigation. We will then extend our

calculation to hot hadronic matter with the addition of nucleons and kaons. The effect of nucleons at finite density and temperature can be included by combining this work's results with those of ref. [40]. This will require combining this work's pion self-energy with that of ref. [40] and the calculation of additional vertex corrections to the rho self-energy. After including nucleons we will continue our calculation of the conductivity of hot hadronic matter by calculating the effects of thermal kaons on Σ_π and the $\rho\pi\pi$ and $\rho\rho\pi\pi$ vertices. Both the probing of the strong coupling limit and the more complete hadronic matter calculation will likely bring the conductivity closer to the lower bound. However, our quantum calculation will be able to probe these scenarios by a controlled means and should respect the lower bound. Furthermore, in a more strongly coupled medium the increase in the conductivity due to the vertex corrections may be enhanced and provide a significant contribution to the conductivity.

Finally, we note that the ALICE-3 experiment, planed for run 5 of the LHC in the early 2030's, will be able to measure momenta down to a few tens of MeV [63]. These measurements will allow for the extraction of dilepton emission rates at low invariant mass where pionic interactions are curtail. Thus, we intend to carry our formalism to finite momentum, in order to calculate low energy dilepton emission rates. Furthermore, the experiment may allow for a measurement of the electric conductivity of hot QCD matter, providing further motivation to extend our formalism to more strongly coupled systems.

Bibliography

[1] H. Fritzsch, M. Gell-Mann and H. Leutwyler, Phys. Lett. B 47, 365 (1973).

[2] D. J. Gross and F. Wilczek, Phys. Rev. Lett. 30, 1346 (1973).

[3] H. D. Politzer, Phys. Rev. Lett. 30, 1346 (1973).

[4] E. V. Shuryak, The QCD Vacuum, Hadrons and Superdense Matter, 2. edition, World Scientific Lecture Notes in Physics, Vol. 71 (2004).

[5] J. I. Kapusta, Nucl. Phys. B 148, 461 (1979).

[6] R. Rapp, J. Wambach and H. van Hees, Landolt-Börnstein 23, 134 (2010).

[7] A. Das and T. Ferbel, *Introduction to Nuclear and Particle Physics*, World Scientific Publishing Co. (2003).

[8] U. W. Heinz and M. Jacob, arXiv:nucl-th/0002041 (2000).

[9] I. Arsene *et al.* (BRAHMS Collaboration), Nucl. Phys. A 757, 1 (2005).

[10] B.B. Back *et al.* (PHOBOS Collaboration), Nucl. Phys. A 757, 28 (2005).

[11] J. Adams *et al.* (STAR Collaboration), Nucl. Phys. A 757, 102 (2005).

[12] K. Adcox *et al.* (PHENIX Collaboration), Nucl. Phys. A 757, 184 (2005).

[13] P. W. Higgs, Phys. Rev. Lett. 12, 132 (1964).

[14] M. Gell-Mann, R. J. Oakes, and B. Renner, Phys. Rev. 175, 2195-2199 (1968).

[15] R. Rapp, T Schafer, E. V. Shuryak, and M. Velkovsky, Phys. Rev. Lett. 81, 53-56 (1998).

[16] U. Heinz, and R. Snellings, Ann. Rev. Nucl. Part. Sci. 63, 123-151 (2013).

[17] F. Prino, and R. Rapp, J. Phys. G 43, 093002 (2016).

[18] X. Dong, Y. Lee, and R. Rapp, Ann. Rev. Nucl. Part. Sci. 69, 417-445 (2019).

[19] R. Rapp, G. Chanfray, and J. Wambach, Nucl. Phys. A 617, 472-495 (1997).

[20] S. Pratt, arXiv:2104.00628v2 [nucl-th] (2021).

[21] M. Greif, C. Greiner and G. Denicol, Phys. Rev. D 93, 096012 (2016).

[22] S. C. Huot, P. Kovtun, G. D. Moore, A. Starinets, and L. G. Yaffe, JHEP, 015 (2006).

[23] D. Fernández-Fraile and A. Gomez Nicola, Phys. Rev. D 73, 045025 (2006).

[24] S. I. Finazzo and J. Noronha, Phys. Rev. D 89, 106008 (2014).

[25] G. Aarts, C. Allton, A. Amato, P. Giudice, S. Hands, and J.-I. Skullerud, JHEP 02, 186 (2015).

[26] B. B. Brandt, A. Francis, H. B. Meyer, and H. Wittig, JHEP 1303, 100 (2013).

[27] B. B. Brandt, A. Francis, B. Jäger, and H. B. Meyer, Phys. Rev. D 93, 054510 (2016).

[28] A. Amato, G. Aarts, C. Allton, P. Giudice, S. Hands, and J.-I. Skullerud, Phys. Rev. Lett. 111, 172001 (2013).

[29] G. Kadam, S. Pawar, and H. Mishra, J. Phys. G46, 015102 (2019).

[30] S. Ghosh, Phys. Rev. D 95, 036018 (2017).

[31] S. Ghosh, S. Mitra, and S. Sarkar, Nucl. Phys. A 969, 237-253 (2018).

[32] R. Rapp, and J. Wambach, Adv. Nucl. Phys. 25, 1-205 (2000).

[33] E. L. Feinberg, Nuovo Cim. A 34, 391 (1976).

[34] L. D. McLerran and T. Toimela, Phys. Rev. D 31, 545 (1985).

[35] G. Moore and J. Robert, arXiv:hep-ph/0607172v1 [nucl-th] (2006).

[36] J. J. Sakurai, *Currents and Mesons*, University of Chicago Press, Chicago (1969).

[37] C. Gale and J. Kapusta, Nucl. PHys. B357, 65 (1991).

[38] M. Herrmann, B.L. Friman, and W. Norenberg, Nucl. Phys. A 560, 411-436 (1993).

[39] G. Chanfray, R. Rapp, and J. Wambach, Phys. Rev. Lett. 76, 368-371 (1996).

[40] M. Urban, M. Buballa, R. Rapp, and J. Wambach, Nucl. Phys. A 673, 357 (2000).

[41] M. Asakawa and C. M. Ko, Phys. Rev. C 48, R526 (1993).

[42] B. Friman and H. J. Pirner, Nucl. Phys. A 617, 496-509 (1997).

[43] G. Chanfray, and P. Schuck, Nucl. Phys. A 545, 271C-276C (1992).

[44] C. Song, and V. Koch, Phys. Rev. C 54, 3218 (1996).

[45] P. Gubler and D. Satow, Phys. Rev. D 94, 094042 (2016).

[46] M. Urban, M. Buballa, R. Rapp and J. Wambach, Nucl. Phys. A 641 433 (1998).

[47] L. Fetter and J. D. Walecka, *Quantum Theory of Many-Particle Systems*, McGraw-Hill, New York (1971).

[48] R. Rapp and J. Wambach, Phys. Lett. B 315, 220-225 (1993).

[49] M. Greif, I. Bouras, C. Greiner, and Z. Xu, Phys. Rev. D 90, 094014 (2014).

[50] R. Rapp, J. W. Durso, and J Wambach, Nucl. Phys. A 596, 436-450 (1996).

[51] R. Rapp, *Pion-Pion Wechselwirkungen in dichter/heißer Materie*, Institut für Kernphysik Forschungszentrum Jülich, (1996).

[52] Z. Aouissat, R. Rapp, G. Chanfray, P. Schuck and J. Wambach, Nucl. Phys. A 581, 471 (1995).

[53] R.D. Pisarski, Phys. Rev. D52, R3773 (1995).

[54] C. Froggatt, and J. Petersen, Nucl. Phys. B 129, 89-110 (1977).

[55] M. Urban, Impulsabhängigkeit des ρ-Meson-Propagators in kalter Kernmaterie, Institut für Kernphysik Technische Hochschule Darmstadt (1999).

[56] S.D. Protopopescu, M. Alston-Garnjost, A Barbaro-Galtieri, S.M. Flatté, J.H. Freidman, G.R. Lynch, M.S. Rabin, F.T. Solnitz, Phys. Rev. D 9, 1872 (1974).

[57] L. McLerran, Phys. Rev. D 36, 3291 (1987).

[58] J. Kapusta, *Finite Temperature Field Theory*, Cambridge University Press (1989).

[59] M. Prakash and I. Zahed, Phys. Rev. Lett. 69, 3282 (1992).

[60] J.-P. Blaizot, E. Iancu, and R.R. Parwani, Phys. Rev. D 52, 2543 (1995).

[61] M. Prakash, R. Rapp, J Wambach, and I Zahed, Phys. Rev. C 65, 034906 (2002).

[62] R. Rapp, and J. Wambach, Eur. Phys. J. A 6, 415-420 (1999).

[63] D. Adamová *et al.*, arXiv:1902.01211v2 [physics.ins-det] (2019).

APPENDIX A

Vertex correction Matsubara sums

In this appendix we perform the Matsubara sums involved in calculating the vertex corrections introduced in chapter 4. The vertex corrections that remain after dropping corrections with multiple rho propagators are: $\Gamma^{(3)A\rho}_{\mu\,ab3}$, $\Gamma^{(3)B\rho}_{\mu\,ab3}$, $\Gamma^{(3)C\rho}_{\mu\,ab3}$, $\Gamma^{(3)C\sigma}_{\mu\,ab3}$, $\Gamma^{(4)A\rho}_{\mu\nu\,ab33}$, $\Gamma^{(4)B_1\rho}_{\mu\nu\,ab33}$, $\Gamma^{(4)B_2\rho}_{\mu\nu\,ab33}$, $\Gamma^{(4)E\rho}_{\mu\nu\,ab33}$, $\Gamma^{(4)G\rho}_{\mu\nu\,ab33}$, $\Gamma^{(4)E\sigma}_{\mu\nu\,ab33}$, and $\Gamma^{(4)G\sigma}_{\mu\nu\,ab33}$. In order to avoid double counting, diagrams $\Gamma^{(4)B_1\rho}_{\mu\nu\,ab33}$, $\Gamma^{(4)B_2\rho}_{\mu\nu\,ab33}$, $\Gamma^{(4)E\rho}_{\mu\nu\,ab33}$, $\Gamma^{(4)G\rho}_{\mu\nu\,ab33}$, $\Gamma^{(4)E\sigma}_{\mu\nu\,ab33}$, and $\Gamma^{(4)G\sigma}_{\mu\nu\,ab33}$ are only calculated when the external pion corresponds to a vacuum pion. Furthermore, the rho self-energy contributions resulting from these diagrams can be expressed in terms of the pion unitarity cut. We begin by presenting the corrections to the $\pi\pi$-loop from the three-point vertex corrections in A.1.1. In section A.1.2 we present the corrections to the tad pole loop from the four-point vertex corrections. Finally, in section A1.3 we give the total correction to the rho self-energy.

A.1 $\pi\pi$-loop corrections

It is straight forward to express the propagators in the vertex corrections in terms of a spectral representation, as was done for the rho and pion self-energies. The Matsubara sums can then be calculated using eq. 2.23. Here we write the imaginary parts of $\Gamma^{(3)A\rho}_{\mu\,ab3}$, $\Gamma^{(3)B\rho}_{\mu\,ab3}$, $\Gamma^{(3)C\rho}_{\mu\,ab3}$, and $\Gamma^{(3)C\sigma}_{\mu\,ab3}$ relevant for maintaining gauge invariance when D_π is dressed with the Landau cut of the pion

self-energy.

$$
\begin{aligned}
\mathrm{Im}\Gamma^{\prime\prime(3)A\rho}_{\mu\,ab3}(k,q) &= -\epsilon_{3ab}\frac{3g_\rho^3}{2}\int\frac{d^3p}{(2\pi)^3}\Bigg[\int_0^\infty\frac{dw}{-\pi}\mathrm{Im}[D_\pi(p)]\mathrm{Im}[D_\rho^{\nu\lambda}(p+k)] \\
&\quad g_{\mu\lambda}(k-p)_\nu(f(w)-f(k_0+w)) \\
&\quad \theta(k_0+w)\mathrm{FF}_\rho[-q+p,q+k]\mathrm{FF}_\rho[p,k]\Bigg]_{p_0=w} \\
&\quad +\epsilon_{3ab}\frac{3g_\rho^3}{2}\int\frac{d^3p}{(2\pi)^3}\Bigg[\int_0^\infty\frac{dw}{-\pi}\mathrm{Im}[D_\pi(p)]\mathrm{Im}[D_\rho^{\nu\lambda}(p+k)] \\
&\quad g_{\mu\lambda}(k-p)_\nu(f(w)-f(-k_0+w)) \\
&\quad \theta(-k_0+w)\mathrm{FF}_\rho[-q+p,q+k]\mathrm{FF}_\rho[p,k]\Bigg]_{p_0=-w}, \qquad \text{(A.1)}
\end{aligned}
$$

$$
\begin{aligned}
\mathrm{Im}\Gamma^{\prime\prime(3)B\rho}_{\mu\,ab3}(k,q) &= -\epsilon_{3ab}\frac{3g_\rho^3}{2}\int\frac{d^3p}{(2\pi)^3}\Bigg[\int_0^\infty\frac{dw}{-\pi}\mathrm{Im}[D_\pi(p)]\mathrm{Im}[D_\rho^{\nu\lambda}(q+k+p)] \\
&\quad g_{\mu\lambda}(q+k-p)_\nu(f(w)-f(q_0+k_0+w)) \\
&\quad \theta(q_0+k_0+w)\mathrm{FF}_\rho[q+p,k]\mathrm{FF}_\rho[p,q+k]\Bigg]_{p_0=w} \\
&\quad +\epsilon_{3ab}\frac{3g_\rho^3}{2}\int\frac{d^3p}{(2\pi)^3}\Bigg[\int_0^\infty\frac{dw}{-\pi}\mathrm{Im}[D_\pi(p)]\mathrm{Im}[D_\rho^{\nu\lambda}(q+k+p)] \\
&\quad g_{\mu\lambda}(q+k-p)_\nu(f(w)-f(-q_0-k_0+w)) \\
&\quad \theta(-q_0-k_0+w)\mathrm{FF}_\rho[q+p,k]\mathrm{FF}_\rho[p,q+k]\Bigg]_{p_0=-w}, \qquad \text{(A.2)}
\end{aligned}
$$

$$
\begin{aligned}
\mathrm{Im}\Gamma^{\prime\prime(3)C\rho}_{\mu\,ab3}(k,q) \;=\;& \epsilon_{3ab}\frac{g_\rho^3}{2}\int\frac{d^3p}{(2\pi)^3}\Bigg[\int_0^\infty\frac{dw}{-\pi}\mathrm{Im}[D_\pi(p)]\mathrm{Re}[D_\pi(q-p)]\mathrm{Im}[D_\rho^{\nu\lambda}(p+k)] \\
& (-2p+q)_\mu(-p+k+2q)_\lambda(k-p)_\nu(f(w)-f(k_0+w)) \\
& \theta(k_0+w)\mathrm{FF}_\rho[p,k]\mathrm{FF}_\rho[-q+p,q+k]\Bigg]_{p_0=w} \\
& -\epsilon_{3ab}\frac{g_\rho^3}{2}\int\frac{d^3p}{(2\pi)^3}\Bigg[\int_0^\infty\frac{dw}{-\pi}\mathrm{Im}[D_\pi(p)]\mathrm{Re}[D_\pi(q-p)]\mathrm{Im}[D_\rho^{\nu\lambda}(p+k)] \\
& (-2p+q)_\mu(-p+k+2q)_\lambda(k-p)_\nu(f(w)-f(-k_0+w)) \\
& \theta(-k_0+w)\mathrm{FF}_\rho[p,k]\mathrm{FF}_\rho[-q+p,q+k]\Bigg]_{p_0=-w} \\
& +\epsilon_{3ab}\frac{g_\rho^3}{2}\int\frac{d^3p}{(2\pi)^3}\Bigg[\int_0^\infty\frac{dw}{-\pi}\mathrm{Im}[D_\pi(p)]\mathrm{Re}[D_\pi(q+p)]\mathrm{Im}[D_\rho^{\nu\lambda}(q+k+p)] \\
& (-2p-q)_\mu(-p+k+q)_\lambda(k-q-p)_\nu(f(w)-f(q_0+k_0+w))) \\
& \theta(q_0+k_0+w\mathrm{FF}_\rho[q+p,k]\mathrm{FF}_\rho[p,q+k]\Bigg]_{p_0=w} \\
& -\epsilon_{3ab}\frac{g_\rho^3}{2}\int\frac{d^3p}{(2\pi)^3}\Bigg[\int_0^\infty\frac{dw}{-\pi}\mathrm{Im}[D_\pi(p)]\mathrm{Re}[D_\pi(q+p)]\mathrm{Im}[D_\rho^{\nu\lambda}(q+k+p)] \\
& (-2p-q)_\mu(-p+k+q)_\lambda(k-q-p)_\nu(f(w)-f(-q_0-k_0+w)) \\
& \theta(-q_0-k_0+w)\mathrm{FF}_\rho[q+p,k]\mathrm{FF}_\rho[p,q+k]\Bigg]_{p_0=-w} \\
& +\epsilon_{3ab}\frac{g_\rho^3}{2}\int\frac{d^3p}{(2\pi)^3}\Bigg[\int_0^\infty\frac{dw}{-\pi}\mathrm{Im}[D_\pi(p)]\mathrm{Im}[D_\pi(q+p)]\mathrm{Re}[D_\rho^{\nu\lambda}(q+k+p)] \\
& (-2p-q)_\mu(-p+k+q)_\lambda(k-q-p)_\nu(f(w)-f(q_0+w)) \\
& \mathrm{FF}_\rho[q+p,k]\mathrm{FF}_\rho[p,q+k]\Bigg]_{p_0=w} \\
& -\epsilon_{3ab}\frac{g_\rho^3}{2}\int\frac{d^3p}{(2\pi)^3}\Bigg[\int_0^\infty\frac{dw}{-\pi}\mathrm{Im}[D_\pi(p)]\mathrm{Im}[D_\pi(q-p)]\mathrm{Re}[D_\rho^{\nu\lambda}(p+k)] \\
& (-2p+q)_\mu(-p+k+2q)_\lambda(k-p)_\nu(f(w)-f(q_0+w)) \\
& \mathrm{FF}_\rho[p,k]\mathrm{FF}_\rho[-q+p,q+k]\Bigg]_{p_0=-w}, \qquad \text{(A.3)}
\end{aligned}
$$

$$
\begin{aligned}
\mathrm{Im}\Gamma^{\prime\prime(3)C\sigma}_{\mu\,ab3}(k,q) &= \epsilon_{3ab}\frac{g_\rho g_\sigma^2}{2}\int\frac{d^3p}{(2\pi)^3}\Bigg[\int_0^\infty\frac{dw}{-\pi}\mathrm{Im}[D_\pi(p)]\mathrm{Re}[D_\pi(q-p)]\mathrm{Im}[D_\sigma(p+k)] \\
&\quad ((p+k)^2-m_\pi^2)(-2p+q)_\mu(f(w)-f(k_0+w)) \\
&\quad \theta(k_0+w)\mathrm{FF}_\sigma[p,k]\mathrm{FF}_\sigma[-q+p,q+k]\Bigg]_{p_0=w} \\
&\quad -\epsilon_{3ab}\frac{g_\rho g_\sigma^2}{2}\int\frac{d^3p}{(2\pi)^3}\Bigg[\int_0^\infty\frac{dw}{-\pi}\mathrm{Im}[D_\pi(p)]\mathrm{Re}[D_\pi(q-p)]\mathrm{Im}[D_\sigma(p+k)] \\
&\quad ((p+k)^2-m_\pi^2)(-2p+q)_\mu(f(w)-f(-k_0+w)) \\
&\quad \theta(-k_0+w)\mathrm{FF}_\sigma[p,k]\mathrm{FF}_\sigma[-q+p,q+k]\Bigg]_{p_0=-w} \\
&\quad +\epsilon_{3ab}\frac{g_\rho g_\sigma^2}{2}\int\frac{d^3p}{(2\pi)^3}\Bigg[\int_0^\infty\frac{dw}{-\pi}\mathrm{Im}[D_\pi(p)]\mathrm{Re}[D_\pi(q+p)]\mathrm{Im}[D_\sigma(q+k+p)] \\
&\quad ((q+k+p)^2-m_\pi^2)(-2p-q)_\mu(f(w)-f(q_0+k_0+w)) \\
&\quad \theta(q_0+k_0+w)\mathrm{FF}_\sigma[q+p,k]\mathrm{FF}_\sigma[p,q+k]\Bigg]_{p_0=w} \\
&\quad -\epsilon_{3ab}\frac{g_\rho g_\sigma^2}{2}\int\frac{d^3p}{(2\pi)^3}\Bigg[\int_0^\infty\frac{dw}{-\pi}\mathrm{Im}[D_\pi(p)]\mathrm{Re}[D_\pi(q+p)]\mathrm{Im}[D_\sigma(q+k+p)] \\
&\quad ((q+k+p)^2-m_\pi^2)(-2p-q)_\mu(f(w)-f(-q_0-k_0+w)) \\
&\quad \theta(-q_0-k_0+w)\mathrm{FF}_\sigma[q+p,k]\mathrm{FF}_\sigma[p,q+k]\Bigg]_{p_0=-w} \\
&\quad +\epsilon_{3ab}\frac{g_\rho g_\sigma^2}{2}\int\frac{d^3p}{(2\pi)^3}\Bigg[\int_0^\infty\frac{dw}{-\pi}\mathrm{Im}[D_\pi(p)]\mathrm{Im}[D_\pi(q+p)]\mathrm{Re}[D_\sigma(q+k+p)] \\
&\quad ((q+k+p)^2-m_\pi^2)(-2p-q)_\mu(f(w)-f(q_0+w)) \\
&\quad \mathrm{FF}_\sigma[q+p,k]\mathrm{FF}_\sigma[p,q+k]\Bigg]_{p_0=w} \\
&\quad -\epsilon_{3ab}\frac{g_\rho g_\sigma^2}{2}\int\frac{d^3p}{(2\pi)^3}\Bigg[\int_0^\infty\frac{dw}{-\pi}\mathrm{Im}[D_\pi(p)]\mathrm{Im}[D_\pi(q-p)]\mathrm{Re}[D_\sigma(p+k)] \\
&\quad ((p+k)^2-m_\pi^2)(-2p+q)_\mu(f(w)-f(q_0+w)) \\
&\quad \mathrm{FF}_\sigma[p,k]\mathrm{FF}_\sigma[-q+p,q+k]\Bigg]_{p_0=w}. \qquad \text{(A.4)}
\end{aligned}
$$

In order to help group $\Gamma^{\prime\prime(3)C\rho}_{\mu\,ab3}$ and $\Gamma^{\prime\prime(3)C\sigma}_{\mu\,ab3}$ into spectral representations we define the functions:

$$
\begin{aligned}
\mathrm{Im}\Gamma^{\prime\prime(3)C\rho k}_{\mu\,ab3}(k,q) &= \epsilon_{3ab}\frac{g_\rho^3}{2}\int\frac{d^3p}{(2\pi)^3}\Bigg[\int_0^\infty\frac{dw}{-\pi}\mathrm{Im}[D_\pi(p)]\mathrm{Re}[D_\pi(q-p)]\mathrm{Im}[D_\rho^{\nu\lambda}(p+k)] \\
&\quad (-2p+q)_\mu(-p+k+2q)_\lambda(k-p)_\nu(f(w)-f(k_0+w)) \\
&\quad \theta(k_0+w)\mathrm{FF}_\rho[p,k]\mathrm{FF}_\rho[-q+p,q+k]\Bigg]_{p_0=w} \\
&\quad -\epsilon_{3ab}\frac{g_\rho^3}{2}\int\frac{d^3p}{(2\pi)^3}\Bigg[\int_0^\infty\frac{dw}{-\pi}\mathrm{Im}[D_\pi(p)]\mathrm{Re}[D_\pi(q-p)]\mathrm{Im}[D_\rho^{\nu\lambda}(p+k)] \\
&\quad (-2p+q)_\mu(-p+k+2q)_\lambda(k-p)_\nu(f(w)-f(-k_0+w)) \\
&\quad \theta(-k_0+w)\mathrm{FF}_\rho[p,k]\mathrm{FF}_\rho[-q+p,q+k]\Bigg]_{p_0=-w}, \qquad \text{(A.5)} \\
\mathrm{Im}\Gamma^{\prime\prime(3)C\rho q}_{\mu\,ab3}(k,q) &= \epsilon_{3ab}\frac{g_\rho^3}{2}\int\frac{d^3p}{(2\pi)^3}\Bigg[\int_0^\infty\frac{dw}{-\pi}\mathrm{Im}[D_\pi(p)]\mathrm{Re}[D_\pi(q+p)]\mathrm{Im}[D_\rho^{\nu\lambda}(q+k+p)] \\
&\quad (-2p-q)_\mu(-p+k+q)_\lambda(k-q-p)_\nu(f(w)-f(q_0+k_0+w)) \\
&\quad \theta(q_0+k_0+w)\mathrm{FF}_\rho[q+p,k]\mathrm{FF}_\rho[p,q+k]\Bigg]_{p_0=w} \\
&\quad -\epsilon_{3ab}\frac{g_\rho^3}{2}\int\frac{d^3p}{(2\pi)^3}\Bigg[\int_0^\infty\frac{dw}{-\pi}\mathrm{Im}[D_\pi(p)]\mathrm{Re}[D_\pi(q+p)]\mathrm{Im}[D_\rho^{\nu\lambda}(q+k+p)] \\
&\quad (-2p-q)_\mu(-p+k+q)_\lambda(k-q-p)_\nu(f(w)-f(-q_0-k_0+w)) \\
&\quad \theta(-q_0-k_0+w)\mathrm{FF}_\rho[q+p,k]\mathrm{FF}_\rho[p,q+k]\Bigg]_{p_0=-w}, \qquad \text{(A.6)} \\
\mathrm{Im}\Gamma^{\prime\prime(3)C\rho k\pi}_{\mu\,ab3}(k,q) &= -\epsilon_{3ab}\frac{g_\rho^3}{2}\int\frac{d^3p}{(2\pi)^3}\Bigg[\int_0^\infty\frac{dw}{-\pi}\mathrm{Im}[D_\pi(p)]\mathrm{Im}[D_\pi(q-p)]\mathrm{Re}[D_\rho^{\nu\lambda}(p+k)] \\
&\quad (-2p+q)_\mu(-p+k+2q)_\lambda(k-p)_\nu(f(w)-f(q_0+w)) \\
&\quad \mathrm{FF}_\rho[p,k]\mathrm{FF}_\rho[-q+p,q+k]\Bigg]_{p_0=-w}, \qquad \text{(A.7)} \\
\mathrm{Im}\Gamma^{\prime\prime(3)C\rho q\pi}_{\mu\,ab3}(k,q) &= \epsilon_{3ab}\frac{g_\rho^3}{2}\int\frac{d^3p}{(2\pi)^3}\Bigg[\int_0^\infty\frac{dw}{-\pi}\mathrm{Im}[D_\pi(p)]\mathrm{Im}[D_\pi(q+p)]\mathrm{Re}[D_\rho^{\nu\lambda}(q+k+p)] \\
&\quad (-2p-q)_\mu(-p+k+q)_\lambda(k-q-p)_\nu(f(w)-f(q_0+w)) \\
&\quad \mathrm{FF}_\rho[q+p,k]\mathrm{FF}_\rho[p,q+k]\Bigg]_{p_0=w}, \qquad \text{(A.8)}
\end{aligned}
$$

$$
\begin{aligned}
\mathrm{Im}\Gamma^{\prime\prime(3)C\sigma k}_{\mu\,ab3}(k,q) &= \epsilon_{3ab}\frac{g_\rho g_\sigma^2}{2}\int\frac{d^3p}{(2\pi)^3}\Bigg[\int_0^\infty\frac{dw}{-\pi}\mathrm{Im}[D_\pi(p)]\mathrm{Re}[D_\pi(q-p)]\mathrm{Im}[D_\sigma(p+k)] \\
&\quad (p+k)^2-m_\pi^2)(-2p+q)_\mu(f(w)-f(k_0+w)) \\
&\quad \theta(k_0+w)\mathrm{FF}_\rho[p,k]\mathrm{FF}_\rho[-q+p,q+k]\Bigg]_{p_0=w} \qquad \text{(A.9)} \\
&\quad -\epsilon_{3ab}\frac{g_\rho g_\sigma^2}{2}\int\frac{d^3p}{(2\pi)^3}\Bigg[\int_0^\infty\frac{dw}{-\pi}\mathrm{Im}[D_\pi(p)]\mathrm{Re}[D_\pi(q-p)]\mathrm{Im}[D_\sigma(p+k)] \\
&\quad ((p+k)^2-m_\pi^2)(-2p+q)_\mu(f(w)-f(-k_0+w)) \\
&\quad \theta(-k_0+w)\mathrm{FF}_\rho[p,k]\mathrm{FF}_\rho[-q+p,q+k]\Bigg]_{p_0=-w}, \qquad \text{(A.10)} \\
\mathrm{Im}\Gamma^{\prime\prime(3)C\sigma q}_{\mu\,ab3}(k,q) &= \epsilon_{3ab}\frac{g_\rho g_\sigma^2}{2}\int\frac{d^3p}{(2\pi)^3}\Bigg[\int_0^\infty\frac{dw}{-\pi}\mathrm{Im}[D_\pi(p)]\mathrm{Re}[D_\pi(q+p)]\mathrm{Im}[D_\sigma(q+k+p)] \\
&\quad ((q+k+p)^2-m_\pi^2)(-2p-q)_\mu(f(w)-f(q_0+k_0+w)) \\
&\quad \theta(q_0+k_0+w)\mathrm{FF}_\rho[q+p,k]\mathrm{FF}_\rho[p,q+k]\Bigg]_{p_0=w} \\
&\quad -\epsilon_{3ab}\frac{g_\rho g_\sigma^2}{2}\int\frac{d^3p}{(2\pi)^3}\Bigg[\int_0^\infty\frac{dw}{-\pi}\mathrm{Im}[D_\pi(p)]\mathrm{Re}[D_\pi(q+p)]\mathrm{Im}[D_\sigma(q+k+p)] \\
&\quad ((q+k+p)^2-m_\pi^2)(-2p-q)_\mu(f(w)-f(-q_0-k_0+w)) \\
&\quad \theta(-q_0-k_0+w)\mathrm{FF}_\rho[q+p,k]\mathrm{FF}_\rho[p,q+k]\Bigg]_{p_0=-w}, \qquad \text{(A.11)} \\
\mathrm{Im}\Gamma^{\prime\prime(3)C\sigma k\pi}_{\mu\,ab3}(k,q) &= -\epsilon_{3ab}\frac{g_\rho g_\sigma^2}{2}\int\frac{d^3p}{(2\pi)^3}\Bigg[\int_0^\infty\frac{dw}{-\pi}\mathrm{Im}[D_\pi(p)]\mathrm{Im}[D_\pi(q-p)]\mathrm{Re}[D_\sigma(p+k)] \\
&\quad ((p+k)^2-m_\pi^2)(-2p+q)_\mu(f(w)-f(q_0+w)) \\
&\quad \mathrm{FF}_\sigma[p,k]\mathrm{FF}_\sigma[-q+p,q+k]\Bigg]_{p_0=w}, \qquad \text{(A.12)} \\
\mathrm{Im}\Gamma^{\prime\prime(3)C\sigma q\pi}_{\mu\,ab3}(k,q) &= \epsilon_{3ab}\frac{g_\rho g_\sigma^2}{2}\int\frac{d^3p}{(2\pi)^3}\Bigg[\int_0^\infty\frac{dw}{-\pi}\mathrm{Im}[D_\pi(p)]\mathrm{Im}[D_\pi(q+p)]\mathrm{Re}[D_\sigma(q+k+p)] \\
&\quad ((q+k+p)^2-m_\pi^2)(-2p-q)_\mu(f(w)-f(q_0+w)) \\
&\quad \mathrm{FF}_\sigma[q+p,k]\mathrm{FF}_\sigma[p,q+k]\Bigg]_{p_0=w}. \qquad \text{(A.13)}
\end{aligned}
$$

The real parts of the vertex corrections are given by the subtracted dispersion relations:

$$\mathrm{Re}\Gamma''^{(3)A\rho}_{\mu\,ab3}(k,q) = \frac{-1}{\pi}\int_{-\infty}^{\infty} dw \left(\frac{\mathrm{Im}\Gamma''^{(3)A\rho}_{\mu\,ab3}(k,q)}{k_0 - w} - \frac{\mathrm{Im}\Gamma''^{(3)A\rho}_{\mu\,ab3}\big(\{k_0 = 0, \vec{k}\}, q\big)}{-w} \right) \tag{A.14}$$

$$\mathrm{Re}\Gamma''^{(3)B\rho}_{\mu\,ab3}(k,q) = \frac{-1}{\pi}\int_{-\infty}^{\infty} dw \left(\frac{\mathrm{Im}\Gamma''^{(3)B\rho}_{\mu\,ab3}(k,q)}{k_0 - w} - \frac{\mathrm{Im}\Gamma''^{(3)B\rho}_{\mu\,ab3}\big(\{k_0 = -q_0, \vec{k}\}, q\big)}{-w} \right), \tag{A.15}$$

$$\mathrm{Re}\Gamma''^{(3)C(\rho/\sigma)k}_{\mu\,ab3}(k,q) = \frac{-1}{\pi}\int_{-\infty}^{\infty} dw \left(\frac{\mathrm{Im}\Gamma''^{(3)C(\rho/\sigma)k}_{\mu\,ab3}(k,q)}{k_0 - w} - \frac{\mathrm{Im}\Gamma''^{(3)C(\rho/\sigma)k}_{\mu\,ab3}\big(\{k_0 = 0, \vec{k}\}, q\big)}{-w} \right) \tag{A.16}$$

$$\mathrm{Re}\Gamma''^{(3)C(\rho/\sigma)q}_{\mu\,ab3}(k,q) = \frac{-1}{\pi}\int_{-\infty}^{\infty} dw \left(\frac{\mathrm{Im}\Gamma''^{(3)C(\rho/\sigma)q}_{\mu\,ab3}(k,q)}{k_0 - w} - \frac{\mathrm{Im}\Gamma''^{(3)C(\rho/\sigma)q}_{\mu\,ab3}\big(\{k_0 = -q_0, \vec{k}\}, q\big)}{-w} \right), \tag{A.17}$$

$$\mathrm{Re}\Gamma''^{(3)C(\rho/\sigma)\pi k}_{\mu\,ab3}(k,q) = \frac{-1}{\pi}\int_{-\infty}^{\infty} dw \frac{\mathrm{Im}\Gamma''^{(3)C(\rho/\sigma)\pi k}_{\mu\,ab3}(k,q)}{k_0 - w} \tag{A.18}$$

$$\mathrm{Re}\Gamma''^{(3)C(\rho/\sigma)\pi q}_{\mu\,ab3}(k,q) = \frac{-1}{\pi}\int_{-\infty}^{\infty} dw \frac{\mathrm{Im}\Gamma''^{(3)C(\rho/\sigma)\pi q}_{\mu\,ab3}(k,q)}{k_0 - w}. \tag{A.19}$$

The values for k_0 used in the subtractions are chosen so that gauge invariance is maintained. These subtractions are determined by the argument of the rho or sigma propagator, and are fixed by the Ward identities and the subtractions used in the pion self-energy. Furthermore, $\mathrm{Re}\Gamma''^{(3)C(\rho/\sigma)\pi(k/q)}_{\mu\,ab3}$ does not include a subtraction, because, unlike $\mathrm{Re}\Sigma_\pi$, $\mathrm{Re}\Gamma''^{(3)C(\rho/\sigma)\pi(k/q)}_{\mu\,ab3}$ is not proportional to $\mathrm{Re}D_{(\rho/\Sigma)}$. Instead, $\mathrm{Im}\Gamma''^{(3)C(\rho/\sigma)\pi(k/q)}_{\mu\,ab3}$ is proportional to $\mathrm{Re}D_{(\rho/\Sigma)}$, this is in fact the first time the real rho or sigma propagator has explicitly appeared in a self-energy or vertex corrections. Until now the real part of the rho and sigma propagators have been calculated through subtracted dispersion relations. Therefore, to ensure that the same rho and sigma propagators are used though

out our calculations, we perform a subtraction on $\mathrm{Im}\Gamma''^{(3)C(\rho/\sigma)\pi(k/q)}_{\mu\,ab3}$ rather than $\mathrm{Re}\Gamma''^{(3)C(\rho/\sigma)\pi(k/q)}_{\mu\,ab3}$:

$$\mathrm{Im}\tilde{\Gamma}''^{(3)C\rho\pi k}_{\mu\,ab3}(k,q) = \mathrm{Im}\Gamma''^{(3)C(\rho/\sigma)\pi k}_{\mu\,ab3}(k,q) - \mathrm{Im}\Gamma''^{(3)C\rho\pi k}_{\mu\,ab3}(\{k_0=0,\vec{k}\},q) \quad (A.20)$$

$$\mathrm{Im}\tilde{\Gamma}''^{(3)C\rho\pi q}_{\mu\,ab3}(k,q) = \mathrm{Im}\Gamma''^{(3)C(\rho/\sigma)\pi q}_{\mu\,ab3}(k,q) - \mathrm{Im}\Gamma''^{(3)C\rho\pi q}_{\mu\,ab3}(\{k_0=-q_0,\vec{k}\},q), \quad (A.21)$$

$$\mathrm{Im}\tilde{\Gamma}''^{(3)C\sigma\pi k}_{\mu\,ab3}(k,q) = \mathrm{Im}\Gamma''^{(3)C(\rho/\sigma)\pi k}_{\mu\,ab3}(k,q) - \mathrm{Im}\Gamma''^{(3)C\sigma\pi k}_{\mu\,ab3}(\{k_0=0,\vec{k}\},q) \quad (A.22)$$

$$\mathrm{Im}\tilde{\Gamma}''^{(3)C\sigma\pi q}_{\mu\,ab3}(k,q) = \mathrm{Im}\Gamma''^{(3)C(\rho/\sigma)\pi q}_{\mu\,ab3}(k,q) - \mathrm{Im}\Gamma''^{(3)C\sigma\pi q}_{\mu\,ab3}(\{k_0=-q_0,\vec{k}\},q). \quad (A.23)$$

The above subtractions have the added benefit of ensuring that the imaginary part of each vertex correction goes to zero for either $k_0 = 0$ or $q_0 + k_0 = 0$ and do no violate gauge invariance.

The corrections can be grouped into the following spectral representations, before performing the Matsubara sums in the rho self-energy:

$$D_\pi(k)\Gamma^{(3)k}_{\mu\,ab3}(k,q) = \frac{-1}{\pi}\int_{-\infty}^{\infty} dv \frac{\mathrm{Im}\big[D_\pi(v,\vec{k})\Gamma^{(3)k}_{\mu\,ab3}(\{v,\vec{k}\},q)\big]}{k_0 - v + i\epsilon}, \quad (A.24)$$

$$D_\pi(q+k)\Gamma^{(3)q}_{\mu\,ab3}(q+k,q) = \frac{-1}{\pi}\int_{-\infty}^{\infty} dv' \frac{\mathrm{Im}\big[D_\pi(v',\vec{k})\Gamma^{(3)q}_{\mu\,ab3}(\{v',\vec{k}\},q)\big]}{q_0 + k_0 - v' + i\epsilon}, \quad (A.25)$$

$$D_\pi(k)\Gamma^{(3)k}_{\mu\,ab3}(k,q)^2 = \frac{-1}{\pi}\int_{-\infty}^{\infty} dv \frac{\mathrm{Im}\big[D_\pi(v,\vec{k})\Gamma^{(3)k}_{\mu\,ab3}(\{v,\vec{k}\},q)^2\big]}{k_0 - v + i\epsilon}, \quad (A.26)$$

$$D_\pi(q+k)\Gamma^{(3)q}_{\mu\,ab3}(q+k,q)^2 = \frac{-1}{\pi}\int_{-\infty}^{\infty} dv' \frac{\mathrm{Im}\big[D_\pi(v',\vec{k})\Gamma^{(3)q}_{\mu\,ab3}(\{v',\vec{k}\},q)^2\big]}{q_0 + k_0 - v' + i\epsilon}, \quad (A.27)$$

where we define the functions:

$$\begin{aligned}\Gamma^{(3)k}_{\mu\,ab3}(k,q) &= \Gamma''^{(3)A\rho}_{\mu\,ab3}(k,q) + \Gamma''^{(3)C\rho k}_{\mu\,ab3}(k,q) + \tilde{\Gamma}''^{(3)C\rho k\pi}_{\mu\,ab3}(k,q) \\ &\quad + \Gamma''^{(3)C\sigma k}_{\mu\,ab3}(k,q) + \tilde{\Gamma}''^{(3)C\sigma k\pi}_{\mu\,ab3}(k,q) \\ &\quad + g_\rho \epsilon_{3ab}(2k+q)_i\Big(\frac{\Sigma_{\pi(\rho)}(k)}{\Lambda_{2\rho}^2 + (\vec{q}+\vec{k})^2} + \frac{\Sigma_{\pi(\sigma)}(k)}{\Lambda_{2\sigma}^2 + (\vec{q}+\vec{k})^2}\Big), \quad (A.28)\\ \Gamma^{(3)q}_{\mu\,ab3}(k,q) &= \Gamma''^{(3)B\rho}_{\mu\,ab3}(-q+k,q) + \Gamma''^{(3)C\rho q}_{\mu\,ab3}(-q+k,q) + \tilde{\Gamma}''^{(3)C\rho q\pi}_{\mu\,ab3}(-q+k,q) \\ &\quad + \Gamma''^{(3)C\sigma q}_{\mu\,ab3}(-q+k,q) + \tilde{\Gamma}''^{(3)C\sigma q\pi}_{\mu\,ab3}(-q+k,q) \\ &\quad + g_\rho \epsilon_{3ab}(2k-q)_i\Big(\frac{\Sigma_{\pi(\rho)}(k)}{\Lambda_{2\rho}^2 + (\vec{k})^2} + \frac{\Sigma_{\pi(\sigma)}(k)}{\Lambda_{2\sigma}^2 + (\vec{k})^2}\Big). \quad (A.29)\end{aligned}$$

The real part of the integrals in eqs. A.24 and A.27 are calculated from the principal values of the integrals. Furthermore, we note that the functions in $\Gamma^{(3)k}_{\mu\,ab3}$ and $\Gamma^{(3)q}_{\mu\,ab3}$ include the corrections to the $\rho\pi\pi$ vertex due to the addition of a form factor.

We are now in place to calculate the transverse projection of the $\pi\pi$-loop diagrams containing vertex corrections, at $\vec{q}=0$. In terms of $\Gamma^{(3)k}_{\mu\,ab3}$ and $\Gamma^{(3)q}_{\mu\,ab3}$ one can write the transverse projection of the vertex corrections to the $\pi\pi$-loop as:

$$\begin{aligned}
\Sigma_{\rho 1}(q_0,\vec{q}=0) &= \frac{2\pi}{3}T\sum_{n(even)}\int\frac{d|\vec{k}|\vec{k}^2}{(2\pi)^3}\int_{-\infty}^{\infty}\frac{dvdv'}{\pi^2}\frac{1}{(k_0-v+i\epsilon)(q_0+k_0-v'+i\epsilon)}\\
&\Big[2g_\rho\epsilon_{3ab}(2|\vec{k}|)\mathrm{Im}[D_\pi(v,\vec{k})\Gamma^{(3)k}_{3\,ba3}(\{v,\vec{k}\},q)]\mathrm{Im}[D_\pi(v',\vec{k})]\\
&+2g_\rho\epsilon_{3ab}(2|\vec{k}|)\mathrm{Im}[D_\pi(v,\vec{k})]\mathrm{Im}[D_\pi(v',\vec{k})\Gamma^{(3)q}_{3\,ba3}(\{v',\vec{k}\},q)]\\
&+2\mathrm{Im}[D_\pi(v,\vec{k})\Gamma^{(3)k}_{3\,ab3}(\{v,\vec{k}\},q)]\mathrm{Im}[D_\pi(v',\vec{k})\Gamma^{(3)q}_{3\,ba3}(\{v',\vec{k}\},q)]\\
&-\mathrm{Im}\big[D_\pi(v,\vec{k})\big(\Gamma^{(3)k}_{3\,ab3}(\{v,\vec{k}\},q)\big)^2\big]\mathrm{Im}[D_\pi(v',\vec{k})]\\
&-\mathrm{Im}[D_\pi(v,\vec{k})]\mathrm{Im}\big[D_\pi(v',\vec{k})\big(\Gamma^{(3)q}_{3\,ab3}(\{v',\vec{k}\},q)\big)^2\big]\Big]_{k_0=i\omega_n}+\mathrm{PV}. \quad \text{(A.30)}
\end{aligned}$$

One can now perform the Matsubara sum to obtain:

$$\begin{aligned}
\Sigma_{\rho 1}(q_0,\vec{q}=0) &= \frac{-2\pi}{3}\int\frac{d|\vec{k}|\vec{k}^2}{(2\pi)^3}\int_{-\infty}^{\infty}\frac{dvdv'}{\pi^2}\frac{(f(v)-f(v'))}{q_0+v-v'}\\
&\Big[2g_\rho\epsilon_{3ab}(2|\vec{k}|)\mathrm{Im}[D_\pi(v,\vec{k})\Gamma^{(3)k}_{3\,ba3}(\{v,\vec{k}\},q)]\mathrm{Im}[D_\pi(v',\vec{k})]\\
&+2g_\rho\epsilon_{3ab}(2|\vec{k}|)\mathrm{Im}[D_\pi(v,\vec{k})]\mathrm{Im}[D_\pi(v',\vec{k})\Gamma^{(3)q}_{3\,ba3}(\{v',\vec{k}\},q)]\\
&+2\mathrm{Im}[D_\pi(v,\vec{k})\Gamma^{(3)k}_{3\,ab3}(\{v,\vec{k}\},q)]\mathrm{Im}[D_\pi(v',\vec{k})\Gamma^{(3)q}_{3\,ba3}(\{v',\vec{k}\},q)]\\
&-\mathrm{Im}\big[D_\pi(v,\vec{k})\big(\Gamma^{(3)k}_{3\,ab3}(\{v,\vec{k}\},q)\big)^2\big]\mathrm{Im}[D_\pi(v',\vec{k})]\\
&-\mathrm{Im}[D_\pi(v,\vec{k})]\mathrm{Im}\big[D_\pi(v',\vec{k})\big(\Gamma^{(3)q}_{3\,ab3}(\{v',\vec{k}\},q)\big)^2\big]\Big]+\mathrm{PV}, \quad \text{(A.31)}
\end{aligned}$$

where PV represents the Paulli Villars regularization terms, defined by dressing the vacuum Pauli Vilars terms with thermal pion self-energies and vertex corrections. These terms can be obtained by taking the temperature in the Bose distribution $(f(v))$ to zero and replacing the pion mass in D_π

with the appropriate heavy pion mass. Next, we must remove double counting from the Landau cut of $\Sigma_{\rho 1}$. This is achieved by including a function $\tilde{\Sigma}_{\rho 1}$, which subtracts out the double counting:

$$\begin{aligned}\tilde{\Sigma}_{\rho 1}(q_0, \vec{q}=0) &= -\frac{-2\pi}{3}\int \frac{d|\vec{k}|\vec{k}^2}{(2\pi)^3}\int_{-\infty}^{\infty}\frac{dvdv'}{\pi^2}\frac{\theta(vv')(f(v)-f(v'))}{q_0+v-v'} \\ &\Big[g_\rho \epsilon_{3ab}(2|\vec{k}|)\mathrm{Im}[D_\pi(v,\vec{k})\chi^k(\{v,\vec{k}\},q)]\mathrm{Im}[D_\pi(v',\vec{k})] \\ &+g_\rho \epsilon_{3ab}(2|\vec{k}|)\mathrm{Im}[D_\pi(v,\vec{k})]\mathrm{Im}[D_\pi(v',\vec{k})\chi^q(\{v',\vec{k}\},q)]\Big], \qquad \text{(A.32)}\end{aligned}$$

where:

$$\begin{aligned}\chi^k(k,q) &= \Gamma''^{(3)C\rho k}_{3\,ba3}(k,q) + \tilde{\Gamma}''^{(3)C\rho k\pi}_{3\,ba3}(k,q) \\ \chi^q(k,q) &= \Gamma''^{(3)C\rho q}_{3\,ba3}(-q+k,q) + \tilde{\Gamma}''^{(3)C\rho q\pi}_{3\,ba3}(-q+k,q). \qquad \text{(A.33)}\end{aligned}$$

A.2 Tad pole loop corrections

In this section we calculate the corrections to the tad pole loop from the $\rho\rho\pi\pi$ vertex corrections. To begin we consider $\Gamma''^{(4)A\rho}_{\mu\nu\,ab33}$, which we rewrite in terms of a function $\tilde{\Gamma}^{(4)A\rho}_{\mu\nu\,ab33}$ such that:

$$\Gamma''^{(4)A\rho}_{\mu\nu\,ab33}(k,q) = i\big(\tilde{\Gamma}^{(4)A\rho}_{\mu\nu\,ab33}(k,q) + \tilde{\Gamma}^{(4)A\rho}_{\mu\nu\,ab33}(-k,q)\big). \qquad \text{(A.34)}$$

We have factored an i out of the vertex correction, so that it more closely resembles the vacuum $\pi\pi\rho\rho$ vertex. Furthermore, it is more convenient to define spectral representations with $\tilde{\Gamma}^{(4)A\rho}_{\mu\nu\,ab33}$ than $\Gamma''^{(4)A\rho}_{\mu\nu\,ab33}$, because the imaginary part of $\tilde{\Gamma}^{(4)A\rho}_{\mu\nu\,ab33}$ can be broken into cuts corresponding to corrections induced by either Σ_π's Landau or unitarity cut. After grouping propagators into spectral representations and performing the Matsubara sum, the imaginary part of $\tilde{\Gamma}^{(4)A\rho}_{\mu\nu\,ab33}$ can be calculated

using eq. 2.25:

$$\begin{aligned}
\mathrm{Im}\tilde{\Gamma}^{(4)A\rho}_{\mu\nu\,ab33}(k,q) &= -(-3\delta_{3a}\delta_{3b}+5\delta_{ab})\frac{g_\rho^4}{2}\int\frac{d^3p}{(2\pi)^3}\Big[\int_0^\infty\frac{dw}{-\pi}\mathrm{Im}[D_\pi(p)]\mathrm{Im}[D_\rho^{\mu\nu}(q+k+p)] \\
&\quad (f(w)-f(q_0+k_0+w))\theta(q_0+k_0+w)\mathrm{FF}_\rho[q+p,k]^2\Big]_{p_0=w} \\
&\quad +(-3\delta_{3a}\delta_{3b}+5\delta_{ab})\frac{g_\rho^4}{2}\int\frac{d^3p}{(2\pi)^3}\Big[\int_0^\infty\frac{dw}{-\pi}\mathrm{Im}[D_\pi(p)]\mathrm{Im}[D_\rho^{\mu\nu}(q+k+p)] \\
&\quad (f(w)-f(-q_0-k_0+w))\theta(-q_0-k_0+w)\mathrm{FF}_\rho[q+p,k]^2\Big]_{p_0=-w}, \quad \text{(A.35)}
\end{aligned}$$

where we only write the cuts necessary to maintain gauge invariance with the Landau cut of Σ_π. The real part of $\Gamma''^{(4)A\rho}_{\mu\nu\,ab33}$ can be calculated with the subtracted dispersion relation:

$$\mathrm{Im}\tilde{\Gamma}''^{(4)A\rho}_{\mu\nu\,ab33} = \frac{-1}{\pi}\int_{-\infty}^{\infty}dw\Big(\frac{\mathrm{Im}\tilde{\Gamma}''^{(4)A\rho}_{\mu\nu\,ab33}(k,q)}{k_0-w}-\frac{\mathrm{Im}\tilde{\Gamma}^{(4)A\rho}_{\mu\nu\,ab33}\big(\{k_0=-q_0,\vec{k}\},q\big)}{-w}\Big). \quad \text{(A.36)}$$

The transverse projection of the rho self-energy corrections derived from $\Gamma''^{(4)A\rho}_{\mu\nu\,ab33}$, at $\vec{q}=0$ are

given by:

$$\begin{aligned}
\Sigma_{\rho 2}(q_0,0) &= \frac{2\pi}{3}T\sum_{n(even)}\int\frac{d|\vec{k}|\vec{k}^2}{(2\pi)^3}\Big[D_\pi(k)(-i)\Gamma''^{(4)A\rho}_{ii\,aa33}(k,q)\Big]_{k_0=i\omega_n}+\text{PV}\\
&= \frac{4\pi}{3}T\sum_{n(even)}\int\frac{d|\vec{k}|\vec{k}^2}{(2\pi)^3}\int_{-\infty}^{\infty}\frac{dvdv'}{\pi^2}\text{Im}[\tilde{\Gamma}^{(4)A\rho}_{ii\,aa33}(\{-q_0+v',\vec{k}\},q)]\\
&\quad \text{Im}[D_\pi(v,\vec{k})]\frac{1}{(i\omega_n-v+i\epsilon)(q_0+i\omega_n-v'+i\epsilon)}+\text{PV}\\
&= \frac{-4\pi}{3}\int\frac{d|\vec{k}|\vec{k}^2}{(2\pi)^3}\int_{-\infty}^{\infty}\frac{dvdv'}{\pi^2}\text{Im}[\tilde{\Gamma}^{(4)A\rho}_{ii\,aa33}(\{-q_0+v',\vec{k}\},q)]\\
&\quad \text{Im}[D_\pi(v,\vec{k})]\frac{1}{q_0+v-v'+i\epsilon}(f(v)-f(v'))(1-\frac{1}{2}\theta(vv'))\\
&\quad \text{Im}[D_\pi(v,\vec{k})]f(v)(1-\frac{1}{2}\theta(vv'))+\text{PV}, \qquad \text{(A.37)}\\
\Sigma^0_{\rho 2} &= \frac{4\pi}{3}T\sum_{n(even)}\int\frac{d|\vec{k}|\vec{k}^2}{(2\pi)^3}\int_{-\infty}^{\infty}\frac{dv}{-\pi}\text{Re}[\tilde{\Gamma}^{(4)A\rho}_{ii\,aa33}(\{0,\vec{k}\},0)]\frac{\text{Im}[D_\pi(v,\vec{k})]}{(i\omega_n-v+i\epsilon)}+\text{PV}\\
&= -\frac{4\pi}{3}\int\frac{d|\vec{k}|\vec{k}^2}{(2\pi)^3}\int_{-\infty}^{\infty}\frac{dv}{-\pi}\text{Re}[\tilde{\Gamma}^{(4)A\rho}_{ii\,aa33}(\{0,\vec{k}\},0)]\\
&\quad \text{Im}[D_\pi(v,\vec{k})]f(v)(1-\frac{1}{2}\theta(v))+\text{PV} \qquad \text{(A.38)}
\end{aligned}$$

where the theta functions are added in the last equalities to remove double counting from the Landau cut, as was described in section 4.6. Furthermore, we have explicitly calculated the self-energy contribution from the subtraction constant in $\text{Re}\tilde{\Gamma}^{(4)A\rho}_{ii\,aa33}$ with $\Sigma^0_{\rho 2}$. This is done because the spectral representation of $\tilde{\Gamma}^{(4)A\rho}_{ii\,aa33}$ has no knowledge of the subtraction, thus it must be handled separately.

The corrections to the tad pole due to the addition of a form factor can be expressed in a similar

form. We write these contributions in terms of the functions:

$$
\begin{aligned}
Y_{Fk}(k,\{q_0,\vec{q}=0\}) &= -\frac{4g_\rho\epsilon_{3ca}k_3}{\Lambda_{2\rho}^2+\vec{k}^2}\Big[\Gamma''^{(3)A\rho}_{3\,ac3}(k,q)+\Gamma''^{(3)C\rho k}_{3\,ac3}(k,q)+\Gamma''^{(3)C\rho k\pi}_{3\,ac3}(k,q)\Big] \\
&\quad -\frac{4g_\rho\epsilon_{3ca}k_3}{\Lambda_{2\sigma}^2+\vec{k}^2}\Big[\Gamma''^{(3)C\sigma k}_{3\,ac3}(k,q)+\Gamma''^{(3)C\sigma k\pi}_{\mu\,ac3}(k,q)\Big] \\
&\quad -4g_\rho^2\Bigg\{4k_3^2\left[\frac{\Sigma_{\pi(\rho)}(k)}{(\Lambda_{2\rho}^2+\vec{k}^2)^2}+\frac{\Sigma_{\pi(\sigma)}(k)}{(\Lambda_{2\sigma}^2+\vec{k}^2)^2}\right] \\
&\quad -3\frac{\Sigma_{\pi(\rho)}(k)}{\Lambda_{2\rho}^2+\vec{k}^2}-3\frac{\Sigma_{\pi(\sigma)}(k)}{\Lambda_{2\sigma}^2+\vec{k}^2}\Bigg\}, \qquad \text{(A.39)} \\
Y_{Fq}(k,\{q_0,\vec{q}=0\}) &= -\frac{4g_\rho\epsilon_{3ca}k_3}{\Lambda_{2\rho}^2+\vec{k}^2}\Big[\Gamma''^{(3)B\rho}_{3\,ab3}(-q+k,q)+\Gamma''^{(3)C\rho q}_{3\,ab3}(-q+k,q) \\
&\quad +\Gamma''^{(3)C\rho q\pi}_{3\,ab3}(-q+k,q)\Big] \\
&\quad -\frac{4g_\rho\epsilon_{3ca}k_3}{\Lambda_{2\sigma}^2+\vec{k}^2}\Big[\Gamma''^{(3)C\sigma q}_{3\,ab3}(-q+k,q)+\Gamma''^{(3)C\sigma q\pi}_{3\,ab3}(-q+k,q)\Big] \\
&\quad -8g_\rho^2k_3^2\left[\frac{\Sigma_{\pi(\rho)}(k)}{(\Lambda_{2\rho}^2+\vec{k}^2)^2}+\frac{\Sigma_{\pi(\sigma)}(k)}{(\Lambda_{2\sigma}^2+\vec{k}^2)^2}\right]. \qquad \text{(A.40)}
\end{aligned}
$$

The transverse projection of the corresponding rho self-energy correction at $\vec{q}=0$ is then given

by:

$$\begin{aligned}
\Sigma_{\rho 3}(q_0,0) &= \frac{2\pi}{3}T\sum_{n(even)}\int\frac{d|\vec{k}|\vec{k}^2}{(2\pi)^3}\Big[D_\pi(k)\big(Y_{Fq}(q+k,q)+Y_{Fq}(q-k,q)+ \\
&\quad Y_{Fk}(k,q)+Y_{Fk}(-k,q)\big)\Big]_{k_0=i\omega_n} \\
&= \frac{4\pi}{3}T\sum_{n(even)}\int\frac{d|\vec{k}|\vec{k}^2}{(2\pi)^3}\int_{-\infty}^{\infty}\frac{dvdv'}{\pi^2}\mathrm{Im}[Y_{Fq}(\{v',\vec{k}\},q)] \\
&\quad \mathrm{Im}[D_\pi(v,\vec{k})]\frac{1}{(i\omega_n-v+i\epsilon)(q_0+i\omega_n-v'+i\epsilon)} \\
&= \frac{-4\pi}{3}\int\frac{d|\vec{k}|\vec{k}^2}{(2\pi)^3}\int_{-\infty}^{\infty}\frac{dvdv'}{\pi^2}\mathrm{Im}[Y_{Fq}(\{v',\vec{k}\},q)] \\
&\quad \mathrm{Im}[D_\pi(v,\vec{k})]\frac{1}{q_0+v-v'+i\epsilon}(f(v)-f(v'))+\mathbf{PV}, \qquad \text{(A.41)} \\
\Sigma^0_{\rho 3} &= \frac{4\pi}{3}T\sum_{n(even)}\int\frac{d|\vec{k}|\vec{k}^2}{(2\pi)^3}\int_{-\infty}^{\infty}\frac{dv}{-\pi}\mathrm{Re}[Y_{Fq}(\{0,\vec{k}\},0)]\frac{\mathrm{Im}[D_\pi(v,\vec{k})]}{(i\omega_n-v+i\epsilon)}+ \\
&\quad \frac{4\pi}{3}T\sum_{n(even)}\int\frac{d|\vec{k}|\vec{k}^2}{(2\pi)^3}\int_{-\infty}^{\infty}\frac{dv}{-\pi}\frac{\mathrm{Im}\big[Y_{Fk}(\{v,\vec{k}\},0)D_\pi(v,\vec{k})\big]}{(i\omega_n-v+i\epsilon)} \\
&= -\frac{4\pi}{3}\int\frac{d|\vec{k}|\vec{k}^2}{(2\pi)^3}\int_{-\infty}^{\infty}\frac{dv}{-\pi}\mathrm{Re}[Y_{Fq}(\{0,\vec{k}\},0)]\mathrm{Im}[D_\pi(v,\vec{k})]f(v)- \\
&\quad \frac{4\pi}{3}\int\frac{d|\vec{k}|\vec{k}^2}{(2\pi)^3}\int_{-\infty}^{\infty}\frac{dv}{-\pi}\mathrm{Im}\big[Y_{Fk}(\{v,\vec{k}\},0)D_\pi(v,\vec{k})\big]f(v)+\mathbf{PV}, \qquad \text{(A.42)}
\end{aligned}$$

where we again must calculate the contribution from the subtraction constants in ReY_{Fq} explicitly with $\Sigma^0_{\rho 3}$. We note that the rho self-energy diagrams involving Y_{Fk} only contribute a constant shift to the real part of Σ^T_ρ, and thus are also included in $\Sigma^0_{\rho 3}$.

Next, we calculate the corrections to the tad pole that can be expressed in terms of unitarity cuts of $\rho\pi$ or $\sigma\pi$-loops, $\Gamma''^{(4)B_1\rho}_{\mu\nu\,ab33}$, $\Gamma''^{(4)B_2\rho}_{\mu\nu\,ab33}$, $\Gamma''^{(4)E\rho}_{\mu\nu\,ab33}$, $\Gamma^{(4)G\rho}_{\mu\nu\,ab33}$, $\Gamma''^{(4)E\sigma}_{\mu\nu\,ab33}$, and $\Gamma''^{(4)G\sigma}_{\mu\nu\,ab33}$. From figure 4.12, one can see that the tad pole contributions derived from $\Gamma''^{(4)E\rho}_{\mu\nu\,ab33}$, $\Gamma^{(4)G\rho}_{\mu\nu\,ab33}$, $\Gamma''^{(4)E\sigma}_{\mu\nu\,ab33}$, and $\Gamma''^{(4)G\sigma}_{\mu\nu\,ab33}$ simply dress a pion propagator in the rho self-energy with a $\rho\pi$ or $\sigma\pi$-loop. When the tap pole loop was thermal this produced double counting, however the vacuum tad pole loop produces unique rho self-energies. These rho self-energies dress a pion propagator with the unitarity cut of the pion self-energy (Σ^U_π). Σ^U_π is given for positive energy by the sum of eqs. 3.37 and 3.41. For negative

energy Σ_π^U is determined by enforcing the retarded property of the pion self-energy (eq. 3.45). The real part of Σ_π^U can then be evaluated with a dispersion relation. However, the dispersion relations converges quite slowly, resulting in an unphysical shift of the pion mass by approximately 800 MeV. This shift is produced by vacuum $\pi \rightarrow \rho\pi$ decay and in principal should be absorbed into the pion mass, however modifying the real part of the vacuum tad pole loop in only these diagrams would violate gauge invariance. In order to remove the shift systematically and preserve gauge invariance, we resum the pion propagators in the rho self-energy with Σ_π^U giving:

$$\begin{aligned}
\Sigma^{\mu\nu}_{\rho U}(q) &= g_\rho^2 \int \frac{d^3k}{(2\pi)^3} \int_{-\infty}^{\infty} \frac{dvdv'}{\pi^2} \frac{(2k+q)^\mu (2k+q)^\nu}{q_0 + v - v' + i\epsilon} (f(v) - f(v'))\theta(vv') \\
&\quad \mathrm{Im}[\frac{1}{v^2 - \vec{k}^2 - m_\pi^2 - \Sigma_\pi(v,\vec{k},T) - \Sigma_\pi^U(v,\vec{k},T) - \mathrm{Re}\Sigma_\pi^U(m_\pi,0,0)}] \\
&\quad \mathrm{Im}[\frac{1}{(v')^2 - (\vec{q}+\vec{k})^2 - m_\pi^2 - \Sigma_\pi(v',\vec{q}+\vec{k},T) - \Sigma_\pi^U(v',\vec{q}+\vec{k},T) - \mathrm{Re}\Sigma_\pi^U(m_\pi,0,0)}] \\
&\quad -2g_\rho^2 g^{\mu\nu} \int \frac{d^3k}{(2\pi)^3} \int_{-\infty}^{\infty} \frac{dv}{-\pi} f(v)\theta(v) \\
&\quad \mathrm{Im}[\frac{1}{v^2 - \vec{k}^2 - m_\pi^2 - \Sigma_\pi(v,\vec{k},T) - \Sigma_\pi^U(v\vec{k},T) - \mathrm{Re}\Sigma_\pi^U(m_\pi,0,0)}], \qquad \text{(A.43)}
\end{aligned}$$

where

$$\mathrm{Re}\Sigma_\pi^U(k) = \frac{-1}{\pi} \mathrm{p.v.} \int_0^\infty dv^2 \frac{\mathrm{Im}\Sigma_\pi^U(v,\vec{k})}{k_0^2 - v^2} - \frac{\mathrm{Im}\Sigma_\pi^U(v,\vec{k})}{-v^2}, \qquad \text{(A.44)}$$

and we have limited the integration with theta functions to ensure we do not introduce new vacuum rho self-energy diagrams. Finally, we apply Pauli Villars regularization to the vacuum Σ_π^U loop, such that:

$$\begin{aligned}
\mathrm{Im}\Sigma_\pi^U(k,m_\pi,T) \rightarrow\ & \mathrm{Im}\Sigma_\pi^U(k,m_\pi,T) - 2\mathrm{Im}\Sigma_\pi^U(k,\sqrt{m_\pi^2+\Lambda_0^2},T=0) \\
& + \mathrm{Im}\Sigma_\pi^U(k,\sqrt{m_\pi^2+2\Lambda_0^2},T=0), \qquad \text{(A.45)}
\end{aligned}$$

Equation A.43 contains the tad pole corrections derived from $\Gamma''^{(4)E\rho}_{\mu\nu\,ab33}$, $\Gamma^{(4)G\rho}_{\mu\nu\,ab33}$, $\Gamma''^{(4)E\sigma}_{\mu\nu\,ab33}$, and $\Gamma''^{(4)G\sigma}_{\mu\nu\,ab33}$ in the resummation of the pion propagator. However, in eq. A.43 we are free to treat Σ_π^U

equivalently to Σ_π, performing a zero energy subtraction on $\text{Re}\Sigma^U_\pi$. Furthermore, we add a constant shift $\text{Re}\Sigma^U_\pi(k_0 = m_\pi, \vec{k} = 0, T = 0)$ to ensure that the vacuum pion mass is 140 MeV at $\vec{p} = 0$. We are now free to add this constant without violating gauge invariance, because it simply amounts to a redefinition of the bare pion mass. Finally, because we have dressed the pion propagators with Σ^U_π the Ward identities imply that additional vertex correction should be calculated. These additional correction simply correspond to the unitarity cuts of the previously calculated thermal vertex correction. However, we have actually already encountered these corrections by dressing the unitarity cut of the rho self-energy with thermal vertex corrections. For example, the first two diagrams in figure 4.12 are derived from the vertex corrections $\Gamma''^{(4)B_1\rho}_{\mu\nu\, ab33}$ and $\Gamma''^{(4)B_2\rho}_{\mu\nu\, ab33}$, however one can also generate these diagrams by dressing the $\pi\pi$-loop with the unitarity cut of $\Gamma''^{(3)A\rho}_{\mu\, ab3}$. This symmetry is precisely why double counting was encountered in the Landau cut. In fact, the first order corrections to the resummation in eq. A.43 are already included in our formalism, and attempting to explicitly calculate vertex corrections due to Σ^U_π would only introduce double counting into the unitarity cut of $\Sigma^{\mu\nu}_\rho$.

We now take the transverse projections of $\Sigma^{\mu\nu}_{\rho U}$, at $\vec{q} = 0$ to obtain:

$$\begin{aligned}
\Sigma_{\rho 4}(q_0, 0) &= \frac{4\pi g_\rho^2}{3} \int \frac{d\vec{k}\vec{k}^2}{(2\pi)^3} \int_{-\infty}^{\infty} \frac{dv dv'}{\pi^2} \frac{4\vec{k}^2}{q_0 + v - v' + i\epsilon} (f(v) - f(v'))\theta(vv') \\
&\quad \text{Im}[\frac{1}{v^2 - \vec{k}^2 - m_\pi^2 - \Sigma_\pi(v, \vec{k}, T) - \Sigma^U_\pi(v, \vec{k}, T) - \text{Re}\Sigma^U_\pi(m_\pi, 0, 0)}] \\
&\quad \text{Im}[\frac{1}{(v')^2 - (\vec{q} + \vec{k})^2 - m_\pi^2 - \Sigma_\pi(v', \vec{q} + \vec{k}, T) - \Sigma^U_\pi(v', \vec{q} + \vec{k}, T) - \text{Re}\Sigma^U_\pi(m_\pi, 0, 0)}]
\end{aligned} \tag{A.46}$$

$$\begin{aligned}
\Sigma^0_{\rho 4}(q_0, 0) &= -\frac{8 g_\rho^2}{3} \int \frac{d\vec{k}\vec{k}^2}{(2\pi)^3} \int_{-\infty}^{\infty} \frac{dv}{-\pi} f(v)\theta(v) \\
&\quad \text{Im}[\frac{1}{v^2 - \vec{k}^2 - m_\pi^2 - \Sigma_\pi(v, \vec{k}, T) - \Sigma^U_\pi(v\vec{k}, T) - \text{Re}\Sigma^U_\pi(m_\pi, 0, 0)}],
\end{aligned} \tag{A.47}$$

where $\Sigma^0_{\rho 4}$ gives the constant shift in $\text{Re}\Sigma_\rho$ from dressing the tad pole loop.

Finally, we calculate the rho self-energy corrections due to $\Gamma''^{(4)B_1\rho}_{\mu\nu\, ab33}$ and $\Gamma''^{(4)B_2\rho}_{\mu\nu\, ab33}$. We have

already indicated that these corrections can be expressed in terms of the unitarity cut of $\Gamma^{\prime\prime(3)A\rho}_{\mu\,ab3}$:

$$\begin{aligned}
\mathrm{Im}\Gamma^{\prime\prime(3)AU\rho}_{\mu\,ab3}(k,q) &= \epsilon_{3ab}\frac{3g_\rho^3}{2}\int\frac{d^3p}{(2\pi)^3}\Big[\int_0^\infty\frac{dw}{-\pi}\mathrm{Im}[D_\pi(p)]\mathrm{Im}[D_\rho^{\nu\lambda}(p+k)] \\
&\quad g_{\mu\lambda}(k-p)_\nu(1+f(w)+f(k_0-w)) \\
&\quad \theta(k_0-w)\mathrm{FF}_\rho[-q+p,q+k]\mathrm{FF}_\rho[p,k]\Big]_{p_0=-w} \\
&\quad -\epsilon_{3ab}\frac{3g_\rho^3}{2}\int\frac{d^3p}{(2\pi)^3}\Big[\int_0^\infty\frac{dw}{-\pi}\mathrm{Im}[D_\pi(p)]\mathrm{Im}[D_\rho^{\nu\lambda}(p+k)] \\
&\quad g_{\mu\lambda}(k-p)_\nu(1+f(w)+f(-k_0-w)) \\
&\quad \theta(-k_0-w)\mathrm{FF}_\rho[-q+p,q+k]\mathrm{FF}_\rho[p,k]\Big]_{p_0=w} \\
&\quad -2\Big[m_\pi\to\sqrt{m_\pi^2+\Lambda_0^2}\Big]_{T=0}+\Big[m_\pi\to\sqrt{m_\pi^2+2\Lambda_0^2}\Big]_{T=0}, \qquad \text{(A.48)}
\end{aligned}$$

where the last line implements the Pauli Villars regularization on the vacuum loop. The real part of $\Gamma^{\prime\prime(3)AU\rho}_{\mu\,ab3}$ is given by the subtracted dispersion relation:

$$\mathrm{Re}\Gamma^{\prime\prime(3)AU\rho}_{\mu\,ab3}(k,q) = \frac{-1}{\pi}\mathrm{p.v.}\int_{-\infty}^{\infty}dv\frac{\mathrm{Im}\Gamma^{\prime\prime(3)AU\rho}_{\mu\,ab3}(\{v,\vec{k}\},q)}{k_0-v}-\frac{\mathrm{Im}\Gamma^{\prime\prime(3)AU\rho}_{\mu\,ab3}(\{v,\vec{k}\},q)}{-v^2}. \qquad \text{(A.49)}$$

The self-energy correction arising from $\Gamma^{\prime\prime(4)B_1\rho}_{\mu\nu\,ab33}$ and $\Gamma^{\prime\prime(4)B_2\rho}_{\mu\nu\,ab33}$ is then given by:

$$\begin{aligned}
\Sigma_{\rho 5}(q_0,0) &= \frac{-8\pi}{3}\int\frac{d|\vec{k}|\vec{k}^2}{(2\pi)^3}\int_{-\infty}^{\infty}\frac{dvdv'}{\pi^2}\mathrm{Im}[D_\pi(v',\vec{k})]\mathrm{Im}\big[D_\pi(v,\vec{k})\Gamma^{(3)AU\rho}_{3ba}(v,\vec{k})\big] \\
&\quad (2g_\rho|\vec{k}|\epsilon_{3ab})\frac{(f(v)-f(v'))}{(q_0+v-v'+i\epsilon)}\theta(vv'), \qquad \text{(A.50)}
\end{aligned}$$

where we again limit our calculation to the Landau cut of $\Sigma_\rho^{\mu\nu}$.

A.3 Total corrections

The total contribution of the vertex corrections to the transverse projections of the rho self-energy, at $\vec{q} = 0$, is given by:

$$\begin{aligned}\Sigma_{\rho}^{VC}(q_0, 0) &= \Sigma_{\rho 1}(q_0, 0) + \tilde{\Sigma}_{\rho 1}(q_0, 0) + \Sigma_{\rho 2}(q_0, 0) + \Sigma_{\rho 2}^{0} + \Sigma_{\rho 3}(q_0, 0) + \Sigma_{\rho 3}^{0} \\ &\quad + \Sigma_{\rho 4}(q_0, 0) + \Sigma_{\rho 4}^{0} + \Sigma_{\rho 5}(q_0, 0). \end{aligned} \tag{A.51}$$

The imaginary part can be calculated from $\Sigma_{\rho 1}$, $\tilde{\Sigma}_{\rho 1}$, $\Sigma_{\rho 2}$, $\Sigma_{\rho 3}$, $\Sigma_{\rho 4}$, and $\Sigma_{\rho 5}$ by converting $\frac{1}{q_0 + v - v' + i\epsilon}$ into a delta function and performing the remaining integrations. The real part can then be calculated through the dispersion relation:

$$\mathrm{Re}\Sigma_{\rho}^{VC}(q) = \frac{-1}{\pi} \mathrm{p.v.} \int_0^{\infty} \frac{dv^2 \mathrm{Im}\Sigma_{\rho}^{VC}(v, \vec{q})}{q_0^2 - v^2} + \Sigma_{\rho 2}^{0} + \Sigma_{\rho 3}^{0} + \Sigma_{\rho 4}^{0}, \tag{A.52}$$

where we do not perform a subtraction, because we have explicitly calculated the nondispersive constant with $\Sigma_{\rho 2}^{0}$, $\Sigma_{\rho 3}^{0}$, $\Sigma_{\rho 4}^{0}$.